Numerical Modeling for the Static and Dynamic Analysis of Nearly Incompressible Dielectric Elastomers

von

Dipl.-Ing. Markus Klassen
aus Asunción

In Erinnerung an meine Mutter.

Vorwort

Die vorliegende Arbeit entstand während meiner Tätigkeit als wissenschaftlicher Mitarbeiter am Lehrstuhl für Technische Mechanik der Technischen Universität Kaiserslautern.

Als Erstes möchte ich mich bei Herrn Prof. Dr.-Ing. Ralf Müller für die ausgezeichnete Betreuung meiner Arbeit bedanken. Insbesondere bin ich für die guten Gespräche fachlicher und nicht fachlicher Natur dankbar, als auch für die stetige Unterstützung, die ich während meiner Arbeit erhalten habe. Weiterhin bedanke ich mich bei Herrn Prof. Dr.-Ing. habil. Sven Klinkel für die freundliche Übernahme des Korreferats und das Interesse an meiner Arbeit. Ebenfalls möchte ich mich bei Frau Prof. Dr. Bai-Xiang Xu für die gemeinsame Zeit in Kaiserslautern bedanken, welche meinen Einstieg in die Thematik erleichtert hat. Außerdem gilt mein Dank auch Herrn Prof. Dr.-Ing. Tilmann Beck für sein Entgegenkommen bei der Übernahme des Vorsitzes.

Zusätzlich möchte ich mich recht herzlich bei meinen Kollegen am Lehrstuhl bedanken. Sowohl der fachliche Austausch wie auch die Freizeitaktivitäten werden bei mir in sehr guter Erinnerung bleiben. Allein die Tatsache, dass es mir nicht leicht gefallen ist den Lehrstuhl zu verlassen, spricht für sich. An dieser Stelle möchte ich auch meinen Freundeskreis, welcher während meiner Studienzeit entstanden ist, erwähnen. Obwohl die Entfernung zwischen uns in den letzten Jahren zugenommen hat, bleibt die enge Freundschaft bestehen. Ebenso bedanke ich mich bei meinen Freunden in der fernen Heimat in Asunción.

Auch meiner Familie in Paraguay und Enkenbach möchte ich an dieser Stelle Lob und Anerkennung ausdrücken. Vor allem meinem Vater, der mich in allem unterstützt hat was ich mir vorgenommen habe, auch wenn es nicht immer sofort geklappt hat. Du bist der Beste!

Abschließend gilt ein sehr großes Dankeschön Britta. Danke für die Geduld und die Unterstützung, die ich während den letzten Zügen dieser Arbeit benötigt habe.

Aachen, Oktober 2016 Markus Klassen

Kurzfassung

Die vorliegende Arbeit beschäftigt sich mit der numerischen Modellierung und Analyse von Kunststoffen, welche unter dem Einfluss eines elektrischen Feldes verformt werden. Diese Kunststoffe sind als deformierbare Dielektrika bekannt und sind somit verwendbar als Aktoren, welche elektrische Energie in mechanische Bewegung umsetzten. Außerdem werden diese Materialien oft als künstliche Muskeln vorgeschlagen, da ihr Spannungs- und Dehnungsbereich mit dem von natürlichen Muskeln übereinstimmt.

Weitere Inspirationen für die praktische Anwendung lassen sich in der Natur finden, wie zum Beispiel ein Luftschiff, welches durch fischartige Bewegungen vorangetrieben wird. Anstatt eines Propellers werden deformierbare Dielektrika an den Rumpfseiten und an der Heckflosse angebracht, um die Bewegungen eines Fisches durch die Verformung des Schiffes zu imitieren. Weitere Anwendungsbeispiele sind Linsen mit veränderbarem Brennpunkt, Lautsprecher, Pumpen, haptische Bildschirme oder Roboter. Auch die Umkehrung dieser Anwendung ist möglich. Durch das Aufbringen einer mechanischen Verformung auf das Dielektrikum lässt sich mechanische in elektrische Energie umwandeln.

Der Nachteil dieser Technologie resultiert aus den hohen elektrischen Feldern, welche für die Aktuation erforderlich sind. Beispielsweise werden für haptische Bildschirme Spannungen von über 5 kV benötigt, um eine zweckerfüllende Deformation zu erzielen. Des Weiteren zeigen die Ergebnisse dieser Arbeit, dass elektrische Felder von ca. 28 kV/mm benötigt werden, um ein Dielektrikum um 30 % zu komprimieren. Hieraus folgt, dass die Konstruktion von Aktoren aus deformierbaren Dielektrika eine Herausforderung darstellt, nämlich mit möglichst geringen Spannungen ausreichend große Deformationen zu erzielen.

Aus diesem Grund wird ein Verbundwerkstoff vorgeschlagen, welcher aus einer dielektrischen Matrix mit Einschlüssen aus Bariumtitanat besteht. Hierzu werden in der vorliegenden Arbeit die notwendigen Aspekte für die numerische Simulation eingeführt und

hergeleitet, um anschließend geeignete Beispiele zu berechnen. Dabei wird insbesondere die Inkompressibilität als auch die elektromechanische Stabilität von Dielektrika in Betracht gezogen.

Nach einer Einleitung in die Thematik der deformierbaren Dielektrika, werden als Erstes die Grundlagen der nichtlinearen Kontinuumsmechanik erläutert. Dabei ist die Vereinfachung der linearen Theorie nicht zielführend, da für die Modellierung der Dielektrika die Theorie von großen Deformationen benötigt wird. Die konstitutiven Gesetze vom neo-Hooke- und Yeoh-Typ werden eingeführt und die Spannungen und Materialtangenten aus den entsprechenden Formulierungen der freien Energie abgeleitet. Da für eine reine Verschiebungsformulierung das volumetrische „Locking" bei inkompressiblen Materialien auftritt, wird die Drei-Feld-Formulierung eingeführt, welche die Inkompressibilität realistisch abbildet.

Als Nächstes werden die Aspekte der Elektrostatik beschrieben. Ausgehend vom Coulombschen Gesetz werden die Definitionen für das elektrische Feld und das Potentialfeld eingeführt, außerdem das Gaußsche Gesetz und das Modell vom elektrischen Dipol. Des Weiteren wird der Einfluss von elektrischen Feldern auf ein polarisierbares Material beschrieben. Hierzu wird das Konzept der Polarisation benötigt, mit dem sich die Kräfte von elektrischen Feldern auf Dielektrika beschreiben lassen. Als Grundlage für den Aktuationsmechanismus von deformierbaren Dielektrika werden die Anziehungskräfte zwischen den parallelen Platten eines Kondensators im Vakuum betrachtet. Anschließend wird das Konzept des Maxwell-Spannungstensors mit Bezug zur elektrostatischen Volumenlast, welche für die Verformung von Dielektrika verantwortlich ist, eingeführt.

Um die Mechanik mit der Elektrostatik zur Beschreibung von deformierbaren Dielektrika zu koppeln, wird die mechanische Impulsbilanz durch das Konzept des Maxwell-Spannungstensors als Bilanz einer Gesamtspannung aus mechanischem und elektrischem Anteil umformuliert. Unter der zusätzlichen Verwendung des Satzes von Gauß lässt sich somit die Gleichgewichtsbilanz für das elektromechanische Problem formulieren. Diese Gleichungen lassen sich wiederum in die schwache Form für die Referenzkonfiguration umformulieren, um für die numerische Implementierung diskretisiert zu werden. Dabei wird die konsistente Tangentenmatrix, welche im Rahmen des Newton Verfahren benötigt wird, für die Verschiebungsformulierung hergeleitet. Es wird bewiesen, dass die Tangentenmatrix symmetrisch ist. Daraus erschließt sich die Abstammung des elektromechanisch gekoppelten Problems aus einer variationellen Formulierung. Zusätzlich wird die Diskretisierung der Drei-Feld-Formulierung mit Herleitung der entsprechenden Tangentenmatrix für ein inkompressibles Material beschrieben. Anschließend wird die Implementierung um Terme für Trägheit und Dämpfung erweitert, um die numerische Simulation der Dynamik zu ermöglichen.

In einem dielektrischen Aktor ist die Kompression zwischen den Elektroden durch die elektromechanische Stabilität begrenzt. Diese Einschränkung beruht auf der quadratischen Abhängigkeit der elektrostatischen Anziehungskraft zwischen den Elektroden bzgl. des elektrischen Feldes. Dadurch wird das Gleichgewicht des Aktors ab einer gewissen Kompression instabil. Abhängig vom gewählten mathematischen Materialmodell, wird der kritische Kompressionspunkt bestimmt. So liegt dieser im Fall eines neo-Hooke-Modells bei ca. 37 %. Für das Yeoh-Modell ergeben sich zwei kritische Werte, nämlich 31,9 % und 74,3 %, wobei das Gleichgewicht zwischen diesen Punkten instabil ist. Es sei an dieser Stelle angemerkt, dass die kritischen Punkte vom gewählten Modell abhängen und nicht von den Materialparametern. In dieser Arbeit werden die Grundzüge der Stabilitätsanalyse hergeleitet. Anschließend werden die Ergebnisse dieser Analyse mit numerischen Simulationen verglichen. In den Ergebnissen stellt sich heraus, dass im stabilen Bereich die Kompressionskurven aus der numerischen Simulation mit der Stabilitätsanalyse übereinstimmen. Für den instabilen Bereich lassen sich mit der in dieser Arbeit verwendeten Methodik keine numerischen Ergebnisse bestimmen, da das Newton Verfahren in diesem Bereich nicht konvergiert.

Es werden sowohl statische als auch dynamische Simulationsanalysen an einem homogenen Dielektrikum durchgeführt. Als Erstes wird das Beispiel eines eingebetteten dielektrischen Aktors berechnet, um den Vorteil der Drei-Feld-Formulierung im quasi inkompressiblen Fall gegenüber der reinen Verschiebungsformulierung zu zeigen. In den Ergebnissen zeigt sich, dass der Ansatz der Drei-Feld-Formulierung zu einer größeren Deformation als in der reinen Verschiebungsformulierung führt. Außerdem ist der Einfluss der Querkontraktionszahl auf die Kompression für den quasi inkompressiblen Fall geringer als in der reinen Verschiebungsformulierung. Des Weiteren wird das Beispiel einer rohrförmigen Pumpe betrachtet, welche aus einem deformierbaren Dielektrikum besteht an dem mehrere Elektrodenpaare entlang der Rohrlänge angebracht sind. Für die Untersuchung der Dynamik wird ein Aktor betrachtet, welcher durch Gleich- und Wechselspannung belastet wird. Dabei werden die Ergebnisse der Simulation mit eindimensionalen analytischen Berechnungen verglichen, wobei sich eine gute Übereinstimmung herausstellt. Zusätzlich wird der Pumpenaktor auch unter Berücksichtigung der Dynamik simuliert.

Ein Nachteil von deformierbaren Dielektrika ist die geringe relative Permittivität, welche zu einer schwachen elektromechanischen Koppelung führt. Da Bariumtitanat eine hohe relative Permittivität besitzt, wird ein Verbundwerkstoff bestehend aus deformierbarem Dielektrikum und Bariumtitanat vorgeschlagen, allerdings auf Kosten einer höheren Steifigkeit, welche durch den Einschluss von Bariumtitanat verursacht wird. Hierzu werden wieder statische und dynamische Berechnungen durchgeführt, um die Vorteile und Nachteile des Verbundwerkstoffes gegenüber eines homogenen Dielektrikums zu zeigen. Insbesondere wird auf die Berücksichtigung der Drei-Feld-Formulierung eingegangen, da

diese für die Modellierung des Verbundwerkstoffes von großer Bedeutung ist. Die Ergebnisse zeigen, dass die Vernachlässigung der Drei-Feld-Formulierung zu volumetrischem „Locking" führt. Dadurch prognostiziert die Simulation des Verbundwerkstoffes eine geringere Kompression als im Fall eines homogenen Dielektrikums. Wird die Drei-Feld-Formulierung jedoch berücksichtigt, kann der Verbundwerkstoff als vorteilhaft betrachtet werden, da höhere Kompressionen als im homogenen Fall berechnet werden.

Abstract

The work at hand focuses on the numerical modeling and the analysis of elastomers which are deformed under the influence of an electric field. These materials are known as dielectric elastomers (DEs) and are used as actuators in order to transform electric energy into mechanical displacements. Furthermore, such materials are often proposed as artificial muscles since the stress and strain range coincides with the extent of biological muscles.

Further practical applications can be found in nature, as for example an airship that imitates the movements of a fish for propulsion. Instead of propellers, dielectric elastomer actuators (DEAs) are attached to the hull and fins of the airship to induce deformations which are similar to those of a swimming fish. Additional application examples are lenses with alterable focus, loudspeakers, pumps, haptic displays or robots. The inverse application is also possible based on a mechanical deformation of the DE in order to transform mechanical energy into electrical.

The main disadvantage of this technology arises from high electric fields that are necessary for sufficient actuations. In the case of haptic displays, voltages of 5 kV are required for a reasonable deformation. In addition, the results of this work show that electric fields of approx. 28 kV/mm are necessary to achieve a compression of 30 %. For this reason, the improvement of DEAs is important to reduce the required electric fields.

To deal with this drawback, a composite which consists of a DE matrix with inclusions of barium titanate is proposed. Hence, necessary aspects of the numerical simulation of those composites as well as DEs are introduced and derived in this work. The performance of DEAs is studied by investigating numerical simulations of benchmark tests. The most important points are the numerical treatment of quasi incompressibility and electromechanical stability.

After a short introduction into the topic of DEs, the fundamentals of nonlinear continuum mechanics are described as these materials are subjected to large deformations. The constitutive laws of neo-Hooke and Yeoh type are introduced. In addition, mechanical

stresses and material tangents are derived from the free energy formulations. In the simulation of nearly incompressible materials, volumetric locking can appear if a pure displacement formulation is considered. To handle this numerical aspect a three field formulation is taken into account.

In a next step the fundamentals of electrostatics are outlined. Starting from Coulomb's law, the definitions of electric and potential fields, Gauss's law and the model of the electric dipole are introduced. Furthermore, the influence of an electric field on polarisable matter is discussed. To this end, the concept of polarisation is required to describe the forces of electric fields on polarisable matter. For a better understanding of the actuation principle of DEAs, the theory of attraction forces between parallel plates of a capacitor in vacuum is outlined. In addition, the concept of the Maxwell stress tensor related to electrostatic volume forces, which are responsible for the DE deformation, is introduced.

To couple mechanics with electrostatics for the description of DEs, the linear momentum balance is reformulated. The total stress is additively composed by a mechanical and an electric part. Considering Gauss's law, the total balance of the electromechanical coupled field problem is established. These equations are recast into the weak form in the reference configuration and then discretized for the numerical implementation. The consistent tangent matrix, which is needed in Newton's method, is derived for the displacement formulation. The symmetry of the matrix is demonstrated, which means that the electromechanic coupled field problem can be derived from a variational formulation. In addition, the discretisation of the three field formulation with the development of the tangent matrix is offered for the modeling of nearly incompressible DEs. Furthermore, the numerical implementation is extended by inertia and damping terms to enable the simulation of DE dynamics.

The compression of a DEA is limited by the electromechanical stability. This limitation is derived from the quadratic dependence of electrostatic attraction forces w.r.t. electric fields. Therefore, the equilibrium of the actuator becomes unstable by exceeding a critical compression point. This point depends on the chosen material model to simulate the behaviour of the DE. In the case of a neo-Hooke model, the critical point is calculated at a compression of approx. 37 %. If a Yeoh model is selected, two critical points will be obtained for 31.9 % and 74.3 % compression. Between these two points an unstable equilibrium region occurs. In this region numerical results are not obtainable since the Newton method does not converge in the solution process. It should be noted, that the critical points only depend on the model and not on the material parameters set for the elastomer. In the present work, the fundamentals of the stability analysis are derived and numerical results are compared to this analysis. A good accordance is obtained considering the numerical compression curves and the stability analysis.

Static and dynamic simulations are performed for homogeneous DEAs. The first example regards an embedded actuator to demonstrate the necessity of the three field formulation for quasi incompressibility. The results show larger deformations using the three field formulation instead of a pure displacement formulation. Additionally, the compression curves are less sensitive to the Poisson's ratio in the quasi incompressible regime. The example of a pump made of DE material bounded by an array of electrode pairs is also simulated. Furthermore, a DEA under constant and time dependent electric loading is considered to study the dynamics. These results are compared to analytical 1D solutions with a good agreement. In addition, simulations of the pump actuator are performed for the dynamic case.

In a DE the electromechanical coupling is limited based on the reduced relative permittivity of the elastomer. Since barium titanate possesses a high relative permittivity, a composite is proposed containing barium titanate inclusions in a DE matrix. However, this composite has an increased stiffness due to the ceramic inclusion. To study the advantages and disadvantages of the composite in comparison to homogeneous DEs, numerical simulations are performed for static and dynamic situations. Special attention is given to the three field formulation, which is important for the modeling of the composite. According to the results, volumetric locking will appear if the three field formulation is neglected, which leads to incorrect predictions of the compression. Applying the three field formulation larger compressions of the composite are obtained in contrast to homogeneous actuators.

Contents

Chapter 1

Introduction

Dielectric elastomers (DEs) are electroactive polymers (EAPs) which constitute the main component in the dielectric elastomer actuator (DEA) technology. The main practical application of the DEA technology is in the field of artificial muscles. This is justified by the similarities of deformation and actuation force range between DEAs and natural muscles. Furthermore, the response rates are very short since the actuation principle consists of a direct coupling of an electric signal to a mechanical deformation. The inspiration for the consideration of DEs as artificial muscles can be found in the human body or in the observation of animal movements. One of the most interesting examples is given by a model airship which flies in the air imitating the movements of a fish, see Fig. 1.1. Instead of a propeller, the airship is equipped with DEAs on the hull and the fin. Another application example with biological inspiration is the heart. Membranes of DE material can be used to build pumps by pushing a fluid via contractions and expansions. Furthermore, the biological eye motivates an alternative for optical systems. Lenses made of DE material are capable of changing their focal point as they are deformed according to an input signal, see Fig. 1.2. Besides the imitation of systems found in nature, DEA can also be considered as substitutes for technical devices. Because of their fast response speed they are good candidates for loudspeakers. For the same reason, active vibration control is another interesting field of application. When it comes to human interaction, they can be also considered for haptic feedback devices or as active braille displays as shown in Fig. 1.3. But actuation technology is not the only field for DE, the reverse application is also possible. This means that they can be used as generators by harvesting energy from movements such as ocean waves or the human body.

Probably the best established technology for converting an electric signal into a mechanical displacement is the electric motor. With the combination of gears and bearings, large forces and displacements are possible. But this facts also limits the application
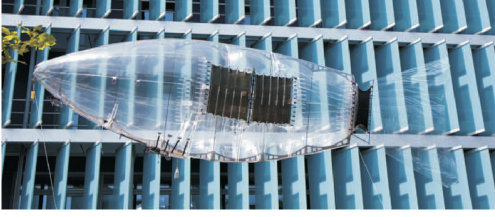
FIGURE 1.1: Airship with DEAs imitating the movements of a fish for propulsion. Source: spie.org.
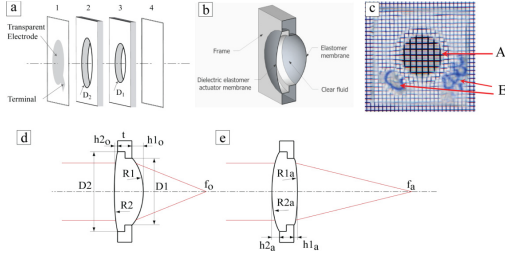
FIGURE 1.2: Concept of a tunable lens with DEAs. Source [1].
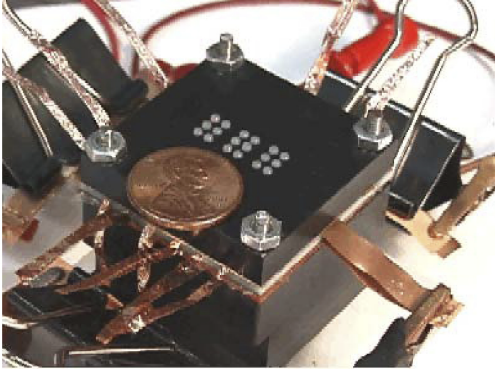
FIGURE 1.3: Prototype of a braille display. The individual dots are activated by a voltage of 5.68 kV. Source [2].

FIGURE 1.4: Arm wrestling robot made of carbon fiber composite and actuated by rolled DEAs. Source [3].

of electric motors, since complex deformations become difficult and costly in combination with these mechanisms. Also piezoceramic actuators are a well known actuation alternative. In this case an electric signal can be directly transformed into a mechanical displacement with the limitation of small deformations. Even though this limitation exists, industrial applications can be found as for example in headphones, microphones, fuel injection systems, pressure and acceleration sensors.

In the last years the interest in EAPs has increased in research and industry. The main reason for this is that EAPs offer the possibility to perform complex deformations with a direct coupling of an electric signal to a deformation. Basically they can be categorised in ionic and electronic. Some examples of ionic EAPs are ionic polymer gels, electro rheological fluids, carbon nanotubes, etc. Since the deformation mechanism is based on the diffusion of ions, an electrolyte liquid is required. Therefore this actuators can only be operated in a wet electrolyte environment but with the advantage of low actuation electric fields. The DE belongs to the category of electronic EAPs where the deformation of the material is induced by an electric field in a dry environment. Besides the DE other elastomers like the ferroelectric, electro-viscoelastic, liquid crystal, etc. also share the category of electronic EAPs. As opposed to the ionic ones, high electric fields are necessary for the actuation. This fact motivates further investigations with the goal

to reduce the electric fields, which is also a topic in the present work. In comparison to the ionic counterpart, the electronic EAP operates with higher actuation forces (but still much lesser than a piezoceramic or an electric motor) and is capable of holding a constant strain under the application of a constant electric voltage.

In the years between 1998 and 2008 Yoseph Bar-Cohen, Roy Kornbluh and Ron Pelrine et. al. motivated, studied and evaluated the use of DEs for actuation purposes like e.g. artificial muscles, see [4–13]. An overview of active polymers for robotic applications is given in [14]. In the year 2005 an arm wrestling contest between a human and an electroactive polymer driven robotic arm took place at the Electroactive Polymer Actuators and Devices conference in San Diego. Even though the robot lost, DE still promise to be a technology in the development of artificial muscles. The details of the robot arm DE actuators which is depicted in Fig. 1.4 can be reviewed in [3].

Some of the earliest works about the electromechanical coupling of elastomers can be found in [15–19]. More than a decade later, an extensive work by Pao [20] was published in which some theories for the formulation of electromagnetic forces on deformable continua are compared. Pao [20] mentions in his work the difficulty of validating a theory because the considered fields are not always measurable in the lab. In the last 15 years much work has been done to describe and analyse the electromechanical coupling of soft elastomers from an analytical perspective. These works established the fundaments for the numerical implementation in the finite element (FE) analysis. Some studies which treat the electromechanical coupling in DEs from a variational perspective can be found in [21–23]. A remarkable series of publications has been given by Dorfmann and Ogden in [24–27]. The first work of this series describes magneto-elasticity while the remaining works are dedicated to the understanding of electro-elasticity. The formulations are stated in dependency of the deformation gradient and electric field or the deformation gradient and electric displacement. Also McMeeking et. al. offer a good overview of the subject applicable for the numerical implementation in the publications [28] and [29]. The works are based on the theories of [30] and a derivation of the Maxwell stress from an energy principle is also given. Suo et. al. provide a theoretical background in the works [31] and [32]. With regard to the numerical implementation and analysis of deformable DEAs some research should be mentioned. One example is given by Gao et. al. [33] in which a general numerical implementation is performed. The works of Vu et. al. [34] and [35] also explain the implementation in the FE context and propose the consideration of the surrounding space of the actuator by a boundary element and finite element method coupling (BEM-FEM). The publications of Ask et. al. [36–38] include the modelling of viscous effects and inverse kinematics. The consideration of quasi-incompressibility has been treated in works like [38] and [39]. Since DEAs consist of thin elastomer sheets,

a shell formulation can be proposed as shown in the work of Klinkel et. al. [40]. Additional research aspects, which have been studied in recent years, are the improvement of the electric breakdown strength, practical applications, experiments, pre-straining, energy minimisation, dynamic response and the characterisation of material parameters in dependency of the deformation. These topics are covered in publications like [41–50]. Finally some PhD theses which are dedicated to the topic of electromechanical coupling and dielectric elastomers can be reviewed in [51–55]. It should be noted that all the mentioned works represent a limited selection of existent publications. For the sake of brevity only those relevant for the present study are cited.

The first purpose of this work is to provide a mathematical description of the electromechanical coupling which takes place in the DE by the consideration of the Maxwell stresses. This description is then recast by means of the Galerkin method for a numerical implementation and further investigation with the finite element method (FEM). Additionally, special attention is given to the fact that DEs are nearly incompressible. To treat this constraint in the numerical implementation, a three field formulation as proposed by Simo, Tyler and Pister, see [56], is considered in the constitutive material law of the DE. In this formulation, the volumetric energy density is decoupled in a first instance from the deformation through the introduction of a variable which represents the volume change. Then, by means of the Lagrange multiplier method, the constraint for the volume change is set to be equal to the Jacobian. The details for the mechanical balance and the material formulation of the DE with the quasi-incompressibility constraint are outlined in chapter 2.

The concept of the Maxwell stress, which represents the key feature in the electromechanical coupling of the DE, is introduced in the last pages of chapter 3. Previously the fundamental concepts and equations for the electrostatic balance in vacuum are defined in this chapter. These concepts are then extended to the electrostatic balance in the dielectric matter and the constitutive law from the electric point of view is established.

After having introduced the fundamental concepts of the DE from the mechanical and electric perspective, the electromechanical coupling is described in the first pages of chapter 4. Afterwards the necessary steps for the numerical implementation are outlined with the derivation of the tangent matrix and the internal load vector for a displacement formulation for compressible materials. To include the incompressibility constraint, the derivation of the internal load vector and the tangent matrix are shown under the consideration of a Q1P0 and a Q2P1 element for the electromechanical coupled problem. The last part of chapter 4 deals with the extension of the quasi-static problem to the dynamic case. By the extension numerical studies of DEAs under an electric cyclic loading are possible.

Before the numerical studies are presented, an analysis of the stability of DEAs is given in chapter 5. Because of the quadratic dependence of the Maxwell stress on the electric field, the compression of the DEA is limited by a critical point at which the equilibrium state of the DEA turns unstable as the applied electric field is increased. This phenomenon is studied in an analytical manner and compared with simulations.

The numerical analysis of the DEA is performed in chapter 6. The chapter is subdivided into studies for the static and the dynamic loading case with the consideration of some benchmarks. A simple sandwich DEA structure is taken into account to study the incompressibility and the dynamic behaviour. Furthermore, a practical application of a pump is motivated with a numerical example.

As mentioned previously, one of the challenges in the conception of EAPs is to increase the ratio between the deformation and the applied electric field. To make this possible, it would be desirable for a DE to have a high dielectric constant which would improve the electromechanical coupling. Since this is not the case for homogeneous materials the proposed strategy is the insertion of inclusions of materials with a high dielectric constant in the elastomer at the cost of an increased stiffness. Chapter 7 presents a numerical investigation and optimisation of the proposed material. Basically the sandwich DEA structure with a spherical inclusion serves as the benchmark in this study. The investigation is performed on the static and dynamic level taking the influence of the incompressibility into account.

Chapter 8 closes the work with concluding remarks and suggestions for future research.

Chapter 2

Continuum Mechanics

This chapter provides an overview of the fundamental concepts and equations of nonlinear continuum mechanics. These are necessary for an adequate description of the deformation of a dielectric elastomer from the mechanical perspective.

The chapter starts with the introduction of the deformation equations and strain measures. After the introduction of stress measures, balance equations are established in their strong and weak form in both configurations. Additionally, a three field formulation is given, which is used in the modelling of nearly incompressible materials. The formulation was proposed first in [56] and considered for finite elasticity in [57] and [58]. It originates from the variational principle of Hu and Washitzu, see [59] and [60]. The last section of the chapter concerns the constitutive laws by postulating the free Helmholtz energy densities for four material models. The stress-strain relations and the elasticity tensors are derived accordingly from these energy formulations.

The theoretical background for this chapter can be found in many textbooks such as [61–66].

2.1   Nonlinear Kinematics

The finite deformation of a material body is described by a nonlinear mapping function χ as shown in Fig. 2.1. A material point P with coordinates $\boldsymbol{X}$ in the reference configuration $\mathcal{B}_0$ is mapped into the current configuration $\mathcal{B}$. In the current configuration the point is represented by p with the coordinates $\boldsymbol{x} = \chi(\boldsymbol{X}, t)$. The displacement of the material point is given by the vector $\boldsymbol{u} = \boldsymbol{x} - \boldsymbol{X}$. The deformation gradient $\boldsymbol{F}$ is introduced to describe the deformation of curves on the material body. It enables the mapping of a tangent vector (line element) of a curve from the reference to the current configuration
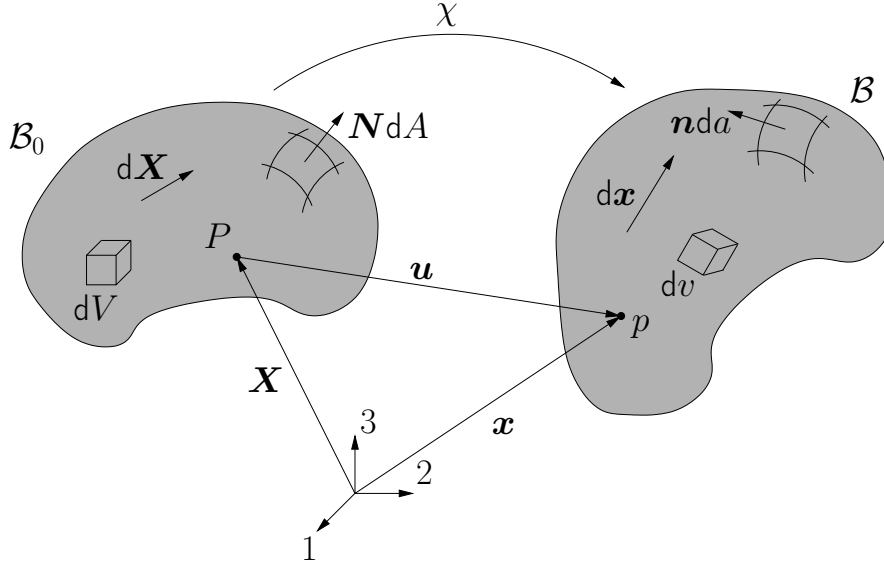
FIGURE 2.1: Nonlinear mapping of the deformation of a material body from reference to current configuration.

according to

$$\mathrm{d}\boldsymbol{x} = \boldsymbol{F}\,\mathrm{d}\boldsymbol{X}, \tag{2.1}$$

where the deformation gradient is defined as

$$\boldsymbol{F} = \frac{\partial \chi(\boldsymbol{X},t)}{\partial \boldsymbol{X}} = \mathrm{Grad}\,\boldsymbol{x}. \tag{2.2}$$

Furthermore, the determinant of the deformation gradient, known as the Jacobian determinant, is introduced by

$$J = \det \boldsymbol{F}. \tag{2.3}$$

The Jacobian determinant J serves as a measure of the volume change between both configurations. For the infinitesimal volume element it follows that

$$\mathrm{d}v = J\,\mathrm{d}V. \tag{2.4}$$

An infinitesimal surface element $\mathrm{d}A$ with the unit normal $\boldsymbol{N}$ is mapped from the reference to the current configuration according to Nanson's formula

$$\boldsymbol{n}\,\mathrm{d}a = J\boldsymbol{F}^{-T}\boldsymbol{N}\,\mathrm{d}A. \tag{2.5}$$

To describe the strain of a material point, appropriate measures are necessary. In this work the right Cauchy-Green tensor $\boldsymbol{C}$ and the Green-Lagrange tensor $\boldsymbol{G}$ are considered. They are defined as

$$\boldsymbol{C} = \boldsymbol{F}^T\boldsymbol{F}, \qquad \boldsymbol{G} = \frac{1}{2}(\boldsymbol{F}^T\boldsymbol{F} - \boldsymbol{I}), \tag{2.6}$$

with $\boldsymbol{I}$ being the second order identity tensor.

In the case of a nearly incompressible deformation, a multiplicative split of the deformation gradient is appropriate. The deformation gradient $\boldsymbol{F}$ is split into an isochoric volume preserving part $\hat{\boldsymbol{F}}$ and a dilatational shape preserving part $\boldsymbol{F}^{vol}$ according to

$$\boldsymbol{F} = \hat{\boldsymbol{F}}\boldsymbol{F}^{vol}. \tag{2.7}$$

With the consideration of $\boldsymbol{F}^{vol} = J^{\frac{1}{3}}\boldsymbol{I}$, the isochoric deformation gradient turns out to be

$$\hat{\boldsymbol{F}} = J^{-\frac{1}{3}}\boldsymbol{F}. \tag{2.8}$$

Furthermore, the isochoric right Cauchy-Green strain tensor $\hat{\boldsymbol{C}}$ is obtained from $(2.6)_1$ and (2.8) by

$$\hat{\boldsymbol{C}} = J^{-\frac{2}{3}}\boldsymbol{C}. \tag{2.9}$$

2.2 Balance Equations

Balance equations are essential to understand the deformation process of a material body under the influence of forces.

The mass conservation of a material body during a deformation is characterised by the change of density. For this purpose the Jacobian determinant J can be used since it describes the volume change of the body, see (2.4). Thus, the density relationship between the configurations is

$$\rho J = \rho_0, \tag{2.10}$$

in which ρ_0 and ρ are the material body densities in the reference and current configuration, respectively.

The next fundamental equation is the conservation of linear momentum. To understand this equation, the concept of the mechanical stress has to be introduced. In the current configuration, according to Cauchy's theorem, there exists an unique second order tensor $\boldsymbol{\sigma}$, known as the Cauchy stress, which fulfills the equation

$$\boldsymbol{t} = \boldsymbol{\sigma}\boldsymbol{n}.\text{[1]} \tag{2.11}$$

In this equation, $\boldsymbol{t}$ is the traction vector on a infinitesimal cross sectional surface of a material body, while $\boldsymbol{n}$ is the outward pointing normal vector to the cross section.

---

[1]The original form of the Cauchy stress states that $\boldsymbol{t} = \boldsymbol{\sigma}^T\boldsymbol{n}$. From the balance of linear/angular momentum it follows that $\boldsymbol{\sigma} = \boldsymbol{\sigma}^T$, which is already used here. The details can be reviewed in [61], [62] and [64].

Taking the angular momentum balance into account it can be shown that $\boldsymbol{\sigma}$ has to be a symmetric tensor. The counterpart of $\boldsymbol{\sigma}$ in the reference configuration is the first Piola-Kirchhoff stress $\boldsymbol{Q}$. Accordingly the Cauchy theorem is given in this configuration by

$$\boldsymbol{T} = \boldsymbol{Q}\boldsymbol{N} \tag{2.12}$$

with $\boldsymbol{T}$ and $\boldsymbol{N}$ being the traction and normal vector respectively. The relation between $\boldsymbol{\sigma}$ and $\boldsymbol{Q}$ is established from the identity

$$\boldsymbol{\sigma}\boldsymbol{n}\,\mathrm{d}a = \boldsymbol{Q}\boldsymbol{N}\,\mathrm{d}A. \tag{2.13}$$

With Nanson's formula (2.5) the first Piola-Kirchhoff stress turns out to be

$$\boldsymbol{Q} = J\boldsymbol{\sigma}\boldsymbol{F}^{-T}. \tag{2.14}$$

Additionally, the second Piola-Kirchhoff stress $\boldsymbol{S}$ is introduced. It is a symmetric tensor with no clear physical interpretation but, it represents a well established stress measure in computational mechanics. It is related to $\boldsymbol{Q}$ according to

$$\boldsymbol{S} = \boldsymbol{F}^{-1}\boldsymbol{Q}. \tag{2.15}$$

With the introduction of mechanical stress measures, the balance of linear momentum at a material point with a body load $\boldsymbol{b}$ can be written in the current configuration

$$\mathrm{div}\,\boldsymbol{\sigma} + \rho\boldsymbol{b} = \boldsymbol{0}. \tag{2.16}$$

With proper transformations the linear momentum balance can be pushed forward into the reference configuration

$$\mathrm{Div}\,\boldsymbol{Q} + \rho_0\boldsymbol{b} = \boldsymbol{0}. \tag{2.17}$$

Equations (2.16) and (2.17) are also known in literature as the strong form of the linear momentum balance. These equations cannot be discretized for a numerical implementation in the FEM context. For this purpose the weak form or principle of virtual work is considered.

Before the weak form is derived, boundary conditions need to be introduced. The boundary of a material body $\mathcal{B}$ is denoted by $\partial\mathcal{B}$ and is composed by two nonintersecting regions

$$\partial\mathcal{B} = \partial\mathcal{B}^u \cup \partial\mathcal{B}^\sigma \quad \text{with} \quad \partial\mathcal{B}^u \cap \partial\mathcal{B}^\sigma = \emptyset. \tag{2.18}$$

To solve the boundary value problem (BVP), conditions have to be prescribed on both regions. The first type are known as Dirichlet boundary conditions and prescribe the

solution field, e.g. $\boldsymbol{u}$ or $\boldsymbol{x}$, on the corresponding boundary region, thus

$$\boldsymbol{u} = \overline{\boldsymbol{u}} \quad \text{on} \quad \partial\mathcal{B}^u. \tag{2.19}$$

The second type, known as von Neumann boundary conditions, define quantities associated to the derivative of the solution field, e.g. the surface traction $\boldsymbol{t}$, on the boundary, thus

$$\boldsymbol{t} = \boldsymbol{\sigma}\boldsymbol{n} = \overline{\boldsymbol{t}} \quad \text{on} \quad \partial\mathcal{B}^\sigma. \tag{2.20}$$

In the current configuration, the weak form of the BVP defined by (2.16), (2.19) and (2.20) is obtained by the multiplication of (2.16) with a virtual displacement $\delta\boldsymbol{u}$ and its integration over the material body $\mathcal{B}$, thus

$$\delta w(\boldsymbol{u}, \delta\boldsymbol{u}) = \int_\mathcal{B} [(\text{div }\boldsymbol{\sigma} + \rho\boldsymbol{b}) \cdot \delta\boldsymbol{u}] \, \mathrm{d}v = 0. \tag{2.21}$$

With the application of the product rule and the divergence theorem the equation can be modified to

$$\delta w(\boldsymbol{u}, \delta\boldsymbol{u}) = \int_\mathcal{B} \boldsymbol{\sigma} : \text{grad }\delta\boldsymbol{u} \, \mathrm{d}v - \int_{\partial\mathcal{B}} \boldsymbol{\sigma}\boldsymbol{n} \cdot \delta\boldsymbol{u} \, \mathrm{d}a - \int_\mathcal{B} \rho\boldsymbol{b} \cdot \delta\boldsymbol{u} \, \mathrm{d}v = 0. \tag{2.22}$$

The Euler-Almansi strain tensor is defined by

$$\boldsymbol{g} = \frac{1}{2}(\boldsymbol{I} - \boldsymbol{F}^{-T}\boldsymbol{F}^{-1}). \tag{2.23}$$

Thus, the first variation of the tensor is

$$\delta\boldsymbol{g} = \frac{1}{2}(\text{grad}^T \delta\boldsymbol{u} + \text{grad }\delta\boldsymbol{u}) = \text{sym}\,(\text{grad }\delta\boldsymbol{u}). \tag{2.24}$$

Since $\boldsymbol{\sigma}$ is a symmetric tensor, (2.24) can be substituted in (2.22). Furthermore, the von Neumann boundary condition (2.20) can also be replaced in the equation and on the boundary $\partial\mathcal{B}^u$ the condition $\delta\boldsymbol{u} = \boldsymbol{0}$ is applied, thus the weak form of the BVP is

$$\delta w(\boldsymbol{u}, \delta\boldsymbol{u}) = \int_\mathcal{B} [\boldsymbol{\sigma} : \delta\boldsymbol{g} - \rho\boldsymbol{b} \cdot \delta\boldsymbol{u}] \, \mathrm{d}v - \int_{\partial\mathcal{B}^\sigma} \overline{\boldsymbol{t}} \cdot \delta\boldsymbol{u} \, \mathrm{d}a = 0. \tag{2.25}$$

In the reference configuration, the statement of the principle of virtual work turns out to be

$$\delta W(\boldsymbol{u}, \delta\boldsymbol{u}) = \int_{\mathcal{B}_0} [\boldsymbol{S} : \delta\boldsymbol{G} - \rho_0\boldsymbol{b} \cdot \delta\boldsymbol{u}] \, \mathrm{d}V - \int_{\partial\mathcal{B}_0^\sigma} \overline{\boldsymbol{T}} \cdot \delta\boldsymbol{u} \, \mathrm{d}A = 0, \tag{2.26}$$

where $\delta\boldsymbol{G}$ is the variation of the Green-Lagrange strain tensor and $\overline{\boldsymbol{T}}$ is the prescribed traction on the boundary of the body in the reference configuration. It should be noted that the Dirichlet boundary condition (2.19) has not been included in the weak forms but is necessary for the solution of the BVP.

2.2.1   Three Field Formulation

The principle of virtual work represents in general a standard approach in mechanics when it comes to the solution of unconstrained displacement problems like compressible materials. For the case of constrained displacement problems, like nearly incompressible materials, this approach leads to the so called volumetric locking phenomenon which renders an undisired stiffening of the system. To handle this situation, so called mixed finite elements are proposed. The methodology of this type of elements arises from a multi-field variational principle which is not only dependent on the displacement field, but also on additional fields. In this work the Jacobian-pressure formulation proposed by Simo, Taylor and Pister, see [56], is considered. In this formulation the free energy density depends on the displacement $\boldsymbol{u}$ and the additional variables p and θ. Under the consideration of $\hat{\boldsymbol{C}}$, see (2.9), the Jacobian-pressure formulation is established as

$$\Psi(\boldsymbol{u}, p, \theta) = \Psi_{iso}(\hat{\boldsymbol{C}}) + \Psi_{vol}(\theta) + p(J - \theta). \tag{2.27}$$

The first term on the right hand side depends only on the isochoric deformation. The second one models the energy which does not depend on J as it would be the case in a displacement formulation, but on an additional variable θ which describes the volume change. The third term is used to enforce the constraint $\theta = J$ by the Lagrange multiplier p, which is the third field in the formulation. To obtain the weak forms from the three field formulation the first variations of the free energy density Ψ w.r.t. $\boldsymbol{u}$, p and θ are required. These first variations are

$$\mathrm{D}_{\delta\boldsymbol{u}}\Psi(\boldsymbol{u}, p, \theta) = \left(Jp\boldsymbol{C}^{-1} + 2\frac{\partial\Psi_{iso}(\hat{\boldsymbol{C}})}{\partial\boldsymbol{C}} \right) : \delta\boldsymbol{G}, \tag{2.28}$$

$$\mathrm{D}_{\delta p}\Psi(\boldsymbol{u}, p, \theta) = (J - \theta)\,\delta p, \tag{2.29}$$

$$\mathrm{D}_{\delta\theta}\Psi(\boldsymbol{u}, p, \theta) = \left(\frac{\partial\Psi_{vol}(\theta)}{\partial\theta} - p \right)\delta\theta. \tag{2.30}$$

The integration of these equations over the material body $\mathcal{B}_0$ gives the internal virtual work in the reference configuration. Under the consideration of external forces, the weak

formulations are obtained

$$\delta W_{\boldsymbol{u}} = \int_{\mathcal{B}_0} \left[\left(Jp\boldsymbol{C}^{-1} + 2\frac{\partial \Psi_{iso}(\hat{\boldsymbol{C}})}{\partial \boldsymbol{C}} \right) : \delta \boldsymbol{G} - \rho_0 \boldsymbol{b} \cdot \delta \boldsymbol{u} \right] \mathrm{d}V$$

$$- \int_{\mathcal{B}_0^{\sigma}} \overline{\boldsymbol{T}} \cdot \delta \boldsymbol{u} \, \mathrm{d}A = 0, \tag{2.31}$$

$$\delta W_p = \int_{\mathcal{B}_0} \left[(J - \theta) \, \delta p \right] \mathrm{d}V = 0, \tag{2.32}$$

$$\delta W_\theta = \int_{\mathcal{B}_0} \left[\left(\frac{\partial \Psi_{vol}(\theta)}{\partial \theta} - p \right) \delta \theta \right] \mathrm{d}V = 0. \tag{2.33}$$

Equation (2.31) represents the weak form which is known from the displacement formulation which has been introduced in (2.26). The difference lies in the second Piola-Kirchhoff stress $\boldsymbol{S}$ which is split in an isochoric and a volumetric part in (2.31). Thus, the two parts are

$$\boldsymbol{S}^{vol} = Jp\boldsymbol{C}^{-1} \quad \text{and} \quad \boldsymbol{S}^{iso} = 2\frac{\partial \Psi_{iso}(\hat{\boldsymbol{C}})}{\partial \boldsymbol{C}}. \tag{2.34}$$

The second weak form in (2.32) represents the constraint for θ to be equal to the Jacobian determinant J while the third weak form in (2.33) renders a constitutive law for p which can be regarded as the hydrostatic pressure.

2.3   Constitutive Laws

For a complete description of the continuum mechanic problem, the kinematic and balance equations are not sufficient. A constitutive law is necessary which describes the mechanical behaviour of a specific material like e.g. steel or rubber. This is realised by a constitutive equation which provides the relation between the mechanical stresses and strains.

For a hyperelastic material the existence of a Helmholtz free energy density Ψ is postulated. If Ψ is only dependent on the mechanical strain, it can be considered as a strain energy or stored energy function. For convenience it is postulated in a form in which it vanishes in the the reference configuration and increases with the deformation of the material body. Furthermore, Ψ is independent of the rotational part of the deformation and only dependent on the stretching part. For this reason, the strain energy function can be written as a function of $\boldsymbol{C}$ or $\boldsymbol{G}$.

In the current work, homogeneous and isotropic materials are considered. The second Piola-Kirchhoff stress, which has been introduced in (2.15), is obtained from the strain energy function according to

$$\boldsymbol{S} = 2\frac{\partial \Psi}{\partial \boldsymbol{C}}. \tag{2.35}$$

For the isotropic case, the stored energy function Ψ can be formulated in dependency of the invariants I, II and III of the strain. For the case of the right Cauchy-Green strain, the second Piola-Kirchhoff becomes

$$\boldsymbol{S} = 2 \left[\left(\frac{\partial \Psi}{\partial \mathrm{I}_{\boldsymbol{C}}} + \mathrm{I}_{\boldsymbol{C}} \frac{\partial \Psi}{\partial \mathrm{II}_{\boldsymbol{C}}} \right) \boldsymbol{1} - \frac{\partial \Psi}{\partial \mathrm{II}_{\boldsymbol{C}}} \boldsymbol{C} + \mathrm{III}_{\boldsymbol{C}} \frac{\partial \Psi}{\partial \mathrm{III}_{\boldsymbol{C}}} \boldsymbol{C}^{-1} \right]. \qquad (2.36)$$

Besides the stress-strain relation, the elasticity tensor $\mathbb{D}$ is needed to describe the change in the stress-strain relation for a nonlinear material. Because of the minor symmetry of $\mathbb{D}$, which results from the symmetry of $\boldsymbol{S}$ and $\boldsymbol{C}$, the tensor has only 36 independent components. If the constitutive law emerges from a free energy function Ψ, the major symmetry is given and the number of components is reduced to 21. The elasticity tensor is obtained from the constitutive law via

$$\mathbb{D} = 2 \frac{\partial \boldsymbol{S}}{\partial \boldsymbol{C}}. \qquad (2.37)$$

In the derivation of $\mathbb{D}$ the partial derivative of $\boldsymbol{C}^{-1}$ w.r.t. $\boldsymbol{C}$ appears and is mentioned here

$$\frac{\partial \boldsymbol{C}^{-1}}{\partial \boldsymbol{C}} = -\mathbb{I}_{\boldsymbol{C}^{-1}}, \qquad (2.38)$$

In index notation this fourth order tensor is

$$\frac{\partial C_{AB}^{-1}}{\partial C_{CD}} = -\mathbb{I}_{\boldsymbol{C}^{-1}\,ABCD} = -\frac{1}{2}(C_{AC}^{-1}C_{BD}^{-1} + C_{AD}^{-1}C_{BC}^{-1}). \qquad (2.39)$$

2.3.1   Displacement Formulation

In the following, three material models are introduced which depend directly on the displacement. The respective strain energy densities are provided and the relations for the stress and elasticity tensors are given.

2.3.1.1   Neo-Hooke

The neo-Hooke model is considered in the mathematical modelling of rubber-like materials. It is motivated by the statistical theory of the long chain molecular network of vulcanised rubber. Because of its simplicity, the model is accurate under uniaxial tension in a strain regime where the strains are under about 40 %, see [67]. For the incompressible case, the mathematical description is based on the first invariant of the strain $\mathrm{I}_{\boldsymbol{C}}$ and the shear modulus G as a material parameter. In the case of compressibility, the model is extended by the determinant J which describes the change in volume and the bulk modulus K is introduced as a second material parameter. Furthermore, expansion and compression limitation conditions can be applied to the model. This implies that

the strain energy has to go towards infinity if the material is compressed to a vanishing volume or expanded towards infinity. A model in which these conditions are satisfied was proposed in [68] and is expressed by

$$\Psi(\text{I}_{\boldsymbol{C}}, J) = \frac{1}{2}\mu(\text{I}_{\boldsymbol{C}} - 3) + \frac{\lambda}{4}(J^2 - 1) - \frac{\lambda}{2}\ln J - \mu\ln J. \tag{2.40}$$

Here the Lamé parameters λ and μ are taken into account which are related to the bulk modulus K and the shear modulus G. By considering (2.35) and (2.36) the second Piola-Kirchhoff stress is obtained

$$\boldsymbol{S} = \frac{\lambda}{2}(J^2 - 1)\boldsymbol{C}^{-1} + \mu(\boldsymbol{1} - \boldsymbol{C}^{-1}). \tag{2.41}$$

Furthermore, by using the definition (2.37) one obtains the elasticity tensor

$$\mathbb{D} = \lambda J^2 \boldsymbol{C}^{-1} \otimes \boldsymbol{C}^{-1} + [2\mu - \lambda(J^2 - 1)]\mathbb{I}_{\boldsymbol{C}^{-1}}. \tag{2.42}$$

2.3.1.2 Neo-Hooke with Volumetric Split

The neo-Hooke model can be modified by an additive split of the strain energy. The purpose of this split is to separate the volumetric and isochoric parts of the strain energy. Therefore the isochoric right Cauchy-Green tensor $\hat{\boldsymbol{C}}$, which was introduced in (2.9), and the dilatation, which is described by J, are considered. In (2.43) the first term on the right hand side represents the isochoric part of the energy. Comparing to the first term in the standard neo-Hooke model, see (2.40), $\text{I}_{\boldsymbol{C}}$ is replaced by $\text{I}_{\hat{\boldsymbol{C}}}$. With this, the first term is only affected by pure isochoric deformations. The second one is affected by the dilatation of the material since it only depends on J. It should be mentioned here that the second term does not grow to infinity if J approaches 0 but for the nearly incompressible case it is sufficient, since $J \approx 1$. Furthermore, the nearly incompressible behaviour is established in this model by a high constant K. This means that a slight increase in volume will lead to a high strain energy,

$$\Psi(\text{I}_{\hat{\boldsymbol{C}}}, J) = \frac{1}{2}\mu(\text{I}_{\hat{\boldsymbol{C}}} - 3) + \frac{1}{2}K(J - 1)^2 = \Psi_{iso} + \Psi_{vol}. \tag{2.43}$$

The second Piola-Kirchhoff stress is obtained with the definition (2.35). Since Ψ is composed of two parts, $\boldsymbol{S}$ can be obtained in a split form according to

$$\boldsymbol{S}^{iso} = 2\frac{\partial\Psi_{iso}}{\partial\boldsymbol{C}} = \mu J^{-\frac{2}{3}}\left(\boldsymbol{1} - \frac{1}{3}\text{I}_{\boldsymbol{C}}\boldsymbol{C}^{-1}\right), \tag{2.44}$$

$$\boldsymbol{S}^{vol} = 2\frac{\partial\Psi_{vol}}{\partial\boldsymbol{C}} = KJ(J - 1)\boldsymbol{C}^{-1}. \tag{2.45}$$

This procedure is also valid for the elasticity tensor, which is additively split in an isochoric and a volumetric part,

$$
\begin{aligned}
\mathbb{D}^{iso} &= 2\frac{\partial \boldsymbol{S}_{iso}}{\partial \boldsymbol{C}} \\
&= \frac{2}{3}\mu J^{-\frac{2}{3}}\left[\mathrm{I}_{\boldsymbol{C}}\left(\mathbb{I}_{\boldsymbol{C}^{-1}} + \frac{1}{3}\boldsymbol{C}^{-1}\otimes\boldsymbol{C}^{-1}\right) - \left(\boldsymbol{1}\otimes\boldsymbol{C}^{-1} + \boldsymbol{C}^{-1}\otimes\boldsymbol{1}\right)\right], \quad (2.46)
\end{aligned}
$$

$$
\begin{aligned}
\mathbb{D}^{vol} &= 2\frac{\partial \boldsymbol{S}_{vol}}{\partial \boldsymbol{C}} \\
&= KJ\left[(2J-1)\,\boldsymbol{C}^{-1}\otimes\boldsymbol{C}^{-1} - 2\,(J-1)\,\mathbb{I}_{\boldsymbol{C}^{-1}}\right]. \quad (2.47)
\end{aligned}
$$

2.3.1.3 Yeoh

If a rubber-like material is deformed in the large strain domain, it can be observed that the tangent shear decreases at the beginning and then increases as the strain advances. One can speak of a stiffening effect in the large strain range. To model this effect, Yeoh proposed a model which is also called reduced polynomial model. For the incompressible case, this model is a three term expansion of the incompressible neo-Hooke model, which depends on the first invariant $\mathrm{I}_{\boldsymbol{C}}$, see [69]. For the case of nearly incompressible materials, the kinematic split of a volumetric and isochoric deformation is considered. The isochoric terms depend on the isochoric first invariant $\mathrm{I}_{\hat{\boldsymbol{C}}}$ and the volumetric part is related to the Jacobi determinant J. Thus, the Yeoh model can be defined by

$$
\Psi(\mathrm{I}_{\hat{\boldsymbol{C}}}, J) = \sum_{i=1}^{3}c_i(\mathrm{I}_{\hat{\boldsymbol{C}}} - 3)^i + \sum_{k=1}^{3}\frac{1}{d_k}(J-1)^{2k}. \quad (2.48)
$$

In this model c_1 can be regarded as half the initial shear modulus μ. For the sake of simplicity the volumetric part can be reduced to the first term with $\frac{1}{d_1}$ being half the bulk modulus

$$
\Psi(\mathrm{I}_{\hat{\boldsymbol{C}}}, J) = \sum_{i=1}^{3}c_i(\mathrm{I}_{\hat{\boldsymbol{C}}} - 3)^i + \frac{1}{2}K(J-1)^2. \quad (2.49)
$$

Using (2.35) the second Piola-Kirchhoff stress is obtained,

$$
\boldsymbol{S} = 2h_1 J^{-\frac{2}{3}}\boldsymbol{1} - \frac{2}{3}h_1 J^{-\frac{2}{3}}\mathrm{I}_{\boldsymbol{C}}\boldsymbol{C}^{-1} + KJ(J-1)\boldsymbol{C}^{-1}, \quad (2.50)
$$

with

$$
h_1 = c_1 + 2c_2(\mathrm{I}_{\hat{\boldsymbol{C}}} - 3) + 3c_3(\mathrm{I}_{\hat{\boldsymbol{C}}} - 3)^2. \quad (2.51)
$$

Furthermore, the elasticity tensor is obtained from (2.37). As it can be seen in (2.50), the second Piola-Kirchhoff stress $\boldsymbol{S}$ for the Yeoh model is composed of three terms. For a better overview, the elasticity tensor is also split into three parts which correspond to

the three terms of $\boldsymbol{S}$, thus

$$\mathbb{D} = \mathbb{D}^a + \mathbb{D}^b + \mathbb{D}^c. \tag{2.52}$$

This three terms are

$$\mathbb{D}^a = 4h_2 J^{-\frac{4}{3}} \mathbf{1} \otimes \mathbf{1} - \frac{4}{3} J^{-\frac{4}{3}} (\mathrm{I}_{\boldsymbol{C}} h_2 + J^{\frac{2}{3}} h_1) \boldsymbol{C}^{-1} \otimes \mathbf{1}, \tag{2.53}$$

$$\mathbb{D}^b = -\frac{4}{3} J^{-\frac{2}{3}} \mathrm{I}_{\boldsymbol{C}} \left[\left(J^{-\frac{2}{3}} h_2 + \frac{h_1}{\mathrm{I}_{\boldsymbol{C}}} \right) \mathbf{1} \otimes \boldsymbol{C}^{-1} \right]$$
$$+ \frac{4}{3} J^{-\frac{2}{3}} \mathrm{I}_{\boldsymbol{C}} \left[\frac{1}{3} (J^{-\frac{2}{3}} \mathrm{I}_{\boldsymbol{C}} + h_1) \boldsymbol{C}^{-1} \otimes \boldsymbol{C}^{-1} + h_1 \mathbb{I}_{\boldsymbol{C}^{-1}} \right], \tag{2.54}$$

$$\mathbb{D}^c = 2KJ \left[\left(J - \frac{1}{2} \right) \boldsymbol{C}^{-1} \otimes \boldsymbol{C}^{-1} - (J - 1) \mathbb{I}_{\boldsymbol{C}^{-1}} \right]. \tag{2.55}$$

2.3.2 Three Field Formulation

As mentioned previously, the consideration of nearly incompressible materials requires a special treatment which can be solved by use of a three field formulation as introduced in section 2.2.1. Based on the neo-Hooke with split formulation given in (2.43), the three field formulation in (2.27) can be rewritten as

$$\Psi(\boldsymbol{u}, p, \theta) = \frac{1}{2} \mu (\mathrm{I}_{\hat{\boldsymbol{C}}} - 3) + \frac{1}{2} K (\theta - 1)^2 + p(J - \theta). \tag{2.56}$$

The first term on the right hand side describes the isochoric part of the energy while the second term models the volumetric part. The third term serves as the constraint for θ. Since the isochoric energy parts of (2.56) and (2.43) are identical, the corresponding part of the second Piola-Kirchhoff stress remains unchanged,

$$\boldsymbol{S}^{iso} = \mu J^{-\frac{2}{3}} \left(\mathbf{1} - \frac{1}{3} \mathrm{I}_{\boldsymbol{C}} \boldsymbol{C}^{-1} \right). \tag{2.57}$$

The volumetric part of the second Piola-Kirchhoff stress is different and turns out to be

$$\boldsymbol{S}^{vol} = p J \boldsymbol{C}^{-1}. \tag{2.58}$$

Analogously to the derivation described in section 2.3.1.2, the elasticity tensor is composed by its isochoric and volumetric part,

$$\mathbb{D}^{iso} = \frac{2}{3} \mu J^{-\frac{2}{3}} \left[\mathrm{I}_{\boldsymbol{C}} \left(\mathbb{I}_{\boldsymbol{C}^{-1}} + \frac{1}{3} \boldsymbol{C}^{-1} \otimes \boldsymbol{C}^{-1} \right) - \left(\mathbf{1} \otimes \boldsymbol{C}^{-1} + \boldsymbol{C}^{-1} \otimes \mathbf{1} \right) \right], \tag{2.59}$$

$$\mathbb{D}^{vol} = p J \left(\boldsymbol{C}^{-1} \otimes \boldsymbol{C}^{-1} - 2 \mathbb{I}_{\boldsymbol{C}^{-1}} \right). \tag{2.60}$$

Here the isochoric part is identical to the one of the neo-Hooke with split formulation, see (2.46).

Chapter 3

Electrostatics in Dielectric Materials

Electrostatics is the part of physics which studies the phenomena produced by electric charges at rest. For the explanation and understanding of these macroscopic phenomena, which are originated at the atomistic level, the concept of point charges is used.

The aim of this chapter is to give an introduction to the electrostatic concepts which are necessary for the description of DEs. The chapter begins by introducing Coulomb's and Gauss's law in vacuum. Furthermore, the concept of electric and potential fields produced by charges in vacuum is described. Afterwards the electric dipole is introduced as the starting point to describe the polarisation. The concept of polarisation is then used to explain the electrostatic forces which act on matter and are responsible for deformations. Additionally the electric displacement is introduced to state an electrostatic constitutive law. To motivate the actuation mechanism of DEAs, a simple analysis of a parallel plate capacitor in vacuum is performed considering two approaches. The idea is to explain the forces on the plates of a capacitor in dependency of the electric field. The chapter is closed by defining the Maxwell stress for vacuum and matter. The relationship between the stress and the electrostatic volume force is shown. This relationship serves for the balance description of the electromechanical coupled field problem.

Several books and sources on the topic of electrostatic can be found in literature as introductory material. The concepts and ideas shown in this work are based on [70]. In addition, the references [30, 71–74] have also been considered as complementary literature.

3.1 Electric Fields in Vacuum

Coulomb's law states, that the force on a test charge Q created by a source charge q is given by the relationship

$$\boldsymbol{F}^E = \frac{1}{4\pi\epsilon_0} \frac{qQ}{|\boldsymbol{r}|^3} \boldsymbol{r}. \tag{3.1}$$

In this equation ϵ_0 is the permittivity of free space and $\boldsymbol{r}$ is the distance vector between the charges Q and q. As it can be observed in the equation, the force vector acts along the distance vector $\boldsymbol{r}$. Furthermore, the sign of both charges is responsible for the force direction. If both charges have the same sign, the force is repulsive, otherwise it is attractive.
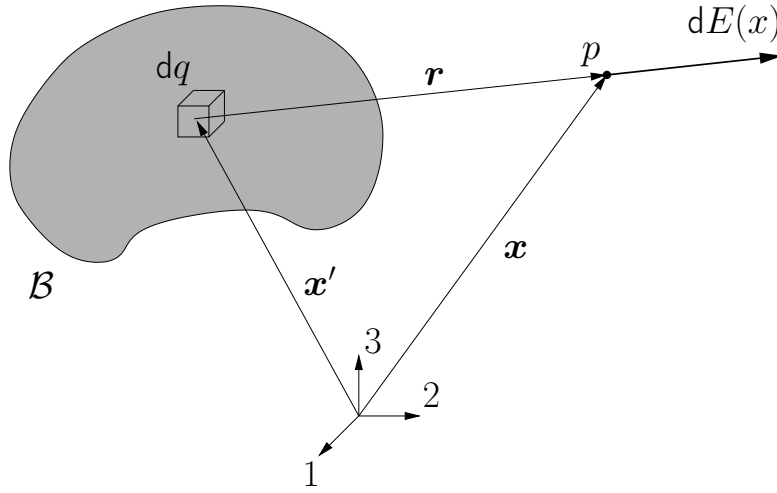
FIGURE 3.1: Electric field at point p created by a charged Body $\mathcal{B}$.

To describe the forces created by a volume charge distribution on a test charge, the concept of the electric field is introduced. The electric field created by a charged body $\mathcal{B}$ at a point p, see Fig. 3.1, is defined as

$$\boldsymbol{E}(\boldsymbol{x}) = \frac{1}{4\pi\epsilon_0} \int_{\mathcal{B}} \frac{\gamma(\boldsymbol{x}')}{|\boldsymbol{r}|^3} \boldsymbol{r} \, \mathrm{d}v, \tag{3.2}$$

where $\gamma = \mathrm{d}q/\mathrm{d}v$ is the charge density of a point with coordinates $\boldsymbol{x}'$ belonging to $\mathcal{B}$. The distance between the charge density point γ and the measuring point p is described by the vector $\boldsymbol{r}$.

A test charge Q which is located in an electric field $\boldsymbol{E}$ is subjected to a force

$$\boldsymbol{F}^E = Q\boldsymbol{E}. \tag{3.3}$$

Gauss's law states that the flux of the electric field $\boldsymbol{E}$ through any closed surface $\mathcal{S}$ is proportional to the total electric charge Q_{enc} enclosed by the given surface according to

$$\oint_{\mathcal{S}} \boldsymbol{E} \cdot \boldsymbol{n} \, \mathrm{d}a = \frac{1}{\epsilon_0} Q_{enc}. \tag{3.4}$$

In this equation the unit normal vector at an infinitesimal surface $\mathrm{d}a$ is given with $\boldsymbol{n}$. Considering the definition of the charge density, the enclosed charge can be written as

$$Q_{enc} = \int_{\mathcal{V}} \gamma \, \mathrm{d}v. \tag{3.5}$$

Substituting (3.5) in (3.4) and under the consideration of the divergence theorem, the differential form of Gauss's law is obtained with

$$\mathrm{div}\, \boldsymbol{E} = \frac{\gamma}{\epsilon_0}. \tag{3.6}$$

One special property of electric fields created by static charges is that they are curl-free. This means that the rotation vanishes, thus rot $\boldsymbol{E} = \boldsymbol{0}$. For this reason it is possible to define the electric field $\boldsymbol{E}$ as the gradient of a scalar field. This scalar field is known as the electric potential φ and fulfils the relationship

$$\boldsymbol{E} = -\mathrm{grad}\, \varphi, \tag{3.7}$$

where the negative sign is just a convention. The unit of φ is joule per coulomb which is known as volt. The electric potential field created by a single point charge or monopole q is given by the equation

$$\varphi(\boldsymbol{r}) = \frac{1}{4\pi\epsilon_0} \frac{q}{|\boldsymbol{r}|}, \tag{3.8}$$

where $\boldsymbol{r}$ is the distance vector from charge q to a given point in space. It should be noted, that the electric potential field of a monopole decreases with $1/|\boldsymbol{r}|$.
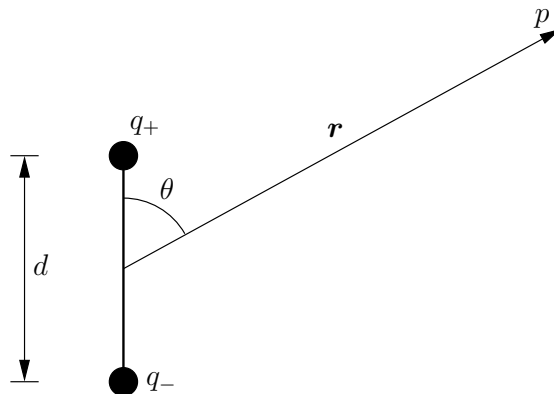

FIGURE 3.2: Scheme of an electric dipole.

An electric dipole is a set of two point charges with opposite charges, q_+ and q_-, which are separated by the distance d, see Fig. 3.2. The electric potential field φ of this arrangement can be obtained via the superposition principle. Under the assumption that d is considerably smaller than the distance $\boldsymbol{r}$, the electric potential at point p is obtained with

$$\varphi(\boldsymbol{r}) = \frac{1}{4\pi\epsilon_0} \frac{qd\cos\theta}{|\boldsymbol{r}|^2}. \tag{3.9}$$

In comparison to a monopole, the electric potential of a dipole decreases faster with $1/|\boldsymbol{r}|^2$. The product qd is known as the magnitude of the dipole moment. The dipole distance vector $\boldsymbol{d}$ is defined as the vector which points from q_- to q_+. Thus, the dipole moment vector can be given by

$$\boldsymbol{p} = q\boldsymbol{d}. \tag{3.10}$$

Considering (3.10) in (3.9) one obtains the electric potential as a function of the dipole moment vector

$$\varphi(\boldsymbol{r}) = \frac{\boldsymbol{r} \cdot \boldsymbol{p}}{4\pi\epsilon_0|\boldsymbol{r}|^3}. \tag{3.11}$$

The electric field of the dipole is obtained by the application of (3.7) on (3.9). Considering polar coordinates $|\boldsymbol{r}|$ and θ, the radial and tangential components are

$$E_r = \frac{2|\boldsymbol{p}|\cos\theta}{4\pi\epsilon_0|\boldsymbol{r}|^3}, \quad E_\theta = \frac{|\boldsymbol{p}|\sin\theta}{4\pi\epsilon_0|\boldsymbol{r}|^3}. \tag{3.12}$$

3.2 Electric Fields in Matter

When a neutral atom or molecule is subjected to an electric field, the positive and negative charges are separated due to Coulomb's force and dipoles are formed. If the magnitude of the electric field is rather small, the moment of the dipole $\boldsymbol{p}$ becomes proportional to the applied electric field $\boldsymbol{E}$. In the case of a homogeneous field, the forces on the charges of the dipole cancel each other out and no net force acts on the dipole. If the electric field is heterogeneous, the forces on the charges of the dipole are not equal and opposite anymore, see Fig. 3.3. The net force which acts on the dipole is then defined as

$$\boldsymbol{F}^E = \boldsymbol{F}_+^E + \boldsymbol{F}_-^E = q\boldsymbol{E}_+ - q\boldsymbol{E}_- = q(\boldsymbol{E}_+ - \boldsymbol{E}_-) = q(\Delta\boldsymbol{E}). \tag{3.13}$$

On the infinitesimal length scale the difference of the electric field $\Delta\boldsymbol{E}$ on the dipole charges can be obtained according to

$$\Delta\boldsymbol{E} = (\operatorname{grad}\boldsymbol{E})\boldsymbol{d}. \tag{3.14}$$
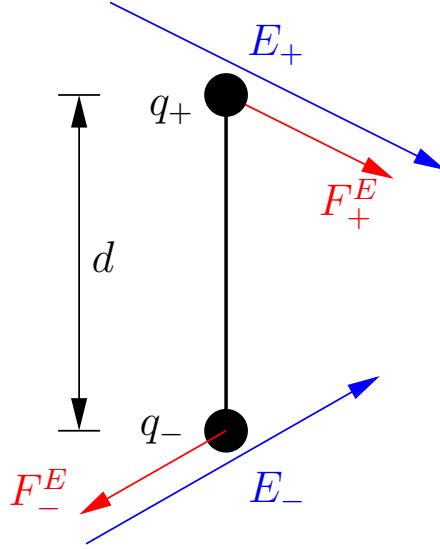
FIGURE 3.3: Electrostatic forces of a heterogeneous electric field on a dipole.

With the substitution of (3.14) in (3.13) the net force of a heterogeneous electric field on a dipole yields

$$\boldsymbol{F}^E = (\operatorname{grad} \boldsymbol{E})q\boldsymbol{d} = (\operatorname{grad} \boldsymbol{E})\boldsymbol{p}. \tag{3.15}$$

Since a continuum body consists of a large number of atoms and molecules, the concept of an atomistic or molecular dipole can be transferred to the macroscopic scale by the means of a continuum material body. To facilitate the description on a macroscopic scale, the concept of polarisation is introduced as the dipole moment per unit volume

$$\boldsymbol{P} = \frac{\boldsymbol{p}}{v}. \tag{3.16}$$

Multiplying (3.15) with $1/v$, the electrostatic volume force of an electric field on dielectric material is obtained by

$$\boldsymbol{f}^E = \frac{\boldsymbol{F}^E}{v} = (\operatorname{grad} \boldsymbol{E})\boldsymbol{P}. \tag{3.17}$$

This expression can be regarded as a physical interpretation of the electrostatic force which acts on polarisable materials like DEs under the influence of an electric field. So far, the concept of polarisation has been described very briefly even tough it is an important factor for the understanding of the deformation of dielectric materials. For this reason the electrostatic volume force introduced in (3.17) is set aside for the moment and will be recaptured in section 3.4 where the concept of the Maxwell stress is presented.

As mentioned in the beginning of this section, a dielectric becomes polarised if it is exposed to an electric field by forming dipoles $\boldsymbol{p}$ on the atomistic and molecular level. To evaluate the potential field created by these dipoles, (3.11) and (3.16) have to be considered. With the integration of (3.11) over the polarised volume and the appropriate

manipulations described in [70] the definition of bound surface and volume charges can be applied. These definitions are

$$\alpha_b = \boldsymbol{P} \cdot \boldsymbol{n}, \qquad \gamma_b = -\mathrm{div}\,\boldsymbol{P}. \tag{3.18}$$

In a dielectric, the electric charges are not able to move as freely as in a conductor. For this reason, the charges in these materials are considered as bound charges. The respective surface and volume densities of the bound charges are represented with α_b and γ_b. For a physical interpretation of these charges, the reader is referred to [70]. By these means, the potential field produced by polarised matter can be obtained in dependency of the bound charges in the material,

$$\varphi(\boldsymbol{r}) = \frac{1}{4\pi\epsilon_0} \oint_{\mathcal{S}} \frac{\alpha_b}{|\boldsymbol{r}|}\mathrm{d}a + \frac{1}{4\pi\epsilon_0} \int_{\mathcal{V}} \frac{\gamma_b}{|\boldsymbol{r}|}\mathrm{d}v. \tag{3.19}$$

Since the potential field is known, the electric field can also be obtained according to (3.7). The concept of potential and electric polarisation fields attributed to bound charges can be transferred to external fields. In this case, the free charges with density γ_f are held responsible for the creation of the external electric field which is the case for the conducting electrodes of a capacitor. Under this perspective, the total electric field in a dielectric, which is composed of the external and the polarisation part, can be attributed to the sum of bound and free charges. Thus the total volume charge density responsible for the entire field is

$$\gamma = \gamma_b + \gamma_f. \tag{3.20}$$

Using Gauss's law (3.6) and (3.18)$_2$ one obtains that

$$\mathrm{div}\,(\epsilon_0 \boldsymbol{E} + \boldsymbol{P}) = \gamma_f, \tag{3.21}$$

in which the term in parenthesis is defined as the electric displacement in polarisable matter,

$$\boldsymbol{D} = \epsilon_0 \boldsymbol{E} + \boldsymbol{P}. \tag{3.22}$$

With this, Gauss's law for dielectric materials is stated by

$$\mathrm{div}\,\boldsymbol{D} = \gamma_f. \tag{3.23}$$

The last issue wich has to be treated in the theory of polarisable matter is the polarisability of dielectrics. In continuum mechanics, materials are generally characterised in first place by the stress-strain relation. The most simple relation is the linear, which can often be applied at small strains. In the same manner the polarisation of a dielectric can

be related to the electric field under the assumption of smaller fields in a linear way

$$\boldsymbol{P} = \epsilon_0 \chi \boldsymbol{E}. \tag{3.24}$$

In this equation χ is known as the electric susceptibility. It should be noted that the polarisation cannot be obtained directly from the applied electric field. The total electric field depends partially on the applied electric field and on the electric field created by the polarisation of the material, which is created by the application of an external electric field. Inserting (3.24) in (3.22) leads to

$$\boldsymbol{D} = \epsilon_0 (1 + \chi)\boldsymbol{E} = \epsilon \boldsymbol{E}. \tag{3.25}$$

Obviously the electric displacement is proportional to the electric field. The proportionality factor ϵ is known as the permittivity of the dielectric. The relative permittivity ϵ_r is defined as the relation between the permittivity ϵ and the permittivity of the free space ϵ_0. It is related to the susceptibility according to

$$\epsilon_r = 1 + \chi = \frac{\epsilon}{\epsilon_0}. \tag{3.26}$$

3.3   Forces in Parallel Plate Capacitors

This section presents a physical interpretation of the forces which appear in a parallel plate capacitor as a consequence of the electric field produced by charge distributions. For this purpose two approaches are given in which the first one is based on Coulomb's law while the second one considers the work and energy in the capacitor.

3.3.1   Force Balance Approach

The electric field $\boldsymbol{E}$ created by one plate of a capacitor can be calculated by Gauss's law. The surface charge density of a plate is given by α. For a given surface A of the plate (blue surface in Fig. 3.4) the total charge is $Q_A = \alpha A$. The electric field created by the surface charge distribution is perpendicular to the surface since the components of $\boldsymbol{E}$, which are parallel to the surface, cancel each other out. To calculate the electric field, the surface A is enclosed by a "Gaussian pillbox", see Fig. 3.4. According to Gauss's law (3.4), the electric field fulfils the equation

$$\oint_{\mathcal{S}} \boldsymbol{E} \cdot \boldsymbol{n} \, \mathrm{d}a = \frac{1}{\epsilon_0} Q_A = \frac{\alpha A}{\epsilon_0}. \tag{3.27}$$
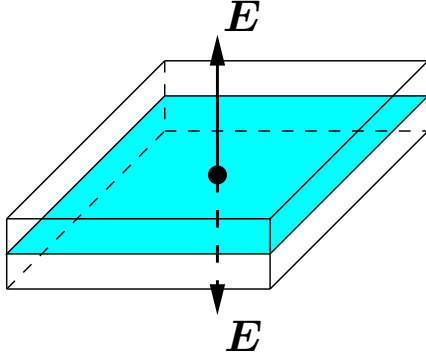
FIGURE 3.4: Electric field created by a charged surface (blue) with enclosing "Gaussian pillbox".
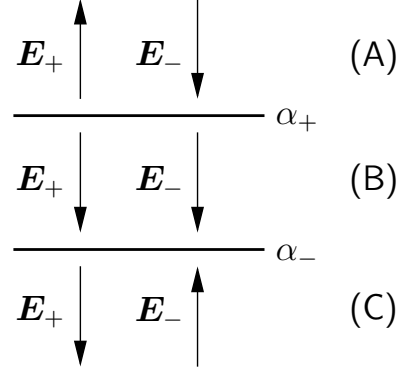

FIGURE 3.5: Electric field created by a charged parallel plate capacitor.

The integration along the lateral faces of the box can be neglected, since the electric field is perpendicular to the plate. The surface integral along the top and the bottom face is

$$\int \boldsymbol{E} \cdot \boldsymbol{n} \, \mathrm{d}a = 2A|\boldsymbol{E}|. \tag{3.28}$$

Taking (3.27) and (3.28) delivers the electric field of the charged plate

$$\boldsymbol{E} = \frac{\alpha}{2\epsilon_0} \boldsymbol{n}, \tag{3.29}$$

in which $\boldsymbol{n}$ is the normal unit vector to the charged plate. With the knowledge of $\boldsymbol{E}$ for a charged plate, the electric field inside a parallel plate capacitor can be calculated. The scheme of a capacitor is represented in Fig. 3.5. The top and bottom electrodes are charged with densities α_+ and α_-. Both plates create the electric fields $\boldsymbol{E}_+$ and $\boldsymbol{E}_-$ which point in the directions shown in Fig. 3.5. The field $\boldsymbol{E}_+$ is created by the top electrode and $\boldsymbol{E}_-$ is created by the bottom one. The magnitude of the field is obtained with (3.29). Outside of the capacitor (region A and C) the electric fields of both plates cancel out because of their opposite direction. Inside the capacitor (region B), the fields of both plates add up, thus the magnitude of the electric field in a parallel plate capacitor is

$$|\boldsymbol{E}| = \frac{\alpha}{\epsilon_0}. \tag{3.30}$$

Now that the electric field is known, the force acting on the plates of the capacitor can be calculated with (3.3). Since the electric field is discontinuous at the surface charge α, the average of the electric field at both sides of the surface has to be taken. Furthermore, a force per unit area is obtained because of the consideration of a charge density. With this, the force per unit area on the plate of a capacitor is

$$\boldsymbol{f}^E = \frac{1}{2}\alpha(\boldsymbol{E}_{above} + \boldsymbol{E}_{below}) = \frac{1}{2}\alpha(\boldsymbol{E} + \boldsymbol{0}) = \frac{1}{2}\alpha\boldsymbol{E}. \tag{3.31}$$

To obtain the force in dependency of ϵ_0 (3.30) is inserted in (3.31), thus

$$|\boldsymbol{f}^E| = \frac{1}{2}\epsilon_0 |\boldsymbol{E}|^2. \tag{3.32}$$

3.3.2 Energy Approach

The attraction force between the parallel plates of a capacitor can also be obtained by the consideration of the energy of the system. In general, the electrostatic energy of a system with a charge density γ and electric potential φ can be obtained by the volume integration over the whole system according to

$$\Psi = \frac{1}{2}\int_{\mathcal{V}} \gamma\varphi \, \mathrm{d}v. \tag{3.33}$$

The charge density γ can be substituted with the consideration of Gauss's law described in (3.6), thus

$$\Psi = \frac{1}{2}\epsilon_0 \int_{\mathcal{V}} (\mathrm{div}\,\boldsymbol{E})\varphi \, \mathrm{d}v. \tag{3.34}$$

Integration by parts yields

$$\Psi = \frac{1}{2}\epsilon_0 \left[-\int_{\mathcal{V}} \boldsymbol{E} \cdot (\mathrm{grad}\,\varphi) \, \mathrm{d}v + \oint_{\mathcal{S}} \varphi\boldsymbol{E} \cdot \boldsymbol{n} \, \mathrm{d}a \right]. \tag{3.35}$$

This equation can be further modified by substituting the gradient of the electric potential from (3.7) into (3.35), thus

$$\Psi = \frac{1}{2}\epsilon_0 \left(\int_{\mathcal{V}} |\boldsymbol{E}|^2 \, \mathrm{d}v + \oint_{\mathcal{S}} \varphi\boldsymbol{E} \cdot \boldsymbol{n} \, \mathrm{d}a \right). \tag{3.36}$$

This is the general form to obtain the energy of a charge distribution under the consideration of the electric field and potential created by the charge distribution. It should be noted that the integration has to be done over a region which encloses the charge distribution. It is not necessary to enclose the system perfectly, the enclosure can be larger as long as it contains the system.

In the case of the parallel plate capacitor the surface integral term can be neglected since the electric field is only present between the plates of the capacitor and therefore does not pass through the enclosure.

Considering a capacitor with the surface area A and a plate separation distance l, the energy of the system can be obtained with (3.36) yielding

$$\Psi = \frac{1}{2}\epsilon_0 |\boldsymbol{E}|^2 Al. \tag{3.37}$$

The work W of an external force $\boldsymbol{F}^E$ which separates the plates of the capacitor is stored as an internal energy of the system, thus

$$W = \Psi. \tag{3.38}$$

The external force can be obtained by the partial derivative of the work w.r.t. the separation distance of the plates. With (3.37) and (3.38) one obtains

$$|\boldsymbol{F}^E| = \frac{\partial W}{\partial l} = \frac{\partial \Psi}{\partial l} = \frac{1}{2}\epsilon_0 |\boldsymbol{E}|^2 A. \tag{3.39}$$

Thus, the force per unit surface is

$$|\boldsymbol{f}^E| = \frac{|\boldsymbol{F}^E|}{A} = \frac{1}{2}\epsilon_0 |\boldsymbol{E}|^2, \tag{3.40}$$

which agrees with the previously obtained result in (3.32).

3.4   Maxwell Stress and Electrostatic Volume Force

The Maxwell stress was first introduced in the treatise by Maxwell in the mathematical derivation of electromagnetic forces on electric charges, see [75]. Initially the concept of the Maxwell stress was developed for forces on charges in vacuum. Afterwards it has been extended for the evaluation of forces in polarisable matter.

In continuum mechanics the divergence of the Cauchy stress is balanced by mechanical volume loads like e.g. gravity if surface tractions are neglected. The same idea can also be applied to the Maxwell stress, whose divergence is balanced by the electrostatic volume force, see [76] and [77].

The definition of the Maxwell stress is considered here for the electrostatic case which means that the electrodynamic terms are neglected. Furthermore, two distinctions are made, namely the vacuum and the dielectric media case. In vacuum the Maxwell stress is given by

$$\boldsymbol{\sigma}^E = \epsilon_0 \left[\boldsymbol{E} \otimes \boldsymbol{E} - \frac{1}{2}(\boldsymbol{E} \cdot \boldsymbol{E})\boldsymbol{1} \right]. \tag{3.41}$$

As mentioned previously, the volume force is in balance with the divergence of the Maxwell stress, thus

$$\boldsymbol{f}^E = \mathrm{div}\boldsymbol{\sigma}^E. \tag{3.42}$$

For the application of the divergence operator on the Maxwell stress, the following identities can be considered,

$$\text{div}(\boldsymbol{E} \otimes \boldsymbol{E}) = (\text{grad}\boldsymbol{E}) \cdot \boldsymbol{E} + \boldsymbol{E}\,\text{div}\,\boldsymbol{E}, \tag{3.43}$$

$$\text{div}\,[(\boldsymbol{E} \cdot \boldsymbol{E})\mathbf{1}] = 2(\text{grad}^T \boldsymbol{E}) \cdot \boldsymbol{E}. \tag{3.44}$$

Substituting (3.41) in (3.42) and then (3.43) and (3.44) in (3.42) results in

$$\boldsymbol{f}^E = \epsilon_0 \left[(\text{grad}\,\boldsymbol{E}) \cdot \boldsymbol{E} + \boldsymbol{E}\,\text{div}\,\boldsymbol{E} - (\text{grad}^T \boldsymbol{E}) \cdot \boldsymbol{E}\right]. \tag{3.45}$$

The electric field can be expressed as the gradient of a potential field, see (3.7). As a consequence, the gradient of the electric field is symmetric ($\text{grad}\,\boldsymbol{E} = \text{grad}^T \boldsymbol{E}$). With these considerations, (3.45) is reduced to

$$\boldsymbol{f}^E = \epsilon_0 (\text{div}\,\boldsymbol{E})\boldsymbol{E}. \tag{3.46}$$

Under the contemplation of the differential form of Gauss's law, see (3.6), the definition of the electrostatic volume force of a charged body in vacuum yields

$$\boldsymbol{f}^E = \gamma\boldsymbol{E}. \tag{3.47}$$

By comparison of (3.47) with (3.3) it becomes clear, that the electrostatic volume force is the force of an electric field on a charge density. In the example of the parallel plate capacitor in vacuum the Maxwell stress tensor is according to (3.41)

$$\boldsymbol{\sigma}^E = \begin{bmatrix} -\frac{1}{2}\epsilon_0 E^2 & 0 & 0 \\ 0 & -\frac{1}{2}\epsilon_0 E^2 & 0 \\ 0 & 0 & \frac{1}{2}\epsilon_0 E^2 \end{bmatrix}. \tag{3.48}$$

The tensor is obtained by assuming a homogeneous electric field $\boldsymbol{E} = \begin{bmatrix} 0 & 0 & E \end{bmatrix}^T$ between the plates of the capacitor. As one can see, the component σ_{33}^E which corresponds to the direction of the electric field is equal to the attraction force of the plates of the capacitor, see (3.39).

In the context of dielectric polarisable materials, the Maxwell stress is defined differently. Depending on the physical assumptions, several possibilities exist. In this work, the concept of the Kelvin polarisation force density is taken into account. Other possibilities include the Kortweg-Helmholz force density which is based on energy and work contemplations. According to the Kelvin polarisation force, see [78], the Maxwell stress

for polarisable material is defined with

$$\boldsymbol{\sigma}^E = \boldsymbol{E} \otimes \boldsymbol{D} - \frac{1}{2}\epsilon_0(\boldsymbol{E} \cdot \boldsymbol{E})\mathbf{1}. \tag{3.49}$$

The volume force is obtained by the divergence of the stress, see (3.42). To simplify the divergence, the identities (3.43) and (3.44) can be considered. The first one is modified by the introduction of $\boldsymbol{D}$ resulting in

$$\mathrm{div}\,(\boldsymbol{E} \otimes \boldsymbol{D}) = (\mathrm{grad}\,\boldsymbol{E}) \cdot \boldsymbol{D} + \boldsymbol{E}\,\mathrm{div}\,\boldsymbol{D}. \tag{3.50}$$

Computing the divergence of the Maxwell stress under this considerations, the force per unit volume turns out to be

$$\boldsymbol{f}^E = (\mathrm{grad}\,\boldsymbol{E}) \cdot \boldsymbol{D} + \boldsymbol{E}\,\mathrm{div}\,\boldsymbol{D} - \epsilon_0(\mathrm{grad}^T\,\boldsymbol{E}) \cdot \boldsymbol{E}. \tag{3.51}$$

The second term on the right hand side can be modified by considering (3.23). Furthermore, the definition of the electric displacement, see (3.22), can be introduced in (3.51), thus

$$\boldsymbol{f}^E = (\mathrm{grad}\,\boldsymbol{E}) \cdot (\epsilon_0\boldsymbol{E} + \boldsymbol{P}) + \gamma_f\boldsymbol{E} - \epsilon_0(\mathrm{grad}^T\,\boldsymbol{E}) \cdot \boldsymbol{E}. \tag{3.52}$$

The right hand side of the equation can be expanded,

$$\boldsymbol{f}^E = \epsilon_0(\mathrm{grad}\,\boldsymbol{E})\boldsymbol{E} + \mathrm{grad}\,\boldsymbol{E} \cdot \boldsymbol{P} + \gamma_f\boldsymbol{E} - \epsilon_0(\mathrm{grad}^T\,\boldsymbol{E}) \cdot \boldsymbol{E}. \tag{3.53}$$

Since the gradient of the electric field is symmetric due to the existence of the electric potential φ, the first and the third term on the right hand side cancel out. This means that the electrostatic volume force in a dielectric material is

$$\boldsymbol{f}^E = (\mathrm{grad}\,\boldsymbol{E})\boldsymbol{P} + \gamma_f\boldsymbol{E}. \tag{3.54}$$

The first term on the right hand side is in agreement with (3.17), where the electrostatic volume force is physically interpreted as the force of an inhomogeneous electric field on a dipole density. The second term corresponds to the force on a free charge density as previously shown in (3.47). It should be mentioned that the Kelvin force only considers the forces of the macroscopic electric field on the dipoles. As the material is polarised, microscopic electric fields are formed additionally to the external electric field. The interaction of these microscopic fields with neighboring dipoles is neglected in the concept of the Kelvin force density presented here, see [78] for details.

Chapter 4

Numerical Implementation

The focus of the present chapter lies on the numerical implementation of the electrome-chanical coupled field problem for DEAs. It is performed in a standard manner known for the finite element method in which the weak forms of the balance equations are discretised with finite elements by means of the isoparametric concept. This chapter aims at obtaining the tangent matrix for different formulations. This matrix serves in the solution of the nonlinear FE problem which is performed with the Newton-Raphson method, introduced in section 4.1. After the introduction the implementation details for the quasi-static case are outlined in section 4.2 which is then extended to dynamic simulations in section 4.3.

4.1   The Newton-Raphson Method

The nonlinear FEM is characterised by the fact that a nonlinear system of equations has to be solved to obtain the solution vector $\boldsymbol{u}$. Usually the system is formed by an internal residual vector $\boldsymbol{R}(\boldsymbol{u})$ and a loading vector $\boldsymbol{P}$ which is constant for the case of dead loads. In general $\boldsymbol{P}$ is scaled by a parameter λ to obtain convergence of the method. Thus the nonlinear system of equations has the form

$$\boldsymbol{G}(\boldsymbol{u}, \lambda) = \boldsymbol{R}(\boldsymbol{u}) - \lambda \boldsymbol{P} = \boldsymbol{0}. \tag{4.1}$$

To solve (4.1) in a numerical procedure a Taylor expansion is performed which is obtained as

$$\boldsymbol{G}(\boldsymbol{u}^{(k+1)}, \overline{\lambda}) = \boldsymbol{G}(\boldsymbol{u}^{(k)}, \overline{\lambda}) + D\boldsymbol{G}(\boldsymbol{u}^{(k)}, \overline{\lambda})\Delta\boldsymbol{u} + \mathcal{O}(\Delta\boldsymbol{u}^2). \tag{4.2}$$

In this equation, the second term on the right hand side is known as the directional derivative or linearisation of $\boldsymbol{G}$ at the point $\boldsymbol{u}^{(k)}$. It provides the matrix $\boldsymbol{K}$ known as

31

the tangent matrix. Neglecting the higher order terms in (4.2) and with the condition

$$G(u^{(k+1)}, \overline{\lambda}) = 0, \tag{4.3}$$

the linear system

$$K \, \Delta u^{(k)} = -G^{(k)} \tag{4.4}$$

has to be solved to obtain $\Delta u^{(k)}$. Thus, the algorithm of the Newton-Raphson method can be formulated as follows.

1: Initialise solution $u^{(k)} = u^{(0)}$

2: Compute $G(u^{(k)}, \overline{\lambda})$ and $K(u^{(k)})$

3: Solve $K \, \Delta u^{(k)} = -G^{(k)}$

4: Compute $u^{(k+1)} = u^{(k)} + \Delta u^{(k)}$

5: Test convergence $||G(u^{(k+1)}, \overline{\lambda})||$ $\begin{cases} < TOL \rightarrow \text{STOP} \\ > TOL \rightarrow k = k+1, \text{GOTO Step 2} \end{cases}$

For the 1D case the algorithm can be represented schematically as shown in Fig. 4.1. Here the nonlinear equation $G(u, \lambda)$, see (4.1), has been normalised. Thus $\hat{R}(u) - \overline{\lambda} = 0$ has to be solved obtaining the solution u^*.
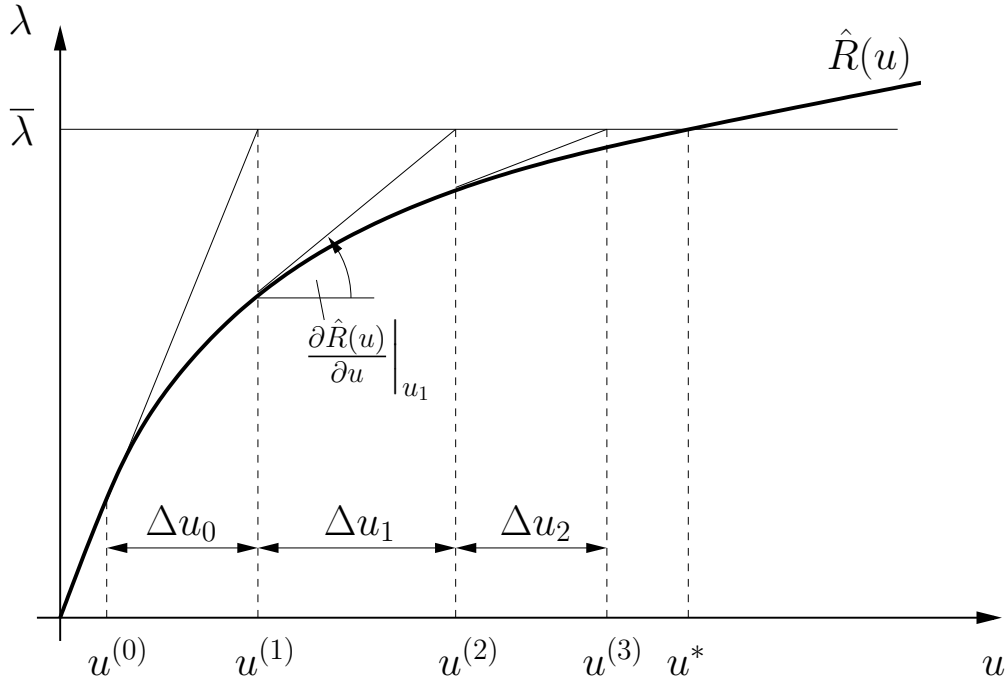

FIGURE 4.1: Representation of the Newton-Raphson method for the 1D case.

The main advantage of the method is the quadratic convergence of the scheme in the vicinity of the solution leading to a reduced number of iterations. As a disadvantage it

should be mentioned that the computation of $\boldsymbol{K}$ and the solution of (4.4) are in general time consuming.

4.2 Quasi-Static Implementation

In this section the required concepts for the implementation of the coupled field problem for the quasi-static case are outlined. In order to gradually increase the complexity the concepts of the displacement formulation case are presented at first. With this, the implementation for the simulation for a DEA is executable but it is restricted to compressible materials. As a next step the displacement formulation is replaced by the three field formulation to treat the incompressibility constraint which is typical for DEs. By this means the necessary ingredients are introduced which allow the understanding of the advanced elements for quasi-incompressibility. The procedure is to start with the mechanical case and then adapt it to the coupled field problem.

4.2.1 Displacement Formulation

So far, the fundamental equations and derivations of the mechanical and electrostatic phenomena have been contemplated separately in the previous chapters 2 and 3.

The balance of linear momentum of a material point in continuum mater has been introduced in (2.16). Furthermore, mechanical loads are omitted since the focus of the present work is on the electromechanical coupling of electric fields with mechanical deformations. For this reason body forces $\boldsymbol{b}$ are neglected. The only considered load in the framework is the electrostatic volume load $\boldsymbol{f}^E$ which is introduced in (3.17) as the force of an electric field on polarisable material. Hence, the linear momentum balance of the electromechanical coupled field problem can be written down in the current configuration with

$$\mathrm{div}\boldsymbol{\sigma} + \boldsymbol{f}^E = \boldsymbol{0}. \tag{4.5}$$

In section 3.4 the electrostatic volume force is related to the Maxwell stress via the divergence operator, see (3.42). With this, the previous expression (4.5) is rewritten to yield

$$\mathrm{div}\left(\boldsymbol{\sigma} + \boldsymbol{\sigma}^E\right) = \mathrm{div}\,\boldsymbol{\tau} = \boldsymbol{0}. \tag{4.6}$$

Under this perspective, the electromechanical coupling can be described as a balance of a total stress $\boldsymbol{\tau}$ which is composed additively by the Cauchy stress $\boldsymbol{\sigma}$ and the Maxwell stress $\boldsymbol{\sigma}^E$. The nature of the stresses are mechanical and electric, respectively.

In the present work the algorithmic implementation is performed in the reference configuration. Thus, the weak form of the linear momentum balance (4.6) needs to be formulated in this configuration. This is realised by the pull-back of $\boldsymbol{\tau}$ into the reference configuration and transforming it into a symmetric total second Piola-Kirchhoff stress

$$\boldsymbol{T}_0 = \boldsymbol{S}_0 + \boldsymbol{S}_0^E. \tag{4.7}$$

The details of the pull-back are not outlined here but can be found in [79]. The mechanical second Piola-Kirchhoff stress $\boldsymbol{S}_0$ depends on the mechanical constitutive relation which is introduced in (2.35). Different alternatives are proposed in sections 2.3.1.1, 2.3.1.2 and 2.3.1.3. The Maxwell stress is pulled back in the reference configuration according to

$$\boldsymbol{S}_0^E = \left(\boldsymbol{C}^{-1}\boldsymbol{E}_0\right) \otimes \boldsymbol{D}_0 - \frac{1}{2}\epsilon_0 J \left[\boldsymbol{E}_0 \cdot \left(\boldsymbol{C}^{-1}\boldsymbol{E}_0\right)\right] \boldsymbol{C}^{-1}, \tag{4.8}$$

in which $\boldsymbol{C}$ is the right Cauchy-Green tensor introduced in (2.6) and J is the determinant of the deformation gradient, see (2.3). The electric field (3.7) is defined for the current configuration and can be pulled back by use of its definition and the chain rule according to

$$\boldsymbol{E}_0 = -\text{Grad}\,\varphi = \boldsymbol{F}^T \boldsymbol{E}. \tag{4.9}$$

It can be regarded as the electric counterpart of a mechanical strain measure which is defined as the gradient of the displacement field. In a similar way, the electric displacement introduced in (3.25) can be seen as the electric counterpart of the Cauchy stress. With Nanson's formula, see (2.5), the pulled back version of the electric displacement is obtained,

$$\boldsymbol{D}_0 = J\boldsymbol{F}^{-1}\boldsymbol{D}. \tag{4.10}$$

The same idea is also applicable for the polarisation vector,

$$\boldsymbol{P}_0 = J\boldsymbol{F}^{-1}\boldsymbol{P}. \tag{4.11}$$

In (3.24) the linear relationship between the polarisation and the electric field, which can be regarded as the electric constitutive law for polarisable matter, has been introduced. This law can also be derived from an electric energy per unit volume h according to [79] with

$$\boldsymbol{P} = -\rho\frac{\partial h}{\partial \boldsymbol{E}}. \tag{4.12}$$

The electric energy h can also be formulated in the reference configuration by the density change with

$$h_0 = \rho J h \tag{4.13}$$

Assuming that the electric energy in the reference configuration is

$$h_0 = \frac{1}{2}\epsilon_0\chi \boldsymbol{E} \cdot \boldsymbol{E}, \tag{4.14}$$

the electric constitutive law for polarisable matter can be obtained with (4.12), (4.13) and (4.14). Thus

$$\boldsymbol{P} = \frac{\epsilon_0\chi}{J}\boldsymbol{E}. \tag{4.15}$$

In comparison to (3.24) the polarisation now also depends on the change of the material density. Substituting (4.15) in (3.22) delivers the electric displacement which now is also dependent on the material density change,

$$\boldsymbol{D} = \epsilon_0\left(1 + \frac{\chi}{J}\right)\boldsymbol{E}. \tag{4.16}$$

With the definition of the stresses in the reference configuration, the necessary steps to obtain the formulation of the weak form can be performed. Neglecting additional external volume forces, the weak form of the mechanical balance is established by

$$W_{mech} = \int_{\mathcal{B}_0} (\boldsymbol{S}_0 + \boldsymbol{S}_0^E) : \delta\boldsymbol{G}\,\mathrm{d}V = \int_{\mathcal{B}_0} \boldsymbol{T}_0 : \delta\boldsymbol{G}\,\mathrm{d}V = 0, \tag{4.17}$$

where $\delta\boldsymbol{G}$ is a virtual Green-Lagrange strain tensor.

The second balance law for the electromechanical coupled field problem in the current configuration is established by Gauss's law for dielectric materials described in (3.23). With the assumption that the charges in a dielectric are all bound ($\gamma_f = 0$), the law of Gauss is defined in the reference configuration by

$$\mathrm{Div}\,\boldsymbol{D}_0 = 0. \tag{4.18}$$

Neglecting surface charges, the local balance of the electric displacement is transformed to the weak form

$$W_{elec} = \int_{\mathcal{B}_0} \boldsymbol{D}_0 \cdot \delta\boldsymbol{E}_0\,\mathrm{d}V = 0, \tag{4.19}$$

where $\delta\boldsymbol{E}_0$ is a virtual electric field.

At this point the weak formulations represented in (4.17) and (4.19) can be discretized for the numerical implementation. The method used here is the standard discretization technique with shape functions known from the FE method by means of the isoparametric concept. In the electromechanical coupled field problem both, the displacement $\boldsymbol{u}$ and the electric potential φ, are discretized with the shape functions N_I. On the element

level the discretization is

$$\underline{\boldsymbol{u}} = \sum_{I=1}^{N} N_I \underline{\boldsymbol{u}}_I, \quad \varphi = \sum_{I=1}^{N} N_I \varphi_I. \tag{4.20}$$

The underbar in the previous and subsequent equations denotes the matrix notation. It is used to express discretised quantities and equations. The same concept is also applied to the virtual displacements and the virtual electric potential,

$$\underline{\delta \boldsymbol{u}} = \sum_{I=1}^{N} N_I \underline{\delta \boldsymbol{u}}_I, \quad \delta \varphi = \sum_{I=1}^{N} N_I \delta \varphi_I. \tag{4.21}$$

It should be noted that I is the index of the element node for an element with N nodes. After having established the discretisation of the field, the tensors $\delta \boldsymbol{G}$ and $\delta \boldsymbol{E}_0$ can be recast into the discrete version. First their relation to the field is mentioned. Namely,

$$\delta \boldsymbol{G} = \text{sym} \left(\boldsymbol{F}^T \text{Grad} \, \delta \boldsymbol{u} \right) = \frac{1}{2} (\boldsymbol{F}^T \delta \boldsymbol{F} + \delta \boldsymbol{F}^T \boldsymbol{F}) \quad \text{with} \quad \text{Grad} \, \delta \boldsymbol{u} = \delta \boldsymbol{F}, \tag{4.22}$$

in which $\boldsymbol{F}$ is the deformation gradient introduced in (2.2), and for the electric field

$$\delta \boldsymbol{E}_0 = -\text{Grad} \, \delta \varphi. \tag{4.23}$$

Considering (4.22), the discretisation of the virtual displacement (4.21) and the application of the gradient on the discretized field the discrete version of $\delta \boldsymbol{G}$ is obtained,

$$\underline{\delta \boldsymbol{G}} = \left[\begin{array}{cccccc} \delta G_{11} & \delta G_{22} & \delta G_{33} & 2\delta G_{12} & 2\delta G_{23} & 2\delta G_{31} \end{array} \right]^T = \sum_{I=1}^{N} \underline{\boldsymbol{B}}_I^0 \underline{\delta \boldsymbol{u}}_I. \tag{4.24}$$

The B-matrix which contains the derivatives of the shape functions is computed by

$$\underline{\boldsymbol{B}}_I^0 = \begin{bmatrix} F_{11}N_{I,1} & F_{21}N_{I,1} & F_{31}N_{I,1} \\ F_{12}N_{I,2} & F_{22}N_{I,2} & F_{32}N_{I,2} \\ F_{13}N_{I,3} & F_{23}N_{I,3} & F_{33}N_{I,3} \\ F_{11}N_{I,2} + F_{12}N_{I,1} & F_{21}N_{I,2} + F_{22}N_{I,1} & F_{31}N_{I,2} + F_{32}N_{I,1} \\ F_{12}N_{I,3} + F_{13}N_{I,2} & F_{22}N_{I,3} + F_{23}N_{I,2} & F_{32}N_{I,3} + F_{33}N_{I,2} \\ F_{11}N_{I,3} + F_{13}N_{I,1} & F_{21}N_{I,3} + F_{23}N_{I,1} & F_{31}N_{I,3} + F_{33}N_{I,1} \end{bmatrix}, \tag{4.25}$$

and the virtual displacement is represented by

$$\underline{\delta \boldsymbol{u}}_I = \left[\begin{array}{ccc} \delta u_{1I} & \delta u_{2I} & \delta u_{3I} \end{array} \right]^T. \tag{4.26}$$

Here the Voigt notation has been introduced which simplifies the representation of symmetric tensors. Thus the second order tensor $\delta \boldsymbol{G}$ can be expressed by a vector in its

discretised version $\delta \underline{G}$. The same procedure can also be applied to (4.23) with consideration of the discrete version of the virtual electric potential. This results in

$$\delta \underline{E}_0 = \left[\begin{array}{ccc} \delta E_{0_1} & \delta E_{0_2} & \delta E_{0_3} \end{array} \right]^T = -\sum_{I=1}^{N} \widetilde{\underline{B}}_I^0 \delta \varphi_I. \tag{4.27}$$

In this case the B-matrix differs from the previous one. Here, only the derivatives of the shape functions in the coordinate directions are necessary,

$$\widetilde{\underline{B}}_I^0 = \left[\begin{array}{ccc} N_{I,1} & N_{I,2} & N_{I,3} \end{array} \right]^T. \tag{4.28}$$

Additionally, the total stress $\boldsymbol{T}_0$ and the electric displacement $\boldsymbol{D}_0$ are written in matrix notation. Finally the internal residual vector for the mechanical and the electric part can be formulated for each node of the element via

$$\underline{\boldsymbol{R}}_I^m(\underline{\boldsymbol{u}}_I, \varphi_I) = -\int_{\mathcal{B}_0^e} \underline{\boldsymbol{B}}_I^{0^T} \underline{\boldsymbol{T}}_0 \, \mathrm{d}V \tag{4.29}$$

with

$$\underline{\boldsymbol{T}}_0 = \left[\begin{array}{cccccc} T_{0_{11}} & T_{0_{22}} & T_{0_{33}} & T_{0_{12}} & T_{0_{23}} & T_{0_{13}} \end{array} \right]^T \tag{4.30}$$

and

$$R_I^e(\underline{\boldsymbol{u}}_I, \varphi_I) = -\int_{\mathcal{B}_0^e} \widetilde{\underline{\boldsymbol{B}}}_I^{0^T} \underline{\boldsymbol{D}}_0 \, \mathrm{d}V \tag{4.31}$$

with

$$\underline{\boldsymbol{D}}_0 = \left[\begin{array}{ccc} D_{0_1} & D_{0_2} & D_{0_3} \end{array} \right]^T. \tag{4.32}$$

Because of the nonlinear nature of the coupled field problem considered here (large deformations and nonlinear constitutive relations), it is solved iteratively in the framework of the Newton-Raphson method. In each iteration step, the tangent of the residual function is needed. One possibility would be the computation of a numerical tangent by a considerably small perturbation in the residual function. The other possibility is the deduction of the consistent tangent in an analytical form which usually leads to a higher convergence rate than the numerical tangent. In a coupled field problem a monolithic tangent matrix is obtained by the derivation of the residuals w.r.t. the fields considered in the problem. In the case of the electromechanical coupling, the residuals (4.29) and (4.31) are derived w.r.t. $\underline{\boldsymbol{u}}_J$ and φ_J to yield the matrix

$$\underline{\boldsymbol{K}}_{IJ} = \left[\begin{array}{cc} \underline{\boldsymbol{K}}_{IJ}^{mm} & \underline{\boldsymbol{K}}_{IJ}^{me} \\ \underline{\boldsymbol{K}}_{IJ}^{em} & K_{IJ}^{ee} \end{array} \right], \tag{4.33}$$

with

$$\boldsymbol{K}_{IJ}^{mm} = -\frac{\partial \boldsymbol{R}_I^m}{\partial \underline{\boldsymbol{u}}_J}, \quad \boldsymbol{K}_{IJ}^{me} = -\frac{\partial \boldsymbol{R}_I^m}{\partial \varphi_J}, \quad \boldsymbol{K}_{IJ}^{em} = -\frac{\partial R_I^e}{\partial \underline{\boldsymbol{u}}_J}, \quad K_{IJ}^{ee} = -\frac{\partial R_I^e}{\partial \varphi_J}. \tag{4.34}$$

The full tangent matrix $\underline{\boldsymbol{K}}$ for the element is assembled using the matrices $\underline{\boldsymbol{K}}_{IJ}$ according to the arrangement of the solution vector in the considered FE solver. The indices I and J address the nodes of the element.

In the next pages the submatrices presented in (4.34) will be derived in detail to present the constitution of the consistent tangent.

4.2.1.1   Submatrix K^{mm}

In the first submatrix $\underline{\boldsymbol{K}}_{IJ}^{mm}$ the mechanical residual is derived w.r.t. the displacement. With the application of the product rule, it can be written as

$$\boldsymbol{K}_{IJ}^{mm} = -\frac{\partial \boldsymbol{R}_I^m}{\partial \underline{\boldsymbol{u}}_J} = \frac{\partial}{\partial \underline{\boldsymbol{u}}_J} \int_{\mathcal{B}_0^e} \boldsymbol{B}_I^{0T} \boldsymbol{T}_0 \, \mathrm{d}V = \int_{\mathcal{B}_0^e} \frac{\partial \boldsymbol{B}_I^{0T}}{\partial \underline{\boldsymbol{u}}_J} \boldsymbol{T}_0 \, \mathrm{d}V + \int_{\mathcal{B}_0^e} \boldsymbol{B}_I^{0T} \frac{\partial \boldsymbol{T}_0}{\partial \underline{\boldsymbol{u}}_J} \, \mathrm{d}V. \tag{4.35}$$

Here, the first term is known as the geometric tangent which is required for problems with large deformations,

$$\int_{\mathcal{B}_0^e} \frac{\partial \boldsymbol{B}_I^{0T}}{\partial \underline{\boldsymbol{u}}_J} \boldsymbol{T}_0 \, \mathrm{d}V = \int_{\mathcal{B}_0^e} G_{IJ} \mathbb{I} \, \mathrm{d}V, \tag{4.36}$$

in which

$$G_{IJ} = \begin{bmatrix} N_{I,1} & N_{I,2} & N_{I,3} \end{bmatrix} \begin{bmatrix} T_{0_{11}} & T_{0_{12}} & T_{0_{13}} \\ T_{0_{21}} & T_{0_{22}} & T_{0_{23}} \\ T_{0_{31}} & T_{0_{32}} & T_{0_{33}} \end{bmatrix} \begin{bmatrix} N_{J,1} \\ N_{J,2} \\ N_{J,3} \end{bmatrix}. \tag{4.37}$$

The matrix $\mathbb{I}$ is the fourth order identity tensor in matrix notation. Thus it reduces to the usual identity matrix. In the second term of (4.35) the total stress is derived w.r.t. the displacement. This part of the tangent depends on the constitutive law of the material. To obtain the derivatives of the stress tensors w.r.t. the right Cauchy-Green tensor as defined in chapter 2, the chain rule is applied leading to the expression

$$\int_{\mathcal{B}_0^e} \boldsymbol{B}_I^{0T} \frac{\partial \boldsymbol{T}_0}{\partial \underline{\boldsymbol{u}}_J} \, \mathrm{d}V = 2 \int_{\mathcal{B}_0^e} \boldsymbol{B}_I^{0T} \frac{\partial \boldsymbol{T}_0}{\partial \underline{\boldsymbol{C}}} \boldsymbol{B}_J^0 \, \mathrm{d}V = 2 \int_{\mathcal{B}_0^e} \boldsymbol{B}_I^{0T} \left(\frac{\partial \boldsymbol{S}_0}{\partial \underline{\boldsymbol{C}}} + \frac{\partial \boldsymbol{S}_0^E}{\partial \underline{\boldsymbol{C}}} \right) \boldsymbol{B}_J^0 \, \mathrm{d}V. \tag{4.38}$$

The second B-matrix originates from the discretization of $\boldsymbol{G}$,

$$\underline{\boldsymbol{G}} = \sum_{J=1}^N \boldsymbol{B}_J^0 \underline{\boldsymbol{u}}_J \quad \rightarrow \quad \frac{\partial \underline{\boldsymbol{G}}}{\partial \underline{\boldsymbol{u}}_J} = \boldsymbol{B}_J^0. \tag{4.39}$$

Finally, the complete submatrix can be written as

$$\underline{\boldsymbol{K}}_{IJ}^{mm} = 2 \int_{\mathcal{B}_0^e} \underline{\boldsymbol{B}}_I^{0T} \left(\frac{\partial \underline{\boldsymbol{S}}_0}{\partial \underline{\boldsymbol{C}}} + \frac{\partial \underline{\boldsymbol{S}}_0^E}{\partial \underline{\boldsymbol{C}}} \right) \underline{\boldsymbol{B}}_J^0 \, \mathrm{d}V + \int_{\mathcal{B}_0^e} G_{IJ} \mathbb{I} \, \mathrm{d}V. \tag{4.40}$$

As mentioned previously, the first term of the matrix depends on the chosen mechanical constitutive law and the derivative of the Maxwell stress w.r.t. the Green-Lagrange strain. Depending on the selected mechanical material model, the derivatives found in 2.3.1 and 2.3.2 can be substituted into (4.40). The details of the second derivative are outlined in the appendix A.1.

4.2.1.2 Submatrix K^{me}

In the second submatrix $\underline{\boldsymbol{K}}_{IJ}^{me}$ the mechanical residual is derived w.r.t. the electric potential,

$$\underline{\boldsymbol{K}}_{IJ}^{me} = -\frac{\partial \underline{\boldsymbol{R}}_I^m}{\partial \varphi_J} = \frac{\partial}{\partial \varphi_J} \int_{\mathcal{B}_0^e} \underline{\boldsymbol{B}}_I^{0T} (\underline{\boldsymbol{S}}_0 + \underline{\boldsymbol{S}}_0^E) \, \mathrm{d}V. \tag{4.41}$$

In this case, only the Maxwell stress depends on the electric potential. The derivative w.r.t. the electric field can be reformulated by application of the chain rule according to

$$\frac{\partial \underline{\boldsymbol{S}}_0^E}{\partial \varphi_J} = \frac{\partial \underline{\boldsymbol{S}}_0^E}{\partial \underline{\boldsymbol{E}}_0} \frac{\partial \underline{\boldsymbol{E}}_0}{\partial \varphi_J}. \tag{4.42}$$

Considering the discretization of the electric field, the second factor on the right hand side of (4.42) turns out to be

$$\underline{\boldsymbol{E}}_0 = -\sum_{J=1}^{N} \widetilde{\underline{\boldsymbol{B}}}_J^0 \varphi_J \quad \rightarrow \quad \frac{\partial \underline{\boldsymbol{E}}_0}{\partial \varphi_J} = -\widetilde{\underline{\boldsymbol{B}}}_J^0. \tag{4.43}$$

After substituting (4.43) and (4.42) in (4.41) the first coupling part of the tangent matrix is obtained,

$$\underline{\boldsymbol{K}}_{IJ}^{me} = -\int_{\mathcal{B}_0^e} \underline{\boldsymbol{B}}_I^{0T} \frac{\partial \underline{\boldsymbol{S}}_0^E}{\partial \underline{\boldsymbol{E}}_0} \widetilde{\underline{\boldsymbol{B}}}_J^0 \, \mathrm{d}V. \tag{4.44}$$

The derivative of the Maxwell stress w.r.t. the electric field is outlined in the appendix A.2.

4.2.1.3 Submatrix K^{em}

The second coupling part of the tangent matrix $\underline{\boldsymbol{K}}_{IJ}^{em}$ is obtained by differentiation of the electric residual w.r.t. the displacement,

$$\underline{\boldsymbol{K}}_{IJ}^{em} = -\frac{\partial R_I^e}{\partial \underline{\boldsymbol{u}}_J} = \frac{\partial}{\partial \underline{\boldsymbol{u}}_J} \int_{\mathcal{B}_0^e} \widetilde{\underline{\boldsymbol{B}}}_I^{0T} \underline{\boldsymbol{D}}_0 \, \mathrm{d}V. \tag{4.45}$$

Since the B-matrix corresponding to the discretization of the electric field is independent of the displacement, only the derivative of the electric displacement w.r.t. the displacement has to be considered. With the application of the chain rule and (4.39) the derivative turns out to be

$$\frac{\partial \underline{\boldsymbol{D}}_0}{\partial \underline{\boldsymbol{u}}_J} = 2 \frac{\partial \underline{\boldsymbol{D}}_0}{\partial \underline{\boldsymbol{C}}} \boldsymbol{B}_J^0. \tag{4.46}$$

Substituting 4.46 in 4.45 the submatrix can be written down as

$$\underline{\boldsymbol{K}}_{IJ}^{em} = 2 \int_{\mathcal{B}_0^e} \widetilde{\underline{\boldsymbol{B}}}_I^{0T} \frac{\partial \underline{\boldsymbol{D}}_0}{\partial \underline{\boldsymbol{C}}} \boldsymbol{B}_J^0 \, \mathrm{d}V. \tag{4.47}$$

The derivative of the electric displacement w.r.t. the right Cauchy-Green tensor can be found in the appendix A.3.

4.2.1.4   Submatrix K^{ee}

The last submatrix $\boldsymbol{K}_{IJ}^{ee}$ is the pure electric part of the tangent which consists of the derivation of the electric residual w.r.t. the electric potential,

$$\boldsymbol{K}_{IJ}^{ee} = -\frac{\partial R_I^e}{\partial \varphi_J} = \frac{\partial}{\partial \varphi_J} \int_{\mathcal{B}_0^e} \widetilde{\underline{\boldsymbol{B}}}_I^{0T} \underline{\boldsymbol{D}}_0 \, \mathrm{d}V. \tag{4.48}$$

The B-matrix in this equation is independent of the electric potential. The only derivative which has to be considered is the derivative of the electric displacement w.r.t. the electric potential. As in the previous cases, the chain rule is applied and (4.43) is considered,

$$\frac{\partial \underline{\boldsymbol{D}}_0}{\partial \varphi_J} = \frac{\partial \underline{\boldsymbol{D}}_0}{\partial \underline{\boldsymbol{E}}_0} \frac{\partial \underline{\boldsymbol{E}}_0}{\partial \varphi_J} = -\frac{\partial \underline{\boldsymbol{D}}_0}{\partial \underline{\boldsymbol{E}}_0} \widetilde{\underline{\boldsymbol{B}}}_J^0. \tag{4.49}$$

Thus, the last submatrix of the consistent tangent is

$$\boldsymbol{K}_{IJ}^{ee} = -\int_{\mathcal{B}_0^e} \widetilde{\underline{\boldsymbol{B}}}_I^{0T} \frac{\partial \underline{\boldsymbol{D}}_0}{\partial \underline{\boldsymbol{E}}_0} \widetilde{\underline{\boldsymbol{B}}}_J^0 \, \mathrm{d}V. \tag{4.50}$$

The derivative of the electric displacement w.r.t. the electric field is outlined in the appendix A.4.

With the presented derivatives, all parts of the consistent tangent matrix and the residual vector are available. In the situation of a 3D implementation, the displacement $\underline{\boldsymbol{u}}$ is given by 3 components in each node. The electric potential φ represents one additional degree of freedom. Thus, the part of the tangent matrix, solution vector, and internal residual

which correspond to a node are

$$
\underline{\boldsymbol{K}}_{IJ} = \begin{bmatrix} \left[\boldsymbol{K}_{IJ}^{mm}\right]_{3\times3} & \left[\boldsymbol{K}_{IJ}^{me}\right]_{3\times1} \\ \left[\boldsymbol{K}_{IJ}^{em}\right]_{1\times3} & K_{IJ}^{ee} \end{bmatrix}_{4\times4} , \quad \underline{\Delta\boldsymbol{u}}_I = \begin{bmatrix} \Delta u_{1I} \\ \Delta u_{2I} \\ \Delta u_{3I} \\ \Delta\varphi_I \end{bmatrix}_{4\times1} ,
$$

$$
\underline{\boldsymbol{R}}_I = \begin{bmatrix} \left[\underline{\boldsymbol{R}}_I^{m}\right]_{3\times1} \\ R_I^e \end{bmatrix}_{4\times1} . \tag{4.51}
$$

The consideration of a 3D brick element with 8 nodes and linear shape functions would deliver the the following system of equations which corresponds to the element,

$$
\begin{bmatrix} \underline{\boldsymbol{K}}_{11} & \cdots & \underline{\boldsymbol{K}}_{18} \\ \vdots & \ddots & \vdots \\ \underline{\boldsymbol{K}}_{81} & \cdots & \underline{\boldsymbol{K}}_{88} \end{bmatrix}_{32\times32} \begin{bmatrix} \underline{\Delta\boldsymbol{u}}_1 \\ \vdots \\ \underline{\Delta\boldsymbol{u}}_8 \end{bmatrix}_{32\times1} = \begin{bmatrix} \underline{\boldsymbol{R}}_1 \\ \vdots \\ \underline{\boldsymbol{R}}_8 \end{bmatrix}_{32\times1} . \tag{4.52}
$$

The global system of equations is then assembled according to the connectivity of the elements and solved in each Newton-Raphson iteration until the global residual reaches the convergence criterium.

As a last and important remark it should be mentioned that the tangent matrix $\underline{\boldsymbol{K}}_{IJ}$ is symmetric. This means that the electromechanical balance equations can be derived from a potential functional. However, when comparing (4.44) and (4.47) the equality can not bee seen directly. It becomes obvious that if

$$
\frac{\partial \underline{\boldsymbol{S}}_0^E}{\partial \underline{\boldsymbol{E}}_0} = -2 \frac{\partial \underline{\boldsymbol{D}}_0}{\partial \underline{\boldsymbol{C}}}^T , \tag{4.53}
$$

the tangent matrix will be symmetric since

$$
\underline{\boldsymbol{K}}_{IJ}^{me} = \underline{\boldsymbol{K}}_{IJ}^{emT} . \tag{4.54}
$$

The proof that condition (4.53) is true is shown in appendix A.5.

4.2.2 Three Field Formulation

In section 2.2.1 an alternative to the standard displacement formulation has been introduced because dielectric elastomers are nearly incompressible materials and thus, volumetric locking effects can appear. As mentioned, the incorporation of additional field variables in the free energy under the consideration of constraints offers an alternative

which deals with quasi-incompressibility in a more elegant way. Therefore the numerical outline for the implementation of the three field formulation in the finite element method is presented. To this end so called mixed elements are formulated, which take into account the additional field variables introduced in the free energy formulation. In this work two discretization schemes are used, namely the Q1P0 and the Q2P1 element. Details about the numerical efficiency of theese elements can be reviewed in [80]. Additional literature about quasi-incompressible elements and the study of volumetric locking can be found e. g. in [81–86].

The implementation is as follows: The linearisations of the weak forms introduced in section 2.2.1 are presented. Afterwards the linearisations and the weak forms are discretised delivering the consistent tangent matrix and internal residual vector for the mechanical part. Subsequently the Q1P0 and the Q2P1 elements are discussed with the application to the electromechanical coupled field situation.

It should be noted, that the implementation procedure differs from the one presented in section 4.2.1 since the discretisation is performed on the weak form and the corresponding linearisations. In section 4.2.1 the weak form is discretised and the internal load vector is obtained. Afterwards it is derived w.r.t. the discrete degrees of freedom to obtain the tangent matrix. For the electromechanical coupled field problem study in this work the consideration of both implementation procedures leads to the same tangent matrix. For this reason both options are taken into account.

The weak forms which state the equilibrium in the three field formulation are introduced in the equations (2.31) to (2.33). To obtain the tangent matrix for the iterative Newton-Raphson scheme, the linearisation of the weak forms w.r.t. the three field variables $\boldsymbol{u}$, p and θ is required. The linearisation is performed with the concept of the Gateaux-derivative. If a function $f(\boldsymbol{x})$ is linearised at the point $\overline{\boldsymbol{x}}$, it can be written according to

$$f(\overline{\boldsymbol{x}} + \Delta\boldsymbol{u}) \approx f(\overline{\boldsymbol{x}}) + \mathrm{D}_{\Delta\boldsymbol{u}}. \tag{4.55}$$

The second term on the right hand side is known as the Gateaux-derivative and is defined as

$$\mathrm{D}_{\Delta\boldsymbol{u}} = \frac{\mathrm{d}}{\mathrm{d}\varepsilon} f(\overline{\boldsymbol{x}} + \varepsilon\Delta\boldsymbol{u})|_{\varepsilon=0} = \left.\frac{\partial f}{\partial\boldsymbol{x}}\right|_{\overline{\boldsymbol{x}}} \cdot \Delta\boldsymbol{u}. \tag{4.56}$$

Considering this, the weak forms (2.31) - (2.33) are linearised w.r.t. the field variables under the assumption of external dead loads. The nontrivial linearisations are:

$$D_{\Delta \boldsymbol{u}} \delta W_{\boldsymbol{u}} = \int_{\mathcal{B}_0} \mathrm{Grad} \Delta \boldsymbol{u} (\boldsymbol{S}_0^{vol} + \boldsymbol{S}_0^{iso}) : \mathrm{Grad} \delta \boldsymbol{u} \, \mathrm{d}V$$

$$+ 2 \int_{\mathcal{B}_0} \delta \boldsymbol{G} : \left(\frac{\partial \boldsymbol{S}_0^{vol}}{\partial \boldsymbol{C}} + \frac{\partial \boldsymbol{S}_0^{iso}}{\partial \boldsymbol{C}} \right) \Delta \boldsymbol{G} \, \mathrm{d}V, \tag{4.57}$$

$$D_{\Delta p} \delta W_{\boldsymbol{u}} = \int_{\mathcal{B}_0} J \Delta p \, \boldsymbol{C}^{-1} : \delta \boldsymbol{G} \, \mathrm{d}V, \tag{4.58}$$

$$D_{\Delta \boldsymbol{u}} \delta W_p = \int_{\mathcal{B}_0} J \boldsymbol{C}^{-1} : \Delta \boldsymbol{G} \, \delta p \, \mathrm{d}V, \tag{4.59}$$

$$D_{\Delta \theta} \delta W_p = - \int_{\mathcal{B}_0} \Delta \theta \, \delta p \, \mathrm{d}V, \tag{4.60}$$

$$D_{\Delta p} \delta W_\theta = - \int_{\mathcal{B}_0} \Delta p \, \delta \theta \, \mathrm{d}V, \tag{4.61}$$

$$D_{\Delta \theta} \delta W_\theta = \int_{\mathcal{B}_0} \frac{\partial^2 \Psi_{vol}}{\partial \theta^2} \Delta \theta \, \delta \theta \, \mathrm{d}V. \tag{4.62}$$

Now the weak forms (2.31) - (2.33) and the linearisations (4.57) - (4.62) can be discretized. Therefore, the isoparametric concept is considered where the three fields are approximated by shape functions. The virtual fields are approximated by

$$\underline{\delta \boldsymbol{u}} = \sum_{I=1}^N N_I \underline{\delta \boldsymbol{u}_I}, \quad \underline{\delta \boldsymbol{G}} = \sum_{I=1}^N \boldsymbol{B}_I^0 \underline{\delta \boldsymbol{u}_I}, \quad \delta p = \sum_{I=1}^N N_I^p \delta p_I, \quad \delta \theta = \sum_{I=1}^N N_I^\theta \delta \theta_I. \tag{4.63}$$

The solution fields are discretized in the same manner. Thus,

$$\underline{\Delta \boldsymbol{u}} = \sum_{J=1}^N N_J \underline{\Delta \boldsymbol{u}_J}, \quad \underline{\Delta \boldsymbol{G}} = \sum_{J=1}^N \boldsymbol{B}_J^0 \underline{\Delta \boldsymbol{u}_J},$$

$$\Delta p = \sum_{J=1}^N N_J^p \Delta p_J, \quad \Delta \theta = \sum_{J=1}^N N_J^\theta \Delta \theta_J. \tag{4.64}$$

With the transformation of the second Piola-Kirchhoff stresses into the matrix notation and the application of (4.63) on the weak forms (2.31) - (2.33), the internal residual vectors are obtained,

$$\underline{\boldsymbol{R}}_I^{\boldsymbol{u}}(\boldsymbol{u}_I, p_I, \theta_I) = - \int_{\mathcal{B}_0^e} \boldsymbol{B}_I^{0^T} (\underline{\boldsymbol{S}}_0^{iso} + \underline{\boldsymbol{S}}_0^{vol}) \, \mathrm{d}V, \tag{4.65}$$

$$R_I^p(\boldsymbol{u}_I, p_I, \theta_I) = - \int_{\mathcal{B}_0^e} (J - \theta) N_I^p \, \mathrm{d}V, \tag{4.66}$$

$$R_I^\theta(\boldsymbol{u}_I, p_I, \theta_I) = - \int_{\mathcal{B}_0^e} \left(\frac{\partial \Psi_{vol}}{\partial \theta} - p \right) N_I^\theta \, \mathrm{d}V. \tag{4.67}$$

Considering now the discretisations in (4.63) and (4.64) and applying them on the linearisations (4.57) - (4.62) with the appropriate transformations, the components of the tangent matrix are obtained,

$$\underline{\boldsymbol{K}}^{\boldsymbol{uu}}_{IJ} = 2 \int_{\mathcal{B}^e_0} \underline{\boldsymbol{B}}^{0T}_I \left(\frac{\partial \underline{\boldsymbol{S}}^{vol}_0}{\partial \underline{\boldsymbol{C}}} + \frac{\partial \underline{\boldsymbol{S}}^{iso}_0}{\partial \underline{\boldsymbol{C}}} \right) \underline{\boldsymbol{B}}^0_J \, \mathrm{d}V + \int_{\mathcal{B}^e_0} G_{IJ} \underline{\mathbb{I}} \, \mathrm{d}V, \qquad (4.68)$$

$$\underline{\boldsymbol{K}}^{\boldsymbol{up}}_{IJ} = \int_{\mathcal{B}^e_0} J \underline{\boldsymbol{B}}^{0T}_I \underline{\boldsymbol{C}}^{-1} N^p_J \, \mathrm{d}V, \qquad (4.69)$$

$$\underline{\boldsymbol{K}}^{\boldsymbol{pu}}_{IJ} = \int_{\mathcal{B}^e_0} J N^p_I \underline{\boldsymbol{C}}^{-T} \underline{\boldsymbol{B}}^0_J \, \mathrm{d}V, \qquad (4.70)$$

$$K^{p\theta}_{IJ} = - \int_{\mathcal{B}^e_0} N^p_I N^\theta_J \, \mathrm{d}V, \qquad (4.71)$$

$$K^{\theta p}_{IJ} = - \int_{\mathcal{B}^e_0} N^\theta_I N^p_J \, \mathrm{d}V, \qquad (4.72)$$

$$K^{\theta\theta}_{IJ} = \int_{\mathcal{B}^e_0} \frac{\partial \Psi^2_{vol}}{\partial \theta^2} N^\theta_I N^\theta_J \, \mathrm{d}V. \qquad (4.73)$$

For a given node of a 3D element the corresponding elements of the tangent matrix, solution and residual vector become,

$$\underline{\boldsymbol{K}}_{IJ} = \begin{bmatrix} \left[\underline{\boldsymbol{K}}^{\boldsymbol{uu}}_{IJ} \right]_{3\times 3} & \left[\underline{\boldsymbol{K}}^{\boldsymbol{up}}_{IJ} \right]_{3\times 1} & \left[\boldsymbol{0} \right]_{3\times 1} \\ \left[\underline{\boldsymbol{K}}^{\boldsymbol{pu}}_{IJ} \right]_{1\times 3} & 0 & K^{p\theta}_{IJ} \\ \left[\boldsymbol{0} \right]_{1\times 3} & K^{\theta p}_{IJ} & K^{\theta\theta}_{IJ} \end{bmatrix}_{5\times 5} , \quad \underline{\Delta \boldsymbol{u}}_I = \begin{bmatrix} \Delta u_{1I} \\ \Delta u_{2I} \\ \Delta u_{3I} \\ \Delta p_I \\ \Delta \theta_I \end{bmatrix}_{5\times 1} ,$$

$$\underline{\boldsymbol{R}}_I = \begin{bmatrix} \left[\underline{\boldsymbol{R}}^{\boldsymbol{u}}_I \right]_{3\times 1} \\ R^p_I \\ R^\theta_I \end{bmatrix}_{5\times 1} . \qquad (4.74)$$

An appropriate element type needs to be selected. The order of the shape functions for each solution field can be chosen independently. For the hexahedral case, the family of $Q_k P_{k-1}$ elements has been established in literature, see [80]. In this family of elements, the shape functions for the displacements are by one order higher than the shape functions of the remaining fields. The most simple is the Q1P0 element where p and θ are interpolated with constant functions while $\boldsymbol{u}$ is interpolated with linear ones. The next one on the order refinement scale is the Q2P1 element. The reason for the restriction on the choice of the order of the shape functions comes from the Ladyzenskaya-Babuška-Brezzi (LBB) condition mentioned in [87]. If the discretisation satisfies the LBB condition the numerical solution is unique, robust and converges with optimal order. Numerical examples which reinforce this statement in a heuristic manner can be found in [88] and [89]. The mathematical proof is given in [87].

4.2.3 The Q1P0 Element

As a starting point the Q1P0 element is selected since the shape functions are of lower order and thus, the interpolation is simpler. Even though it does not satisfy the LBB condition according to [80], it is still a good candidate for the numerical implementation as shown in the benchmarks of the present work even though spurious modes can appear, see [80]. The shape functions of p and θ are constant while the displacement $\boldsymbol{u}$ is interpolated with linear shape functions which means that p and θ are discontinuous between the elements. One advantage of the Q1P0 element is the possibility of static condensation. Considering the system of equations (4.74), the variables Δp and $\Delta \theta$ can be condensed by eliminating the proper degrees of freedom. This gives a modified system which has to be solved just for $\Delta \boldsymbol{u}$. The modified tangent matrix after the static condensation is,

$$\underline{\boldsymbol{K}}_{IJ}^{sc} = \left[\underline{\boldsymbol{K}}_{IJ}^{\boldsymbol{uu}} + K^{\theta\theta} K^{p\theta-2} \underline{\boldsymbol{K}}_{I}^{\boldsymbol{up}} \underline{\boldsymbol{K}}_{J}^{pu} \right]. \tag{4.75}$$

The residual after the static condensation becomes,

$$\underline{\boldsymbol{R}}_{I}^{sc} = \left[\underline{\boldsymbol{R}}_{I}^{\boldsymbol{u}} + (K^{\theta\theta} K^{p\theta-2} R^{p} - K^{p\theta-1} R^{\theta}) \underline{\boldsymbol{K}}_{I}^{\boldsymbol{up}} \right]. \tag{4.76}$$

Since only the displacement needs to be solved after the static condensation, the Q1P0 element behaves as a pure displacement element in the global assembly. In the element implementation routine, the additional degrees of freedom p and θ have to be updated in each Newton step according to,

$$\Delta p = K^{\theta\theta} K^{p\theta-2} \underline{\boldsymbol{K}}_{I}^{\boldsymbol{up}} \underline{\Delta \boldsymbol{u}}_{I} + K^{p\theta-1} R^{\theta} - K^{\theta\theta} K^{p\theta-2} R^{p} \tag{4.77}$$

and

$$\Delta \theta = K^{\theta\theta-1} (R^{\theta} - K^{p\theta} \Delta p). \tag{4.78}$$

The updated p and θ are then evaluated in the residuals (4.66) and (4.67). The slight drawback in the Q1P0 element is the fact that locally matrices need to be inverted.

4.2.3.1 The Q1P0 Element for Electromechanical Coupling

The previous description considered only a mechanical element without the electric part of the coupled problem. To implement the Q1P0 element in the electromechanical coupling, proper modifications have to be made. The two field variables p and θ which were introduced in the three field formulation have a purely mechanical nature. For this reason, the modification from a displacement formulation to the three field formulation for

the electromechanical coupling only affects the purely mechanical parts of the residual and the tangent matrix.

The nodal residual vector $\underline{\boldsymbol{R}}_I$ of the coupled field problem in the displacement formulation is outlined in (4.51). For the modification, the mechanical part of the residual $\underline{\boldsymbol{R}}_I^m$ has to be replaced by the static condensed residual in (4.76). After this substitution, the $\underline{\boldsymbol{R}}_I^{\boldsymbol{u}}$ of (4.76) also has to be modified to consider the Maxwell stress. In a purely mechanical context (4.65) is considered as $\underline{\boldsymbol{R}}_I^{\boldsymbol{u}}$. For the electromechanical coupled case this has to be extended by inserting the Maxwell stress as an additional contribution in the mechanical equilibrium, thus

$$\underline{\boldsymbol{R}}_I^{\boldsymbol{u}}(\underline{\boldsymbol{u}}_I, p_I, \theta_I) = \int_{\mathcal{B}_0^e} \underline{\boldsymbol{B}}_I^{0T}(\underline{\boldsymbol{S}}_0^{iso} + \underline{\boldsymbol{S}}_0^{vol} + \underline{\boldsymbol{S}}_0^E)\,\mathrm{d}V. \qquad (4.79)$$

The second modification regards the tangent matrix and follows the same procedure. In the coupled field tangent matrix described in (4.51), the purely mechanical part $\underline{\boldsymbol{K}}_{IJ}^{mm}$ has to replaced with the static condensed tangent matrix introduced in (4.75). Here, the Maxwell stress has not been considered yet. For this reason the term $\underline{\boldsymbol{K}}_{IJ}^{\boldsymbol{u}\boldsymbol{u}}$ in (4.75) needs to be adjusted. For the mechanical case it is described in (4.68). In this equation, the Maxwell stress has to be introduced. The material term has to be modified to

$$2\int_{\mathcal{B}_0^e} \underline{\boldsymbol{B}}_I^{0T}\left(\frac{\partial \underline{\boldsymbol{S}}_0^{vol}}{\partial \underline{\boldsymbol{C}}} + \frac{\partial \underline{\boldsymbol{S}}_0^{iso}}{\partial \underline{\boldsymbol{C}}} + \frac{\partial \underline{\boldsymbol{S}}_0^E}{\partial \underline{\boldsymbol{C}}}\right)\underline{\boldsymbol{B}}_J^0\,\mathrm{d}V. \qquad (4.80)$$

In the geometric part of (4.68) the addition of the mechanical stresses $\underline{\boldsymbol{S}}_0^{iso}$, $\underline{\boldsymbol{S}}_0^{vol}$ and the Maxwell stress $\underline{\boldsymbol{S}}^E$ is considered as the total stress for the geometric stiffness G_{IJ}, see (4.37).

4.2.4   The Q2P1 Element

In the Q2P1 formulation the displacement $\underline{\boldsymbol{u}}$ is approximated with quadratic shape functions while p and θ are approximated linearly. For this interpolation a hexahedral element with 27 nodes can be considered. The quadratic interpolation of the displacement vector $\underline{\boldsymbol{u}}$ is performed with the use of these 27 nodes. Since p and θ are interpolated linearly, only the 8 vertex nodes of the hexahedral element are considered for these fields. In the 3D case this results in the necessity of 5 degrees of freedom (dof's) for the 8 nodes on the vertices. For the remaining nodes only 3 dof's are needed per node. In a finite element program the number of dof's is generally prescribed to be the same on all nodes. This means that 135 dof's are available in the 27 nodes hexahedral element, but only 97 are actually necessary in the 3D Q2P1 interpolation. This requires special attention which will be outlined in the next sentences. First of all it should be clear, that in (4.63) and

(4.64), $N = 27$ for $\underline{\delta u}$, $\underline{\delta G}$, $\underline{\Delta u}$ and $\underline{\Delta G}$. For δp, $\delta \theta$, Δp and $\Delta \theta$ which are interpolated only on the vertices of the hexahedral element, the value is $N = 8$. This means in the consideration of the residuals that $I = 1, ..., 27$ in (4.65) and $I = 1, ..., 8$ in (4.66) and (4.67). For the 3D case the displacement residual in (4.65) has 3 components which means that the residual vector of the element has 81 components. The residuals in (4.66) and (4.67) are scalars, thus the total number of components in the element residual vector is 8 for each one. The submatrix in (4.68) is a 3×3 matrix. The ranges of the indices are $I = 1, ..., 27$ and $J = 1, ..., 27$. Therefore the number of components in the element tangent matrix is 81×81. The submatrix in (4.69) is a 3×1 matrix. Here, the ranges of the indices are $I = 1, ..., 27$ and $J = 1, ..., 8$, meaning that the total number of components is 81×8. The next submatrix in (4.70) is the transpose of the previous matrix which implies a total number of components of 8×81. The remaining submatrices (4.71) - (4.73) are scalars with ranges $I = 1, ..., 8$ and $J = 1, ..., 8$, thus the number of components of each submatrix is 8×8.

The structure of the complete element tangent matrix and internal residual vector is shown in (4.81) and (4.82). The node numbering starts with the numbers 1 to 8 for the nodes on the vertices of the hexahedral element and 9 to 27 for the remaining nodes. For this reason the structure of the tangent matrix and residual vector changes after the row and column 40.

$$
\underline{K} = \begin{bmatrix}
\underline{K}_{1,1}^{uu} & \underline{K}_{1,1}^{up} & \underline{0} & \cdots & \underline{K}_{1,8}^{uu} & \underline{K}_{1,8}^{up} & \underline{0} & \underline{K}_{1,9}^{uu} & \underline{0} & \underline{0} & \cdots & \underline{K}_{1,27}^{uu} & \underline{0} & \underline{0} \\
\underline{K}_{1,1}^{pu} & 0 & K_{1,1}^{p\theta} & \cdots & \underline{K}_{1,8}^{pu} & 0 & K_{1,8}^{p\theta} & \underline{K}_{1,9}^{pu} & 0 & 0 & \cdots & \underline{K}_{1,27}^{pu} & 0 & 0 \\
\underline{0} & K_{1,1}^{\theta p} & K_{1,1}^{\theta\theta} & \cdots & \underline{0} & K_{1,8}^{\theta p} & K_{1,8}^{\theta\theta} & \underline{0} & 0 & 0 & \cdots & \underline{0} & 0 & 0 \\
\vdots & \vdots & \vdots & \ddots & \vdots & \vdots & \vdots & \vdots & \vdots & \vdots & \ddots & \vdots & \vdots & \vdots \\
\underline{K}_{8,1}^{uu} & \underline{K}_{8,1}^{up} & \underline{0} & \cdots & \underline{K}_{8,8}^{uu} & \underline{K}_{8,8}^{up} & \underline{0} & \underline{K}_{8,9}^{uu} & \underline{0} & \underline{0} & \cdots & \underline{K}_{8,27}^{uu} & \underline{0} & \underline{0} \\
\underline{K}_{8,1}^{pu} & 0 & K_{8,1}^{p\theta} & \cdots & \underline{K}_{8,8}^{pu} & 0 & K_{8,8}^{p\theta} & \underline{K}_{8,9}^{pu} & 0 & 0 & \cdots & \underline{K}_{8,27}^{pu} & 0 & 0 \\
\underline{0} & K_{8,1}^{\theta p} & K_{8,1}^{\theta\theta} & \cdots & \underline{0} & K_{8,8}^{\theta p} & K_{8,8}^{\theta\theta} & \underline{0} & 0 & 0 & \cdots & \underline{0} & 0 & 0 \\
\underline{K}_{9,1}^{uu} & \underline{K}_{9,1}^{up} & \underline{0} & \cdots & \underline{K}_{9,8}^{uu} & \underline{K}_{9,8}^{up} & \underline{0} & \underline{K}_{9,9}^{uu} & \underline{0} & \underline{0} & \cdots & \underline{K}_{9,27}^{uu} & \underline{0} & \underline{0} \\
\underline{0} & 0 & 0 & \cdots & \underline{0} & 0 & 0 & \underline{0} & 1 & 0 & \cdots & \underline{0} & 0 & 0 \\
\underline{0} & 0 & 0 & \cdots & \underline{0} & 0 & 0 & \underline{0} & 0 & 1 & \cdots & \underline{0} & 0 & 0 \\
\vdots & \vdots & \vdots & \ddots & \vdots & \vdots & \vdots & \vdots & \vdots & \vdots & \ddots & \vdots & \vdots & \vdots \\
\underline{K}_{27,1}^{uu} & \underline{K}_{27,1}^{up} & \underline{0} & \cdots & \underline{K}_{27,8}^{uu} & \underline{K}_{27,8}^{up} & \underline{0} & \underline{K}_{27,9}^{uu} & \underline{0} & \underline{0} & \cdots & \underline{K}_{27,27}^{uu} & \underline{0} & \underline{0} \\
\underline{0} & 0 & 0 & \cdots & \underline{0} & 0 & 0 & \underline{0} & 0 & 0 & \cdots & \underline{0} & 1 & 0 \\
\underline{0} & 0 & 0 & \cdots & \underline{0} & 0 & 0 & \underline{0} & 0 & 0 & \cdots & \underline{0} & 0 & 1
\end{bmatrix} \quad (4.81)
$$

$$
\underline{R} = \begin{bmatrix} \underline{R}_1^u & R_1^p & R_1^\theta & \cdots & \underline{R}_8^u & R_8^p & R_8^\theta & \underline{R}_9^u & 0 & 0 & \cdots & \underline{R}_{27}^u & 0 & 0 \end{bmatrix}^T \quad (4.82)
$$

The last point, which has to be addressed concerning the assembly of the tangent matrix and residual vector, is the treatment of the unused dof's p and θ on the nodes 9 to 27.

The considered option is to force these dof's to vanish in each element. This is realised by setting the value of 1 on the diagonal of the tangent matrix which are affected by these dof's. In the internal residual vector, the corresponding values are set to 0. This creates an equation for each unused dof which sets its value to 0. In the assembly of the global tangent matrix and residual vector the unused dof's overlap at the corresponding parts. Thus the solution of 0 is still enforced at these dof's.

As a final remark, it should be mentioned, that static condensation in not possible in the Q2P1 element. Since p and θ are continuous, adjacent elements share the same value for these dof's. Therefore they can not be treated as internal element variables anymore. This fact also needs to be considered carefully when dealing with inhomogeneous problems, where jumps in p and θ may occur from a physical point of view. Numerical examples of the Q2P1 element implementation can be reviewed in [90].

4.2.4.1   The Q2P1 Element for Electromechanical Coupling

The implementation of the Q2P1 element has certain similarities and differences with respect to the implementation of the Q1P0 element. The extension of the Q2P1 element interpolation towards electromechanical coupling is straightforward. The number of dof's is extended by one on each node of the hexahedral element to include the electric potential φ which is discretised with quadratic shape functions. This extension results in a system for each node, which has the following structure

$$
\underline{\boldsymbol{K}}_{IJ} = \begin{bmatrix} \left[\underline{\boldsymbol{K}}_{IJ}^{\boldsymbol{uu}}\right]_{3\times3} & \left[\underline{\boldsymbol{K}}_{IJ}^{\boldsymbol{up}}\right]_{3\times1} & \left[\boldsymbol{0}\right]_{3\times1} & \left[\underline{\boldsymbol{K}}_{IJ}^{me}\right]_{3\times1} \\ \left[\underline{\boldsymbol{K}}_{IJ}^{\boldsymbol{pu}}\right]_{1\times3} & 0 & K_{IJ}^{p\theta} & 0 \\ \left[\boldsymbol{0}\right]_{1\times3} & K_{IJ}^{\theta p} & K_{IJ}^{\theta\theta} & 0 \\ \left[\underline{\boldsymbol{K}}_{IJ}^{em}\right]_{1\times3} & 0 & 0 & K_{IJ}^{ee} \end{bmatrix}_{6\times6} , \quad \underline{\Delta\boldsymbol{u}}_I = \begin{bmatrix} \Delta u_{1I} \\ \Delta u_{2I} \\ \Delta u_{3I} \\ \Delta p_I \\ \Delta \theta_I \\ \Delta \varphi_I \end{bmatrix}_{6\times1} ,
$$

$$
\underline{\boldsymbol{R}}_I = \begin{bmatrix} \left[\underline{\boldsymbol{R}}_I^{\boldsymbol{u}}\right]_{3\times1} \\ R_I^p \\ R_I^{\theta} \\ R_I^e \end{bmatrix}_{6\times1} . \tag{4.83}
$$

The implementation of the Maxwell stress and its derivative w.r.t. the right Cauchy-Green strain has to be realised in the same manner as described in 4.2.3.1. This affects the internal residual vector $\underline{\boldsymbol{R}}_I^{\boldsymbol{u}}$ and the tangent submatrix $\underline{\boldsymbol{K}}_{IJ}^{\boldsymbol{uu}}$ in (4.83). In the assembly of the nodal matrices and vectors to the complete system of the element, the same strategies as described in 4.2.4 are applicable. This concerns the rows and columns of the system

which correspond to p and θ for the nodal values $N = 9, ..., 27$. For the unused dof's the same method is applied by setting the value 1 in the corresponding part of the tangent matrix und setting the value to 0 in the internal residual vector.

4.3 Extension to Dynamics

The purpose of this section is to review the concepts for solving mechanical time dependent initial boundary value problems. These concepts are then adapted to the coupled field implementation as performed in [91]. Thus enabling the consideration of dynamic effects in the DEA simulation.

4.3.1 The Residual Vector for the Dynamic Case

If dynamic effects are to be considered in the numerical simulation of a mechanical problem, the inertia appears as an additional force on the the system. This force is proportional to the acceleration of the body in which the proportionality factor is the mass. Additionally, damping effects can also be considered in the sense of a force which is proportional to the velocity of a material point. This factor is known as the damping coefficient d. With the consideration of these two effects, the internal residual vector known from the static analysis, see (4.29) or (4.65), is extended by two additional terms, which address these effects. In a reference configuration formulation the internal residual vector would be described as

$$\underline{\boldsymbol{R}}_I(\underline{\boldsymbol{u}}_I) = \int_{\mathcal{B}_0^e} \underline{\boldsymbol{B}}_I^{0T} \underline{\boldsymbol{S}}_0 \, \mathrm{d}V + \int_{\mathcal{B}_0^e} N_I \rho_0 \underline{\boldsymbol{a}} \, \mathrm{d}V + \int_{\mathcal{B}_0^e} N_I d_0 \underline{\boldsymbol{v}} \, \mathrm{d}V, \qquad (4.84)$$

in which ρ_0 and d_0 are the mass density and damping coefficient per unit volume in the reference configuration. Now that the two field variables $\underline{\boldsymbol{a}}$ and $\underline{\boldsymbol{v}}$ are introduced to describe the acceleration and the velocity, they have to be discretised. This can be done with the same spacial concept as in the displacement discretisation by the use of shape functions N_J. Thus, the discrete versions of the acceleration and velocity are

$$\underline{\boldsymbol{a}} = \sum_{J=1}^{N} N_J \underline{\boldsymbol{a}}_J, \qquad \underline{\boldsymbol{v}} = \sum_{J=1}^{N} N_J \underline{\boldsymbol{v}}_J. \qquad (4.85)$$

By substituting the discretisation (4.85) into (4.84) the internal residual can be written in the form

$$\underline{\boldsymbol{R}}_I(\underline{\boldsymbol{u}}_I) = \underline{\boldsymbol{R}}_I^{stat}(\underline{\boldsymbol{u}}_I) + \sum_{J=1}^{N} \underline{\boldsymbol{M}}_{IJ} \underline{\boldsymbol{a}}_J + \sum_{J=1}^{N} \underline{\boldsymbol{D}}_{IJ} \underline{\boldsymbol{v}}_J. \qquad (4.86)$$

The first term on the right hand side is the internal residual vector known from quasi-static considerations. The matrices, which appear in the second and third term, are known as the mass and damping matrix which possess a block diagonal structure

$$\underline{\boldsymbol{R}}_I^{stat} = \int_{\mathcal{B}_0^e} \boldsymbol{B}_I^{0^T} \underline{\boldsymbol{S}}_0 \, \mathrm{d}V, \quad \underline{\boldsymbol{M}}_{IJ} = \int_{\mathcal{B}_0^e} \rho_0 N_I N_J \boldsymbol{1} \, \mathrm{d}V, \quad \underline{\boldsymbol{D}}_{IJ} = \int_{\mathcal{B}_0^e} d_0 N_I N_J \boldsymbol{1} \, \mathrm{d}V. \quad (4.87)$$

The field variables $\underline{\boldsymbol{a}}$ and $\underline{\boldsymbol{v}}$ have been introduced as independent solution fields in the problem. Since they are dependent on the displacement $\underline{\boldsymbol{u}}$ by the time parameter, a proper time integration algorithm has to be chosen, which involves the time variable t as a stepping parameter. Besides the boundary values, initial conditions are also required for the solution process.

4.3.2   Solution with Time Discretisation

In the solution process of a dynamic problem the time parameter t is introduced into the solution procedure. This enables the relationship between $\underline{\boldsymbol{a}}$, $\underline{\boldsymbol{v}}$ and $\underline{\boldsymbol{u}}$ by the derivative w.r.t. the time t according to

$$\underline{\boldsymbol{v}} = \dot{\underline{\boldsymbol{u}}}, \quad \underline{\boldsymbol{a}} = \dot{\underline{\boldsymbol{v}}}. \quad (4.88)$$

In the numerical context the time parameter is discretised in steps $\Delta t = t_{n+1} - t_n$. The time step, in which the initial conditions are prescribed, is represented by t_0. In each time step the balance of momentum has to be fulfilled according to

$$\underline{\boldsymbol{M}}\,\underline{\boldsymbol{a}} + \underline{\boldsymbol{D}}\,\underline{\boldsymbol{v}} + \underline{\boldsymbol{R}}^{stat}(\underline{\boldsymbol{u}}) = \underline{\boldsymbol{P}}, \quad (4.89)$$

where $\underline{\boldsymbol{P}}$ represents the external force vector. This could be an initial force which just acts on the first time step t_0 to put the system in motion or it could be a time dependent force acting during the complete dynamic process. Generally, $\boldsymbol{u}_0$ and $\boldsymbol{v}_0$ are given as initial conditions. To obtain $\underline{\boldsymbol{a}}_0$, the balance of linear momentum (4.89) has to be considered. This gives the initial acceleration by

$$\underline{\boldsymbol{a}}_0 = \underline{\boldsymbol{M}}^{-1} \left[-\underline{\boldsymbol{D}}\,\underline{\boldsymbol{v}}_0 - \underline{\boldsymbol{R}}^{stat}(\underline{\boldsymbol{u}}_0) + \underline{\boldsymbol{P}}_0 \right]. \quad (4.90)$$

Starting at the initial time step, the integration scheme has to solve the balance of momentum in each time step successively. To perform this, a variety of algorithms can be considered which can roughly be classified into explicit and implicit schemes. The explicit schemes are characterised by the fact that the variables of the solution are written as a function of the previous time step t_n. This simplifies the implementation process but at the cost of instabilities in the integration scheme with larger time steps. In implicit schemes the variables of the solution are written as a function of the previous

time step t_n and the actual time step t_{n+1}. The implementation is more complex, but in general larger time steps are admissible for stable solutions. One frequently used time integration algorithm for second order differential equations in structural mechanics is the Newmark method. It is characterised by the time discretisation of the displacement and velocity according to

$$\underline{u}_{n+1} = \underline{u}_n + \Delta t \underline{v}_n + \Delta t^2 \left[\left(\frac{1}{2} - \beta \right) \underline{a}_n + \beta \underline{a}_{n+1} \right], \tag{4.91}$$

$$\underline{v}_{n+1} = \underline{v}_n + \Delta t \left[(1 - \gamma) \underline{a}_n + \gamma \underline{a}_{n+1} \right]. \tag{4.92}$$

The parameters $0 \leq \beta \leq 0.5$ and $0 \leq \gamma \leq 1$ serve as algorithmic parameters, which control the behaviour of the algorithm. Of these two parameters, β is mainly responsible for the stability. In the case of $\beta = 0$ the time integration scheme becomes an explicit one. Furthermore, values of $\beta < 0.25$ should be avoided since the algorithm becomes only conditionally stable in this setting.

In every time step of the integration scheme the nonlinear system of equations given in (4.89) has to be solved. With the neglection of external loads, the residual in (4.86) has to converge towards zero in the actual time step, which means that

$$\underline{R}_{n+1} = \underline{R}_{n+1}^{stat} + \underline{M} \, \underline{a}_{n+1} + \underline{D} \, \underline{v}_{n+1} = \underline{0}. \tag{4.93}$$

Because of the nonlinear nature of the problem, the derivative of the residual w.r.t. the displacement, which defines the tangent matrix, is necessary. Since the residual (4.86) is formulated in dependency of $\underline{u}$, $\underline{v}$ and $\underline{a}$, the chain rule can be applied,

$$\underline{K} = \frac{\partial \underline{R}_{n+1}}{\partial \underline{u}_{n+1}} + \frac{\partial \underline{R}_{n+1}}{\partial \underline{v}_{n+1}} \frac{\partial \underline{v}_{n+1}}{\partial \underline{u}_{n+1}} + \frac{\partial \underline{R}_{n+1}}{\partial \underline{a}_{n+1}} \frac{\partial \underline{a}_{n+1}}{\partial \underline{u}_{n+1}}. \tag{4.94}$$

Under a closer examination of (4.94) the following identities emerge in the equation,

$$\frac{\partial \underline{R}_{n+1}}{\partial \underline{u}_{n+1}} = \frac{\partial \underline{R}_{n+1}^{stat}}{\partial \underline{u}_{n+1}} = \underline{K}^{stat}, \quad \frac{\partial \underline{R}_{n+1}}{\partial \underline{v}_{n+1}} = \underline{D}, \quad \frac{\partial \underline{R}_{n+1}}{\partial \underline{a}_{n+1}} = \underline{M}. \tag{4.95}$$

The two remaining partial derivatives in (4.94) depend on the considered time discretization. For the Newmark algorithm, in which the time discretisation is performed according to (4.91) and (4.92), the derivatives are

$$\frac{\partial \underline{v}_{n+1}}{\partial \underline{u}_{n+1}} = \frac{\gamma}{\beta \Delta t}, \quad \frac{\partial \underline{a}_{n+1}}{\partial \underline{u}_{n+1}} = \frac{1}{\beta \Delta t^2}. \tag{4.96}$$

Substituting (4.95) and (4.96) into (4.94) states the tangent matrix of the dynamic problem as an extension of the tangent of the static problem,

$$\underline{\boldsymbol{K}} = \underline{\boldsymbol{K}}^{stat} + \frac{\gamma}{\beta \Delta t} \boldsymbol{D} + \frac{1}{\beta \Delta t^2} \boldsymbol{M}. \tag{4.97}$$

Besides the tangent matrix known from nonlinear statics, the mass and the damping matrix have to be added. Both matrices are multiplied by a factor which depends on the time step size and the parameters β and γ.

4.3.3   Implementation of the Dynamic Parts into the Coupled Field Problem

So far, the dynamics aspects have only been contemplated from the mechanical point of view. When it comes to the coupling of dynamic deformations with electrostatics, the term electrostatics is strictly speaking not appropriate anymore. Obviously, the electric field will be time dependent as a consequence of the coupling with dynamic deformations. Since the oscillation frequencies of a DEA remain in the range of mechanical ones, electrodynamic effects will not occur and for this reason the electrostatic assumption remains valid. For this reason, the extension of the numerical implementation towards dynamic considerations only affects the mechanical part of the coupled field problem. With this, the extension is a straightforward task. Considering the displacement formulation in 4.2.1, the mechanical residual in (4.29) is modified by adding the mass and damping terms mentioned in (4.84),

$$\underline{\boldsymbol{R}}_I^m(\underline{\boldsymbol{u}}_I, \varphi_I) = \int_{\mathcal{B}_0^e} \boldsymbol{B}_I^{0^T} \boldsymbol{T}_0 \, \mathrm{d}V + \int_{\mathcal{B}_0^e} N_I \rho_0 \underline{\boldsymbol{a}} \, \mathrm{d}V + \int_{\mathcal{B}_0^e} N_I d_0 \underline{\boldsymbol{v}} \, \mathrm{d}V. \tag{4.98}$$

The residual in (4.31) remains unmodified. In the tangent matrix (4.33) only the submatrix $\underline{\boldsymbol{K}}_{IJ}^{mm}$ has to be extended. This means that (4.40) is modified into

$$\underline{\boldsymbol{K}}_{IJ}^{mm} = 2 \int_{\mathcal{B}_0^e} \boldsymbol{B}_I^{0^T} \left(\frac{\partial \underline{\boldsymbol{S}}}{\partial \underline{\boldsymbol{C}}} + \frac{\partial \underline{\boldsymbol{S}}^E}{\partial \underline{\boldsymbol{C}}} \right) \boldsymbol{B}_J^0 \, \mathrm{d}V \tag{4.99}$$

$$+ \int_{\mathcal{B}_0^e} G_{IJ} \mathbb{I} \, \mathrm{d}V + \frac{\gamma}{\beta \Delta t} \boldsymbol{D}_{IJ} + \frac{1}{\beta \Delta t^2} \underline{\boldsymbol{M}}_{IJ}. \tag{4.100}$$

The extension procedure outlined here is also applicable to the mixed element formulations Q1P0 and Q2P1. Starting from the residual vectors and tangent matrices mentioned in 4.2.3.1 and 4.2.4.1 the same modifications as described in (4.98) and (4.99) can be performed on the mechanical parts.

Chapter 5

Stability of Incompressible DEAs

After having described the methodology of the numerical implementation in the previous chapter, the evaluation of the implementation with specific benchmarks would be the next step. But before this evaluation is performed, the topic of the stability of DEAs is addressed here.

Considering (3.40) reveals that the attraction force which acts on the electrodes of a parallel plate capacitor depends quadratically on the electric field. The electric field is inversely proportional to the separation distance between the electrodes. Considering a DEA which consists of a deformable parallel plate capacitor in which the potential difference is kept constant, it becomes clear that halving the separation distance of the electrodes will increase the attraction force on the electrodes by a factor 4. In simple words, the attraction force between the electrodes of a deformable parallel plate capacitor is inversely proportional to the square of the electrodes separation distance.

In a DEA, or a parallel plate capacitor with dielectric, the attraction force of the electrodes is equilibrated by the elastic forces of the deformed dielectric. If an elastomer is subjected to compression during an uniaxial test, it can be observed that the increase of the reaction force is lower than the increase of the attraction force between the electrodes for a given deformation. So if the attraction forces of the electrodes increases faster than the equilibrating elastic reaction forces of the elastomer, a point will be reached during the compression of the DEA where the elastic forces can not equilibrate the attraction forces anymore. This point is defined as the critical point at which the stability of the DEA switches from stable to unstable.

The scope of the present chapter is to present a stability analysis for a parallel plate DEA under the consideration of a neo-Hooke and Yeoh material model. The analysis is performed in 1D with the assumption of perfect incompressibility. The last section of

the chapter offers a comparison of the 1D equilibrium solution derived in this chapter with numerical solutions which are performed according to the implementation described in chapter 4. Additional literature regarding the investigation of the stability and electromechanical failure of DEAs can be found in [92–97].
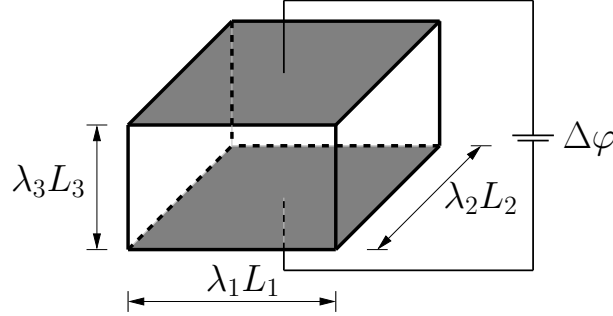
5.1 Equilibrium of DEAs

FIGURE 5.1: Geometry of a deformed DEA under electrostatic loading.

As mentioned in (4.6), the electromechanical coupling in a DEA is contemplated as a balance between the mechanical Cauchy stress $\boldsymbol{\sigma}$ and the electrostatic Maxwell stress $\boldsymbol{\sigma}^e$. The sum of both stresses form the total stress $\boldsymbol{\tau}$ which is in equilibrium with the external mechanical volume loads. In Fig. 5.1 a simple electrostatic loading of a DEA hexahedron is depicted. In the undeformed state, the DEA geometry has the edge length L_i. If a potential difference $\Delta\varphi$ is applied on the electrodes, the edges are deformed to lengths $\lambda_i L_i$. For a loading as described, in which external mechanical forces are not considered, the normal components of the total stress vanish,

$$\tau_i = \sigma_i + \sigma_i^e = 0, \tag{5.1}$$

for $i = 1, 2, 3$. The normal components σ_i of $\boldsymbol{\sigma}$ are

$$\sigma_i = \lambda_i \Psi_{,i} + p. \tag{5.2}$$

The normal stretches are described by λ_i while p stands for the hydrostatic pressure. The free energy which is defined by the material model is denoted by Ψ. The derivative w.r.t. the normal stretch is represented by a comma, thus $\Psi_{,i} = \partial\Psi/\partial\lambda_i$. The definition of the Maxwell stress for polarisable matter has been introduced in chapter 3.4. The normal components for the given loading situation are,

$$\sigma_3^e = \frac{(2\epsilon - \epsilon_0)}{2\lambda_3^2} E^2, \quad \sigma_1^e = \sigma_2^e = -\frac{\epsilon_0 E^2}{2\lambda_3^2}. \tag{5.3}$$

The permittivity of vacuum and the absolute permittivity of the dielectric are described by ϵ_0 and ϵ. The nominal electric field is defined via $E = \Delta\varphi/L_3$. After the substitution of (5.2) and (5.3) in (5.1) the hydrostatic pressure p can be factored out. With the elimination of p in the components of the total stress which are transversal to the electric field ($i = 1, 2$) one obtains

$$\lambda_1 \Psi_{,1} = \lambda_2 \Psi_{,2}. \tag{5.4}$$

Furthermore, p can be substituted from the component τ_1 or τ_2 in τ_3. Substituting τ_1 in τ_3 the following relation is obtained,

$$\epsilon E^2 \lambda_3^{-2} + \lambda_3 \Psi_{,3} - \lambda_1 \Psi_{,1} = 0. \tag{5.5}$$

The assumption of incompressibility is made here. For this case, the stretches of the DEA fulfill the relation

$$\lambda_1 \lambda_2 \lambda_3 = 1. \tag{5.6}$$

With the material model (Ψ), the undeformed geometry of the DEA (L_i) and the electrostatic loading ($\Delta\varphi$), the remaining unknowns to be solved for are the stretches λ_i. These can be obtained from the system of equations (5.4) - (5.6), thus the deformation of the DEA can be determined.

5.1.1 Specific Material Models

To solve the system (5.4) - (5.6) a material model has to be defined which could be e.g. the neo-Hooke or the Yeoh model. In the incompressible Neo-Hooke model, the strain energy is defined by the first invariant of the right Cauchy-Green tensor according to

$$\Psi^{nh} = \frac{\mu}{2}(I_1 - 3). \tag{5.7}$$

The Lamé parameter μ represents the shear modulus. The first invariant is defined by the stretches according to

$$I_1 = \lambda_1^2 + \lambda_2^2 + \lambda_3^2. \tag{5.8}$$

With the substitution of Ψ^{nh} in (5.4) and the consideration of the incompressibility constraint (5.6), the transversal stretches can be obtained in relation to the stretch in loading direction,

$$\lambda_1 = \lambda_2 = \lambda_3^{-\frac{1}{2}}. \tag{5.9}$$

The substitution of the kinematic relation (5.9) in (5.5) leads to the 1D equilibrium equation of the incompressible neo-hookean DEA,

$$E^2 = \frac{\mu}{\epsilon}(\lambda_3 - \lambda_3^4). \tag{5.10}$$

For a given nominal electric field E, the vertical compression stretch λ_3 can be obtained by this equation.

The incompressible Yeoh model is the second model which is considered in this chapter. It is defined in a similar manner as the neo-Hooke model but with two additional terms of second and third order. Therefore three parameters c_1, c_2 and c_3 are necessary. The free energy is defined by

$$\Psi^{ye} = c_1(I_1 - 3) + c_2(I_1 - 3)^2 + c_3(I_1 - 3)^3. \tag{5.11}$$

The kinematic relation (5.9) is also valid for the Yeoh model. Substituting (5.9) and (5.11) in (5.5) provides the 1D equilibrium equation for the Yeoh DEA,

$$E^2 = \frac{2}{\epsilon}(\lambda_3 - \lambda_3^4)h_1, \tag{5.12}$$

with

$$h_1 = c_1 + 2c_2(I_1 - 3) + 3c_3(I_3 - 3)^2. \tag{5.13}$$

At first glance this equation appears very similar to the neo-Hookean (5.10), but the factor h_1 increases the order since it is dependent on the stretches λ_i by the first invariant I_1.

5.2 Stability of DEAs

The higher order of the 1D equilibrium solutions of the neo-Hooke and Yeoh DEA, described in eq. (5.10) and (5.12), suggests the existence of more than one solution for the equilibrium state. So far, no considerations have been made regarding the structural stability of the DEA depicted in Fig. 5.1. In [98] a stability analysis is performed considering the Lagrange multiplier method. In this analysis, (5.5) is regarded as a function of the stretches λ_i with the constraints (5.4) and (5.6). The main result of the mentioned analysis is the critical nominal electric field $E_c(\lambda_3)$. If the nominal electric field from the equilibrium solution is less than the critical nominal electric field for a given deformation state λ_3, the equilibrium is stable. In the case of the neo-Hooke DEA, the critical electric field is given by

$$E_c^2 = \frac{\mu}{\epsilon}(\lambda_3^4 + \frac{\lambda_3}{2}). \tag{5.14}$$

For the Yeoh model it is

$$E_c^2 = (2\lambda_3^4 + \lambda_3)\frac{h_1}{\epsilon} + 4(\lambda_3^3 - 1)\frac{h_2}{\epsilon}, \tag{5.15}$$

with

$$h_2 = c_2 + 3c_3(I_1 - 3). \tag{5.16}$$

A straightforward approach for a stability analysis is the derivation of the total stress τ_3 w.r.t. the strain λ_3. If the derivative is positive or negative, the equilibrium state is stable or unstable respectively. At a critical stretch, where the equilibrium changes stability, the derivative vanishes. The total stress in the electric field direction for the DEA modelled by the neo-Hooke constitutive law is

$$\tau_3 = \epsilon E^2 + \mu(\lambda_3^4 - \lambda_3) = 0. \tag{5.17}$$

At a critical critical stretch the derivative has to vanish, thus

$$\frac{\partial \tau_3}{\partial \lambda_3} = \mu(4\lambda_3^3 - 1) \overset{!}{=} 0. \tag{5.18}$$

This cubic polynomial function has only one real root which is

$$\lambda_3^c = 4^{-\frac{1}{3}} \approx 0.630. \tag{5.19}$$

At stretches $\lambda_3 > \lambda_3^c$ the derivative is positive while for $\lambda_3 < \lambda_3^c$ it becomes negative. Physically speaking, this means that the nominal electric field can be increased from $E = 0$ where $\lambda_3 = 1$ until the stretch $\lambda_3^c \approx 0.630$ is reached. If E is increased further, the equilibrium switches to unstable resulting in a collapse of the DEA structure. In reality an electric breakdown will occur in the unstable region but this phenomenon is not considered in the scope of the present work. An electric breakdown means that the insulating property of the DEA fails, thus resulting in a shortcut in the electric power source.

The same steps regarding the stability analysis can also be carried out for the Yeoh DEA. Because of the additional terms of higher order in the Yeoh equilibrium solution, the analytical derivation is more tedious and is omitted here for the sake of brevity. In this case two critical stretches exist:

$$\lambda_3^c \approx 0.257 \quad \text{and} \quad \lambda_3^c \approx 0.681. \tag{5.20}$$

Interestingly the Yeoh model offers two critical points. The derivative is positive in the regions $\lambda_3 > 0.681$ and $\lambda_3 < 0.257$. In between the behaviour is unstable. Thus for an increasing nominal electric field the equilibrium will remain stable until the stretch

$\lambda_3 = 0.681$ is reached. After a further increase of E, the DEA structure will bifurcate into an equilibrium state in the second region taking a stretch which corresponds to the equilibrium solution of the given E. Decreasing the electric field at this point will reduce the stretch until $\lambda_3 = 0.257$ is reached, a further decrease of E will produce a structural bifurcation to the equilibrium state in the first region. In this analysis the electric breakdown has been neglected. So it should be pointed out, that an electric breakdown will probably occur while the structure switches from the first stable region into the second one while E is increased.

Taking a look at (5.18) another interesting observation emerges. The critical stretches for a DEA are independent of the material parameters. Only the form of the material function Ψ determines the critical points for the DEA. For this reason the selection of a proper constitutive law is of high importance when it comes to stability analysis of DEAs.

5.3   Operational Curves of DEAs

The purpose of this section is to compare the 1D equilibrium solutions introduced previously with numerical simulations. Since the geometry of the DEA in Fig. 5.1 is rather simple, a discretisation with one finite element is sufficient for the numerical analysis. A brick element of 8 nodes with linear shape functions is considered. The element is implemented with a displacement formulation according to 4.2.1. The constitutive neo-Hooke and Yeoh laws are implemented by the means of 2.3.1.1 and 2.3.1.3. It also should be noted that this benchmark serves as a first check for the numerical implementation.

The dimension of the element are set to $L_1 = L_2 = L_3 = 10\,\text{mm}$. The potential difference is applied by setting the electric degree of freedom $\varphi = 0$ on the four bottom nodes and $\varphi > 0$ on the four top nodes of the element. The potential φ is increased linearly on the top nodes in loading steps of 290 V. For the given geometry this results in a nominal electric field E_0[2] which is increased in steps of $29\,\text{V/mm}$. The material parameter for the neo-Hooke model is set to $\mu = 73\,\text{kPa}$. In the Yeoh model the parameters are $c_1 = \frac{1}{2}\mu = 36.5\,\text{kPa}$, $c_2 = -0.1c_1$ and $c_3 = 0.01c_1$. In both cases $\epsilon_r = 4.7$ is used. Since the models of the numerical simulation are compressible and are compared to a 1D analytical incompressible result, a perfect coincidence is not expected. For comparison purposes the Poisson's ratios are set to three different values, namely $\nu = 0.3, 0.4$ and 0.49.

---

[2]In this work the nominal electric field E_0 is always given in scalar notation for the reason that it has only one non-vanishing component which is perpendicular to the charged surfaces of the actuator.
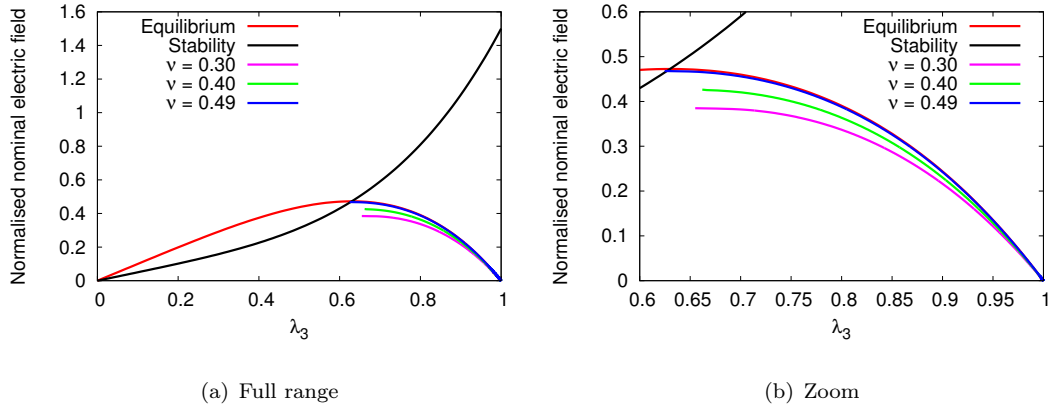
(a) Full range

(b) Zoom

FIGURE 5.2: Stability and equilibrium curves of a DEA with neo-Hooke model.
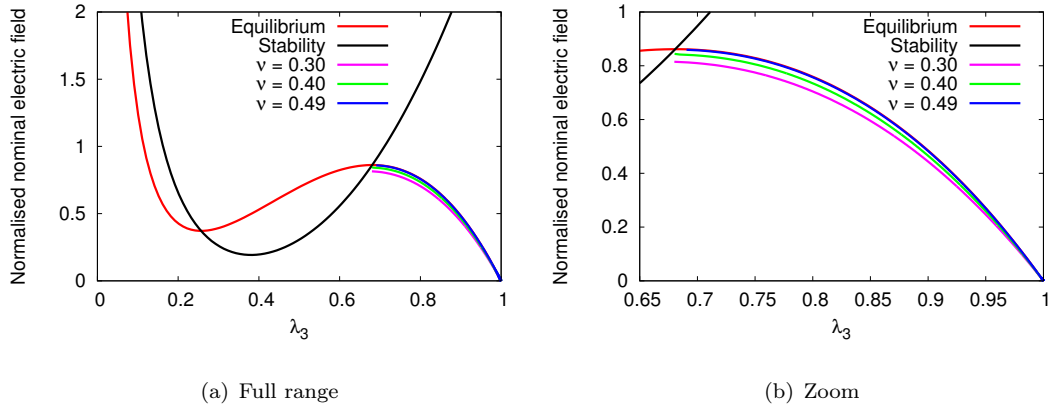

(a) Full range

(b) Zoom

FIGURE 5.3: Stability and equilibrium curves of a DEA with Yeoh model.

The results of the simulations for both models are depicted in Figs. 5.2 and 5.3. Also the curves of the analytical 1D equilibrium solution E (red curve) and the critical electric field E_c (black curve) are shown. The remaining curves (blue, green and magenta) represent the results of the simulation. The subplots Fig. 5.2.(b) and 5.3.(b) depict a zoom in the stable equilibrium region. In the case of the Yeoh model, only the first stable region is zoomed.

The first observation is the influence of the value of ν on the operational curve. An increase of ν towards a value of 0.5 leads to a better approximation of the numerical solution w.r.t. the incompressible analytical solution. It also can be observed that a lower Poisson's ratio ν leads to higher stretches for a given electric field. If the material is more compressible, the stretch increases. The second observation concerns the stability of the DEA. As the electric field is increased during the numerical simulation, direct solutions can only be obtained in the stable regions. As the stretch reaches the critical point (intersection of the black and red curve) the Newton procedure stops to converge in the simulation. This means that the instability of the DEA is rendered by the loss of

convergence in the Newton procedure. To obtain an equilibrium solution in the unstable region, a special treatment will be necessary. A suggestion is an arc length procedure for the coupled field problem.

Chapter 6

Benchmarks with Homogeneous Materials

The present chapter deals with the numerical analysis of DEs and the implementation scheme shown in chapter 4. To start with simple examples, the chapter is restricted to homogeneous DE materials. For this purpose, appropriate geometries for DEAs are chosen and the material parameters are set to specific values. The chapter is subdivided in two main sections to study the quasi-static and the dynamic situations separately. For the dynamic examples, the numerical implementation has been extended according to section 4.3.

6.1 Quasi-Static Analysis

In this section, two benchmarks are considered. The first example studies the effects of the incompressibility constraint on a simplified geometry. The second benchmark provides an application example which consists of a DE tube acting as a fluid pump.

6.1.1 Embedded DE Block

The purpose of this benchmark is to show the volumetric locking effect for the DE electromechanical coupled problem. To this end, a cubic geometry as shown in Fig. 6.1, is considered. The boundary conditions are given in the cross section view depicted in Fig. 6.2. The normal displacements on the four lateral and the bottom face of the cube are constrained. With these conditions the DE block can be considered as perfectly embedded without friction. The top electrode only covers a quarter of the upper surface.
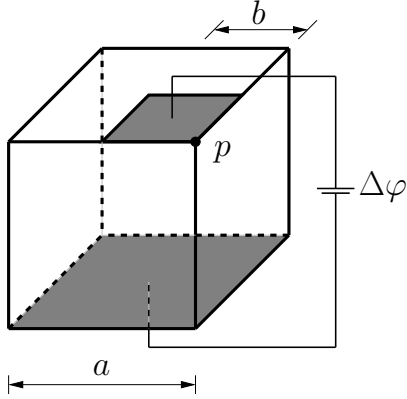
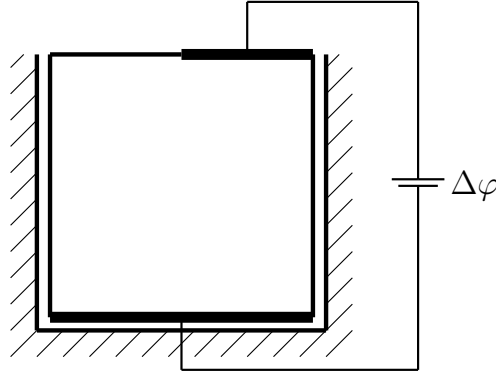FIGURE 6.1: DEA with a partial top electrode. $a = 10$ mm, $b = 5$ mm.

FIGURE 6.2: Cross section with boundary conditions of the embedded DEA.

As a potential difference is applied on the electrode pair, the DE is compressed under the top electrode. With the given boundary conditions and under the consideration of a nearly incompressible material, it is expected for the DE material to be displaced outwards at the top surface where it is not covered by the electrode.

The cube geometry is discretized with 10 elements in each space direction resulting in 1000 volume elements. The dimensions given in Fig. 6.1 are $a = 10$ mm and $b = 5$ mm. The electric potential difference is applied on the electrode pair in 100 steps increasing linearly from 0 to 50 kV which leads to a maximum nominal electric field of 5 kV/mm. To observe the locking effect in this benchmark, the results using the displacement formulation are compared with those of the three field formulation. The first calculation uses the neo-Hooke model defined in 2.3.1.1 while the formulation of the second simulation can be found in 2.3.2. The respective discretisations are given in 4.2.1 and 4.2.3. The material parameters for both formulations are $\mu = 73$ kPa and $\epsilon_r = 4.7$. To study the effects of the incompressibility constraint, the Poisson's ratio ν is varied from 0.49 to 0.4999.

The compression of the cube in vertical direction at the point p of Fig. 6.1 as a function of the applied electric field is depicted in Fig. 6.3. The compression curves of the displacement formulation are represented in red and the disadvantage of the formulation becomes obvious. As the value of ν approaches 0.5 for incompressibility, volumetric locking takes place which leads to a lower compression for a given electric field. In the case of the three field formulation (blue compression curves) the locking effect almost disappears. Even though the value of ν is varied, the difference for the three field formulation is considerably smaller than for the displacement formulation.

A second comparison of both formulations is made in Figs. 6.4.(a) and 6.4.(b) with
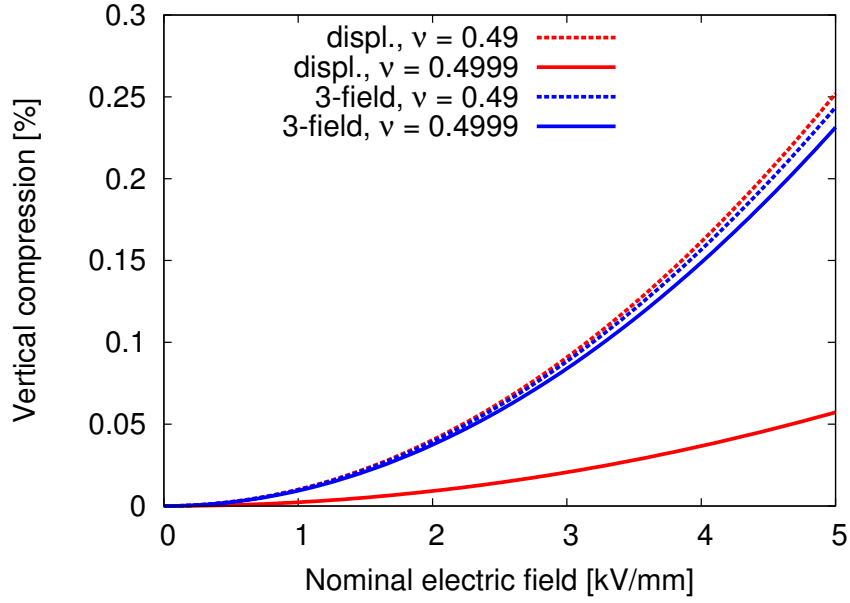
FIGURE 6.3: Vertical compression of the embedded DEA at point p.

a scaling factor of 10. The Poisson's ratio is set to $\nu = 0.4999$, rendering quasi-incompressibility and the potential difference on the electrodes is $\Delta\varphi = 50\,\text{kV}$. The deformed geometry of the DE block for the displacement formulation case is depicted in Fig. 6.4.(a). A considerably small deformation is observed in the region of the top electrode. Furthermore, on the diagonally opposite region of the top electrode a small downward displacement is apparent. This displacement is similar to the one under the top electrode and can be regarded as an artificial locking effect. The deformation for the three field formulation case is represented in Fig. 6.4.(b). In comparison to the displacement formulation case, the deformation under the upper electrode region is considerably larger. Furthermore, in the region next to the top electrode the DE material is displaced in upward direction. This seems to be more physical than the deformation given in Fig. 6.4.(a).

(a) Displacement formulation

(b) Three field formulation
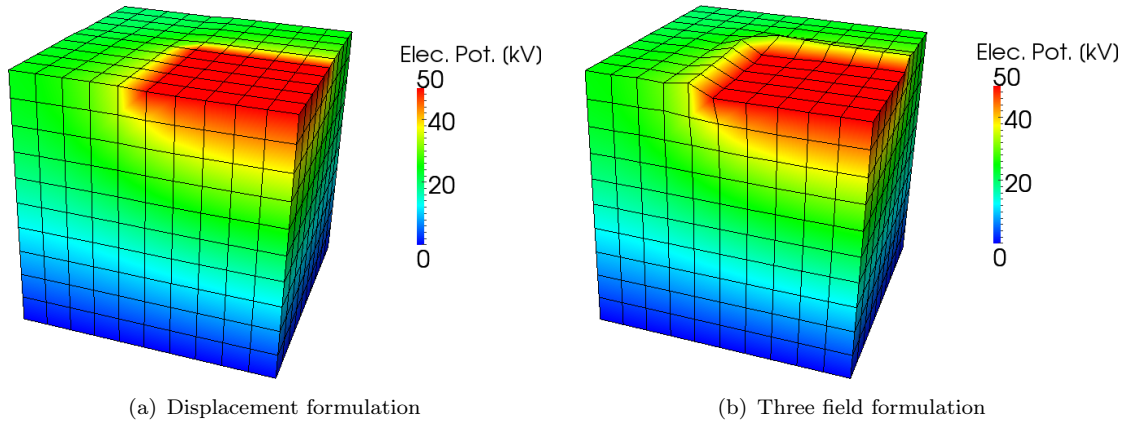
FIGURE 6.4: Deformation of the embedded DEA (10x magnification)

6.1.2   DE Tube Pump

This example provides a motivation for a practical application. Since DEs are flexible materials, a deformable tube acting as a fluid pump is an interesting setup. This could be realised by a cylindrical tube made of DE material and an array of electrode rings along the longitude of the DE tube. Thus the actuation mechanism of the DE tube pump is similar to the one of a peristaltic pump.

The geometry of a short DE tube is presented in Fig. 6.5, where the dimensions are given in mm. Three pairs of electrodes, each with a length of 10 mm, are arranged on the inner and outer wall of the tube. An electric potential difference can be applied on the inner and outer electrode of each pair independently. As known from the previous examples, the application of a potential difference on the electrodes produces a compression of the material. This creates an increase of the diameter of the tube at the activated electrode pair.
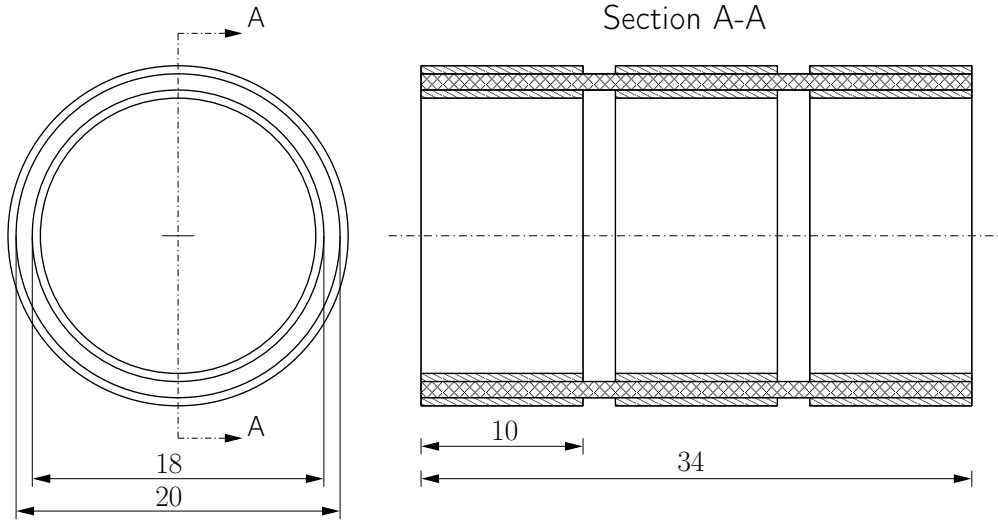
FIGURE 6.5: Geometry of a cylindrical DE tube with dimensions in mm which is activated by three pairs of electrodes.

Because of symmetry conditions, a quarter of the tube geometry with the corresponding boundary conditions is sufficient for the numerical simulation. The geometry is meshed using 3400 volumetric brick elements with linear shape functions. The neo-Hookean material model is considered as described in section 2.3.1.1 with a discretisation according to section 4.2.1. The parameters for the material model are $\mu = 73\,\text{kPa}$, $\nu = 0.49$ and $\epsilon_r = 4.7$. The corresponding boundary conditions are depicted in Fig. 6.6. On the symmetry plane, the tangential displacements are constrained. Furthermore, the axial displacements on both ends of the simulation domain are constrained to suppress an elongation of the tube.
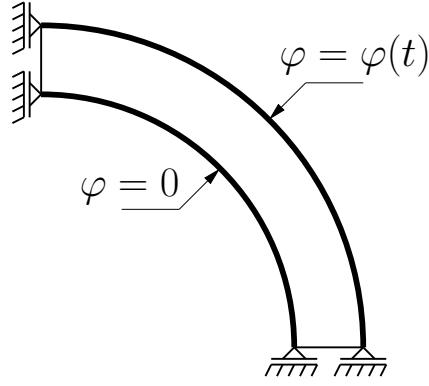
FIGURE 6.6: Electric and displacement boundary conditions of the DE tube.
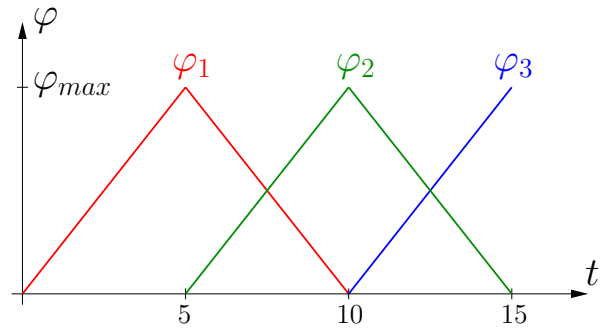
FIGURE 6.7: Time plot of the electric potential applied on the outer electrodes of the DE tube.

The electric loading of the tube is imposed by the application of a potential difference on the electrode pairs. To pump a fluid through the tube, time shifted signals, as depicted in Fig. 6.7, are needed. In this case, a linear increasing and decreasing signal is applied on each electrode pair. The time shift between the electrodes is $5\,\mathrm{s}$. In the numerical simulation, the time is discretized in steps of $0.1\,\mathrm{s}$ which results in 150 time steps for a time range of $15\,\mathrm{s}$. The maximal applied electric potential difference is $\varphi_{max} = 25\,\mathrm{kV}$.

(a) $t = 0$ s

(b) $t = 5$ s

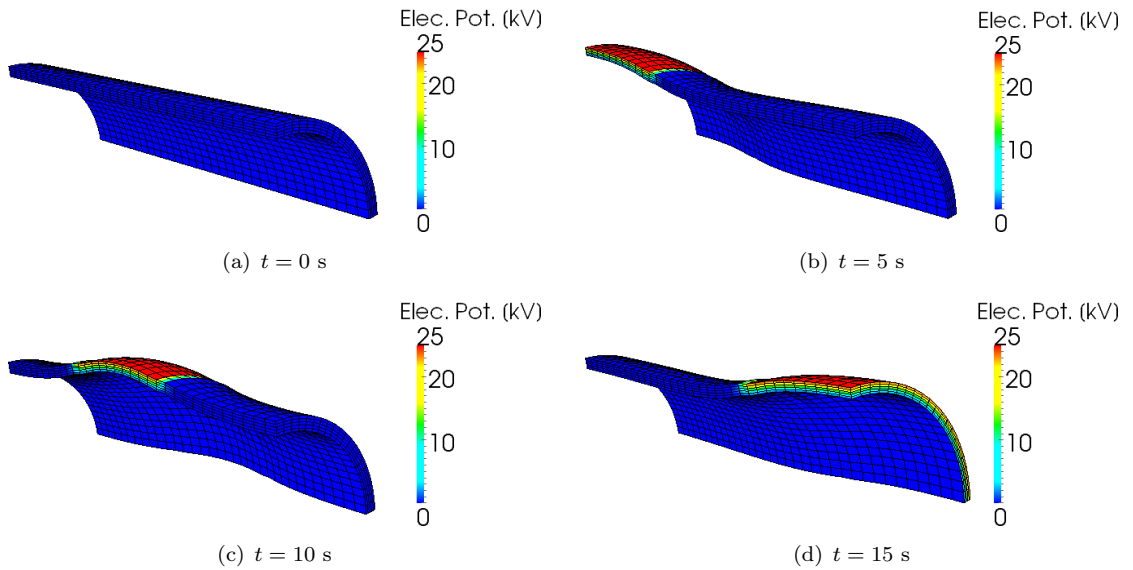(c) $t = 10$ s

(d) $t = 15$ s

FIGURE 6.8: Deformation of the DE tube at different time steps (10x magnification).

The results of the electric potential are given on the deformed geometry as shown in Fig. 6.8. For a proper visualisation, a scaling factor of 10 has been applied to the deformations. The plots show the situations at the initial time step $0\,\mathrm{s}$ (a) and the time steps where each electrode pair reaches $\varphi_{max} = 25\,\mathrm{kV}$ at $5\,\mathrm{s}$ (b), $10\,\mathrm{s}$ (c) and $15\,\mathrm{s}$ (d). Under these circumstances a fluid can be pushed through the DE tube. It should be mentioned, that the given electric signals are just a suggestion to show the working mechanism of

the DE tube pump. Depending on the practical situation, the electric signals would probably be replaced by a sinusoidal activation with time offsets which are optimised for the tube geometry and the medium to be pumped.

6.2 Dynamic Analysis

In this section the numerical implementation is extended by inertia and damping terms according to the description of section 4.3. For the sake of simplicity, a DE hexahedron is considered as a first benchmark which is sufficient to show basic dynamic effects. Two loading cases are considered in this example, namely a constant and a time dependent electric field. The second benchmark consists of the DE tube pump, which was already introduced in 6.1.2. However, a material density is set for the DE which leads to a dynamic reaction of the tube during the simulation.

6.2.1 DE Hexahedron

The benchmarks presented in this section concern the effects of inertia on the DE. For comparison purposes, the examples are based on a 1D analytical analysis presented in [99]. In all subsequent examples, one finite element is considered for the simulations. An electric potential difference is applied on the top and bottom face of the element as shown in Fig. 6.9. The dimensions of the element are set to $a = 10\,\text{mm}$ and $b = 2\,\text{mm}$ which coincide with the dimensions of the work [99]. The constitutive model is the three field formulation from section 2.3.2 with the Q1P0 discretisation offered in section 4.2.3 and the extension by dynamic features shown in section 4.3. To compare the simulation with the 1D analytical analysis, the material parameters are set to $\mu = 67.1\,\text{kPa}$, $\rho = 1200\,\text{kg/m}^3$ and $\kappa_r = 7$. The Poisson's ratio is set to $\nu = 0.4999$ to approximate incompressibility since it is assumed for the analysis in [99].
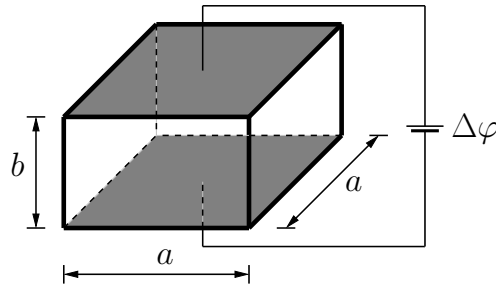

FIGURE 6.9: Geometry of the DE hexahedron. $a = 10\,\text{mm}$, $b = 2\,\text{mm}$.

6.2.1.1   Time Independent Electric Loading

In the first test, a constant electric potential difference $\Delta\varphi$ is applied. In the same manner as a spring-mass system oscillates after the application of a constant force, the DE hexahedron oscillates after the application of a constant $\Delta\varphi$. The potential differences, which are applied on the electrodes, correspond to the nominal electric fields E_0 given in [99]. These are $E_0 = 12, 18$ and $21.27\,\text{kV/mm}$.
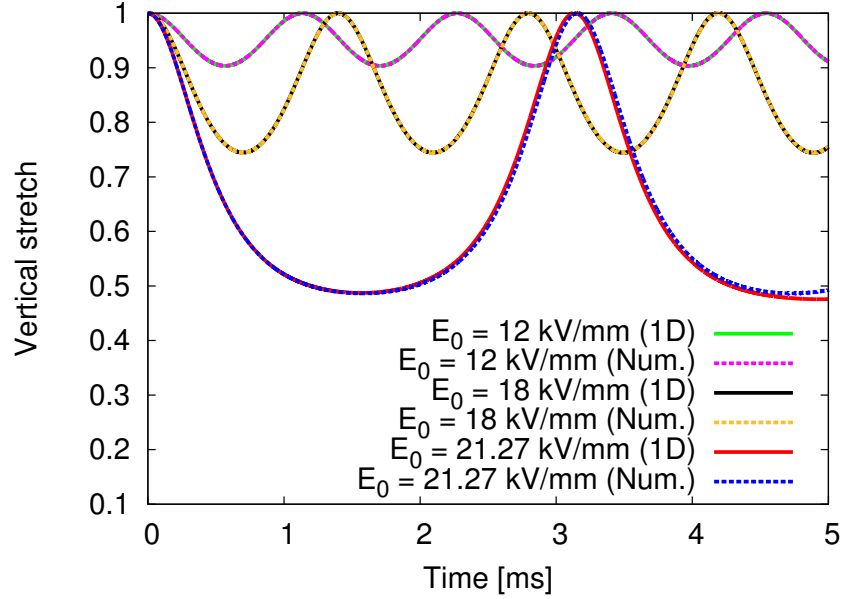

FIGURE 6.10: Vertical stretch of the DE hexahedron activated with a constant electric field.

The vertical stretches of the numerical solutions in comparison to the analytical 1D solutions w.r.t. time are represented in Fig. 6.10. The element oscillates around the equilibrium point of the static case with an amplitude which depends on the applied potential difference (nominal electric field). Also the nonlinearity of DEs becomes visible, since the frequency of the oscillation depends on the applied electric field. For an increasing nominal electric field E_0 the oscillation amplitude increases while the oscillation frequency decreases. A good agreement between the numerical and the analytical 1D solution is observed. However, slight differences are observable for the highest loading case in the second oscillation. A possible explanation for this is that the time integration schemes differ. The numerical solution was obtained with a Newmark time integrator while the 1D solution was computed with a standard time integrator of the software Matlab®. As mentioned previously, the incompressibility is only approximated in the numerical simulation. Obviously this also leads to small differences in the solutions.

6.2.1.2   Time Dependent Electric Loading

In the second example the potential difference is changed from constant to time depen-
dent. This time dependent potential difference $\Delta\varphi$ is applied on the element using a
sinusoidal nominal electric field $E_0 = E_a \sin \omega t$ with a constant amplitude E_a and a
excitation frequency $f = \frac{\omega}{2\pi}$. For comparison, the same amplitude and the same fre-
quencies as in [99] are applied to the finite element. The amplitude of the electric field
is $E_a = 18.5\,\text{kV/mm}$ and the frequencies are $f = 335$ and $410\,\text{Hz}$.

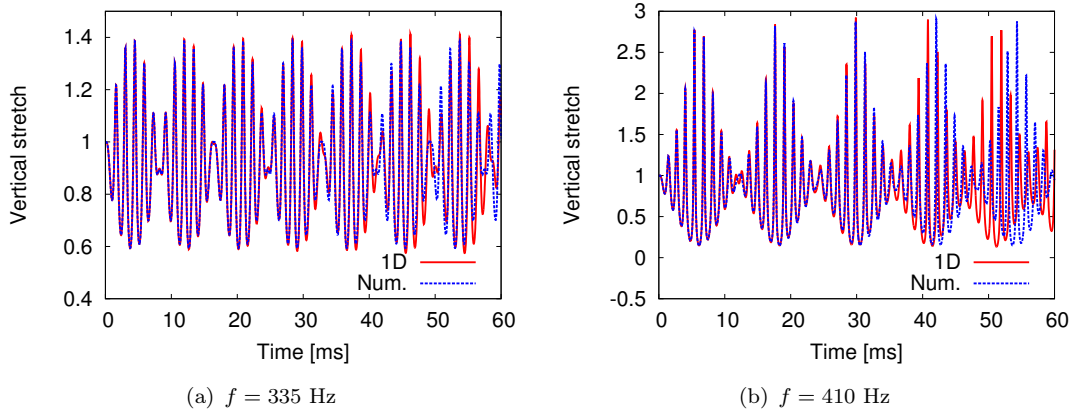(a) $f = 335$ Hz   (b) $f = 410$ Hz

FIGURE 6.11: Vertical stretch of the DE hexahedron activated by a time dependent
electric field. Numerical solution in comparison to 1D solution of [99].

The results of these oscillations for the numerical and the 1D case can be seen in Fig. 6.11.
Again, a good agreement between the different approaches is found, especially at the
beginning. Differences for both frequecies appear with increasing time. The reasons
for these differences are the same as in the previous example. The time integrations
schemes for both solutions are different and perfect incompressibility is compared with
quasi-incompressibility. It should also be noted, that the amplitudes of the oscillations
fluctuate strongly. This is due to the fact, that the selected frequencies are close to the
natural frequency of the structure and will be analysed in the next example.

In the last example, the excitation frequency f is varied. Several time dependent simu-
lations comparable to the previous example are performed covering the frequency range
from 1 to 1000 Hz with 1 Hz increments. Since the so-called dynamic blow-up, see [99],
occurs in this frequency range, the damping parameter has to be set to a non-zero
value. The reason for this is that the oscillation amplitude of the DE hexahedron reaches
high values in the region of the natural frequency which results in an unstable numer-
ical solution. Three different damping parameters are considered, namely $d = 10^5$, 10^6
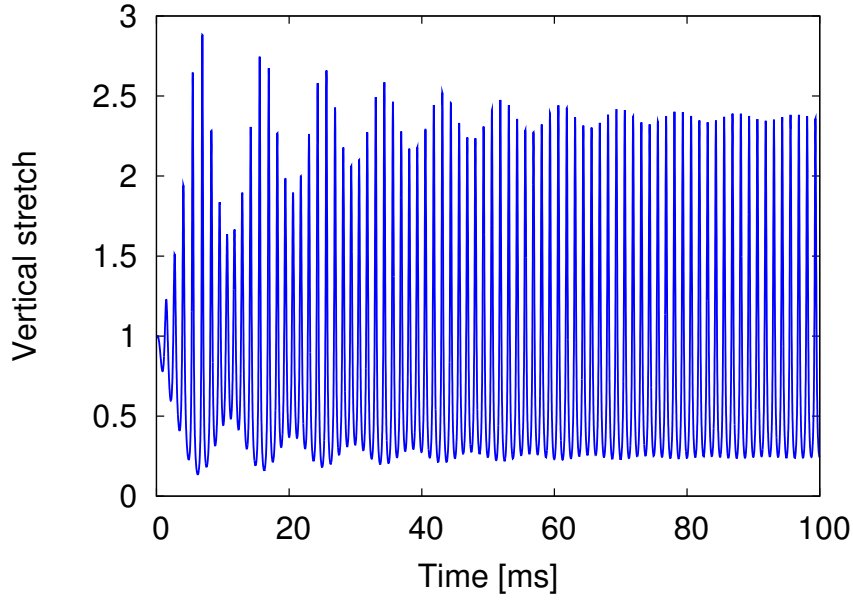and 10^7 kg/sm^3.

FIGURE 6.12: Vertical stretch of the DE hexahedron with damping activated by a time dependent electric field. $f = 400$ Hz, $d = 10^5$.

As it can be seen in Fig. 6.12, the oscillation amplitude of the DE hexahedron with damping is irregular. The hexahedron is excited with a frequency $f = 400$ Hz which is very close to the natural frequency and the damping $d = 10^5$ kg/sm^3 is the lowest one of the studied cases. After a certain amount of time, the amplitude of the oscillations stabilises. The time which is necessary for the amplitude to become steady depends on d and f. In the presented case the amplitude is almost constant after 50 ms. Since this case is an extreme situation, it is assumed for all frequencies and damping parameters that the oscillations are steady after one half of the simulation time at the given time span.

With this methodology, the steady state oscillation amplitude for every frequency and damping case is obtained independently. After the normalisation of the amplitude by relating it to the edge length b of the hexahedron, the frequency response curves are obtained for each damping case. The results of the response are depicted in Fig. 6.13. The response of the DE hexahedron becomes more pronounced with the reduction of d. The frequency with the strongest blow-up effect is ~ 400 Hz. Also at the frequencies of ~ 140, 200, 850 Hz this effect is also observed in a lower intensity. As the parameter d increases, the amplifications at the blow-up frequencies are reduced or even vanish, see the example at 850 Hz with a damping of $d = 10^6$ kg/sm^3.
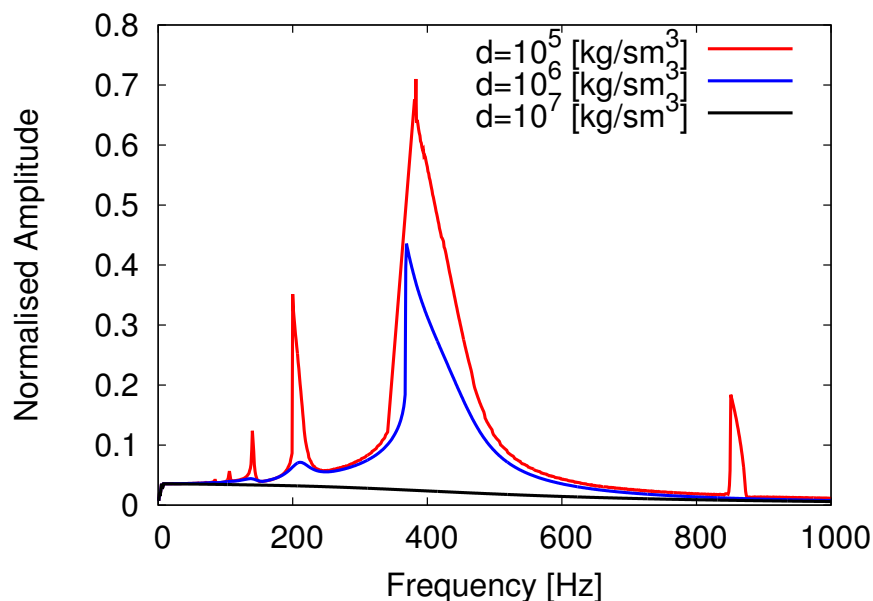
FIGURE 6.13: Frequency dependence of the amplitude of the DE hexahedron for different damping parameters.

6.2.2   Dynamic DE Tube Pump

To consider the dynamic effects in a practical application, the DE tube pump which has been described in 6.1.2 is considered as a benchmark. In contrast to the quasi-static study, only the first electrode on the left side, see Fig. 6.14, is modelled. The idea is to observe the effects of inertia on the DE tube in the sense of a wave propagation which occurs due to a spontaneous contraction of the tube wall at the electrode pair.
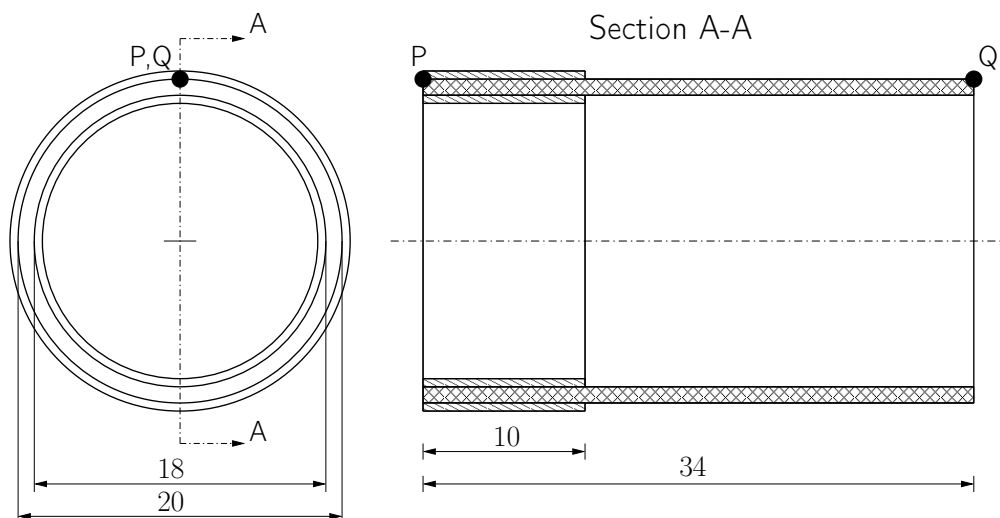

FIGURE 6.14:   Geometry with dimensions in mm of a cylindrical DE tube which is activated by one pair of electrodes.

As in the static benchmark, only a quarter of the tube is modelled with 3400 elements. The element formulation is again the three field formulation. The material parameters, constitutive model and finite element discretisation are the same as in the previous DE tube example, see section 6.1.2. Damping is neglected and the material density is set to $\rho = 1200\,\mathrm{kg/m}^3$. A constant electric potential difference of $\Delta\varphi = 20\,\mathrm{kV}$ is applied on the electrodes resulting in a constant electric field of $20\,\mathrm{kV/mm}$.

Symmetry boundary conditions are applied as shown in Fig. 6.6. The left end of the simulation domain is clamped by constraining the displacements in axial direction. For the right end, two cases are considered, namely the same restriction as at the left side or no restriction at all. Furthermore, the time interval is discretised in steps of $\Delta t = 10^{-5}\,\mathrm{s}$ with a total number of 2000 steps.

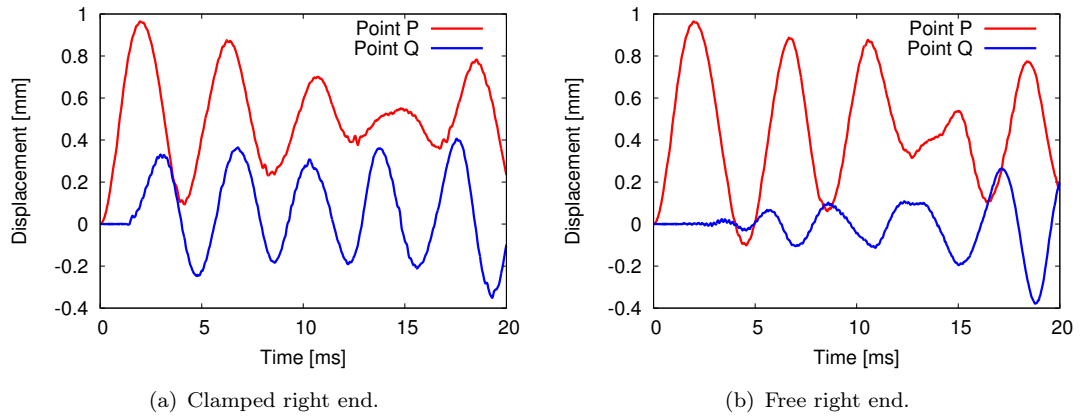(a) Clamped right end. (b) Free right end.

FIGURE 6.15: Radial displacement of the points P and Q of the DE tube activated by a constant electric field.

Under the applied boundary conditions, oscillations and wave propagation are induced in the tube. To evaluate the vibration of the tube, the radial displacements at the points P and Q, see Fig. 6.14, are plotted w.r.t. time in Fig. 6.15 for both boundary condition situations respectively.

In both cases, the time for the propagation of the wave is analysed. The point Q (blue curve) starts to oscillate after a time of $\sim 2\,\mathrm{ms}$. Wave interference is also detected in the plots since the oscillations in the excitation point P are not constant. In both computations, the oscillations at point P are more regular at the beginning of the simulation and more irregular with increasing time. The last observation considers the difference of the plots for the two applied boundary condition situations. In the case of the free right end, see Fig. 6.15.(b), the oscillation amplitude at Point Q increases slower than in the case of the clamped right end, see Fig. 6.15.(a).

To finalise the analysis, the deformed meshes of the DE tube are depicted for the clamped and free right end situation, see Fig. 6.16 and Fig. 6.17. For a better visualisation, a deformation scaling factor of 10 is used.
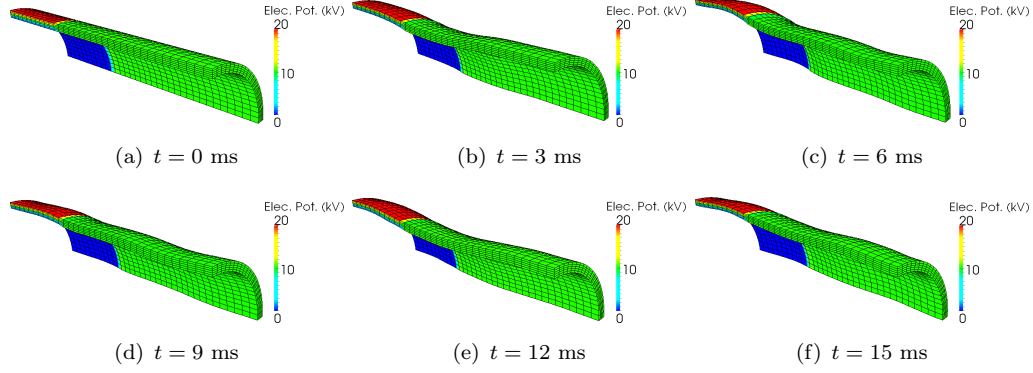

(a) $t = 0$ ms   (b) $t = 3$ ms   (c) $t = 6$ ms

(d) $t = 9$ ms   (e) $t = 12$ ms   (f) $t = 15$ ms

FIGURE 6.16: Deformation of the dynamic DE tube with clamped right end at different time steps (10X magnification).

(a) $t = 0$ ms   (b) $t = 3$ ms   (c) $t = 6$ ms

(d) $t = 9$ ms   (e) $t = 12$ ms   (f) $t = 15$ ms
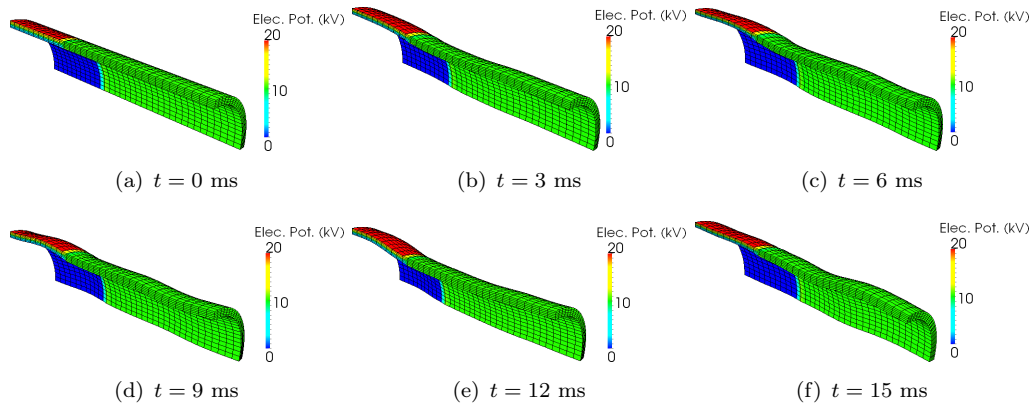
FIGURE 6.17: Deformation of the dynamic DE tube with unconstrained right end at different time steps (10x magnification).

Chapter 7

Microstructural Optimization

As mentioned in chapter 1, one of the technical difficulties of DEs is the extremely high electric field which is necessary to achieve large deformations. The material parameter responsible for this drawback is the relative permittivity ϵ_r which is considerably low in these materials and thus leading to a weak electromechanical coupling. A straight forward solution to this issue would be the consideration of an alternative material with a high value of ϵ_r as e.g. ceramics like barium titanate. However, in ceramics the stiffness is high, so large deformations are not possible. For this reason, the combination of both materials is suggested as a composite microstructure consisting of a DE matrix with ceramic inclusions.

The purpose of the present chapter is to offer a basic numerical analysis in which a representative volume element (RVE) is used as a benchmark. The RVE consists of a DE cube with a spherical inclusion made of ceramic material. The parameters for the material correspond to barium titanate. The chapter is divided into two main sections which treat the quasi-static and the dynamic analysis separately. Additional literature about DE composites can be found in [100–105].

7.1   Quasi-Static Analysis

In this section the numerical analysis is restricted to the quasi-static case. The numerical implementation for the study is performed according to chapter 4. The discretisation with standard displacement elements of the RVE with a constant inclusion radius serves as the starting point for the analysis. Afterwards the element type is modified to the more advanced Q1P0 element and the influence of the diameter of the inclusion is investigated.

7.1.1 RVE with Spherical Inclusion of Constant Radius - Displacement Formulation

In this simulation the effect of a spherical material inclusion in a DE matrix is studied. The inclusion is located in the center of the RVE geometry and the electric boundary condition consists of a potential difference $\Delta\varphi$ applied between the top and bottom surface of the RVE. As in the previous chapter, the simulations are performed in 3D. A scheme of the RVE geometry with the electric boundary conditions can be seen in Fig. 7.1. The diameter of the inclusion is kept constant with $d = 10\,\mu\text{m}$ and the edge length of the RVE is given by $a = 20\,\mu\text{m}$.
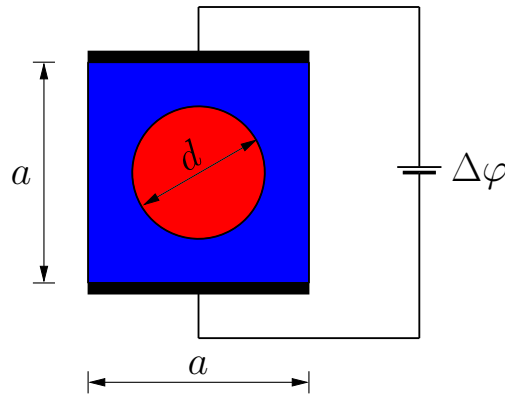

FIGURE 7.1: RVE scheme of the microstructure of a heterogeneous DE consisting of a spherical inclusions (red) in an DE matrix (blue).

Since the solution of the example is symmetric, only a quarter of the geometry is necessary for the finite element meshing, see Fig. 7.2. The mesh is composed of 896 brick elements with 8 nodes per element and linear interpolation. The total number of nodes is 1750 with 4 dof's per node. The element technology is given by the displacement formulation according to section 4.2.1. The constitutive material laws are the neo-Hooke and the Yeoh model which have been introduced in section 2.3.1.1 and 2.3.1.3. The neo-Hooke parameters of the DE are $\mu = 73\,\text{kPa}$, $\nu = 0.49$ and $\epsilon_r = 4.7$. The ceramic inclusion is simulated with the parameters $\mu = 25.7\,\text{MPa}$, $\nu = 0.3$ and $\epsilon_r = 1700$. The parameters for the implementation with the Yeoh model are associated with the neo-Hooke parameters according to the relations,

$$c_1 = \frac{1}{2}\mu, \quad c_2 = -0.1c_1, \quad c_3 = 0.01c_1, \quad K = \frac{2\mu(1+\nu)}{3(1-2\nu)}. \tag{7.1}$$

Thus, the Yeoh parameters are $c_1 = 36.5\,\text{kPa}$, $c_2 = -3.65\,\text{kPa}$, $c_3 = 0.365\,\text{kPa}$ and $K = 3625.67\,\text{kPa}$.
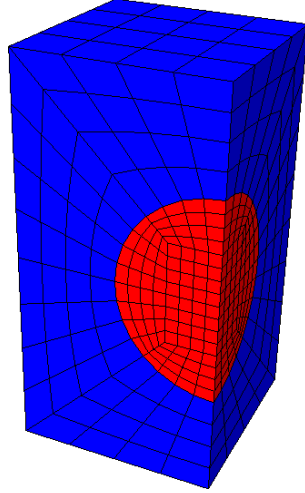
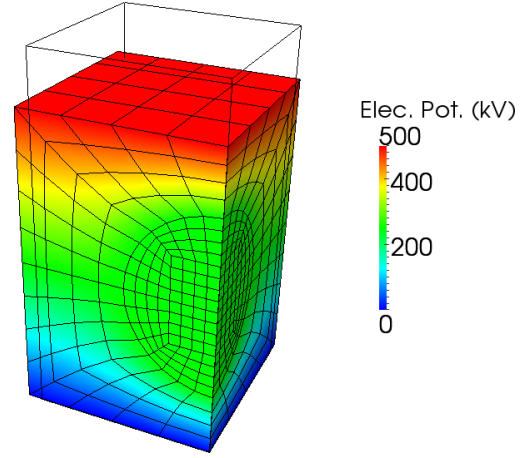FIGURE 7.2: Discretised geometry of the RVE for heterogeneous DE materials.

FIGURE 7.3: Deformation of the RVE activated by an nominal electric field of $E_0 = 25\,\text{kV/mm}$. Neo-Hookean material model.

The normal displacements on the symmetry planes are constrained. On the remaining outer faces of the geometry the normal displacements of the nodes on a face are constrained to be equal. This is performed to be consistent with periodic boundary condition which would be applied on the RVE at the micro-scale level. The boundary condition for the electric loading is applied with a potential difference $\Delta\varphi$ which is incremented linearly in steps of $6\,\text{V}$ as long as the Newton-Raphson iterations converge to the equilibrium solution. With the application of $\Delta\varphi = 500\,\text{V}$ ($E_0 = 25\,\text{kV/mm}$) as the electric loading boundary condition, the RVE is deformed as depicted in Fig. 7.3 for the case of the neo-Hooke model. The outline in Fig. 7.3 represents the undeformed geometry. The contour plot shows the distribution of the electric potential in the structure. One can see, that the spherical inclusion remains nearly undeformed in comparison to the DE matrix. Furthermore, the electric potential φ remains relatively constant with a value of $\sim 250\,\text{V}$ in the inclusion. With this distribution of φ the electric field E is higher in the region between the inclusion and the electrodes in comparison to the homogeneous situation.

The growth of the displacement of the top face of the RVE for an increasing $\Delta\varphi$ is shown in Fig. 7.4. The vertical compression $-u_z/a$ (u_z is the vertical displacement of the top electrode) is plotted as a function of the nominal electric field $\Delta\varphi/a$. For comparison purposes the operational curves of the homogeneous RVE are also given. The curves in Fig. 7.4 predict a stiffer behaviour of the heterogeneous RVE which is opposed to the intention of increasing the compression through a heterogeneous microstructure. The second observation is with regard to the range of the compression and the applied electric field. For the homogeneous case, the ranges are slightly higher than for the heterogeneous ones. The explanation for this is the previously mentioned increase in the electric field in

the region between the inclusion and the electrodes which leads to an instability in these regions. The proposition to handle the undesired stiffening of the heterogeneous RVE consists in the consideration of more advanced element technologies. For this purpose the mixed formulation introduced in section 4.2.3 should be applied and analysed.
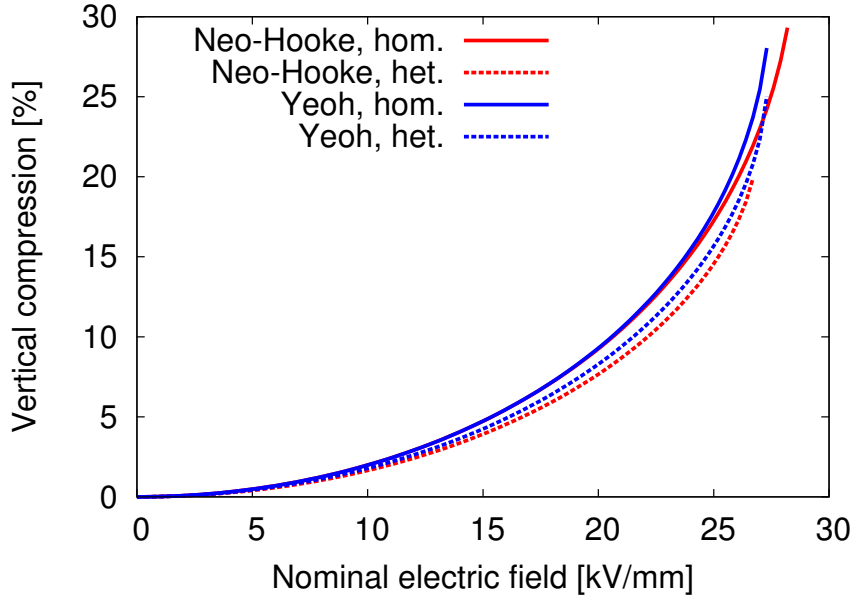

FIGURE 7.4: Compression curves of homogeneous and heterogeneous RVEs. Neo-Hooke and Yeoh material models.

7.1.2 RVE with Spherical Inclusion of Constant Radius - Three Field Formulation

This simulation is a modification of the previous one in which the free energy formulation and the element technology are enhanced. This is performed to handle the volumetric locking which occurs in the numerical analysis of quasi-incompressible materials. In the given example the loading and boundary conditions of the previous benchmark are used. The mesh is depicted in Fig. 7.2. To have comparable free energy formulations a modified neo-Hooke model is considered in the displacement element. The details of the formulation can be found in section 2.3.1.2. The enhanced Q1P0 element is based on the descriptions presented in section 4.2.3 with the free energy model introduced in section 2.3.2.

The discretisation of the geometry with displacement elements is realised by linear and quadratic shape functions. The corresponding number of elements, nodes and number of degrees of freedom are reported in Table 7.1. It should be noted that the internal variables p and θ are taken into account as degrees of freedom in the Q1P0 discretisation. This is why the DOF value of the Q1P0 discretisation is higher than the one of the linear

displacement even tough the number of nodes is equal, see Table 7.1.

Discretisation	Elements	Nodes	DOF
Displacement - Linear	896	1750	7000
Displacement - Quadratic	896	10206	40824
Three field - Q1P0	896	1750	8792

TABLE 7.1: Parameters of RVE discretisation.

The operational curves of the proposed discretisations are shown in Fig. 7.5. Furthermore, the curve for the homogeneous case from the previous section is depicted. The volumetric locking of the heterogeneous RVE becomes obvious. One can see, that an increment of the number of degrees of freedom by discretisation with quadratic elements leads to higher RVE compression (reduction of stiffness). Furthermore, the mesh composed of Q1P0 elements predicts a slightly larger compression. It should be pointed out, that the computational effort of a mesh with Q1P0 elements is considerably lower than the one with quadratic displacement elements, see Table 7.1. With the observation of these results it can be concluded, that special attention has to be given to the volumetric locking when it comes to the microstructural modelling of nearly incompressible DEs. If this issue is neglected, the results predicts a stiffening due to microstructural optimization instead of a softening. A direct but costly approach to overcome this problem is the increase of degrees of freedom either by h or p-refinement. A more elegant and cheaper approach is the use of mixed elements like the Q1P0 element.
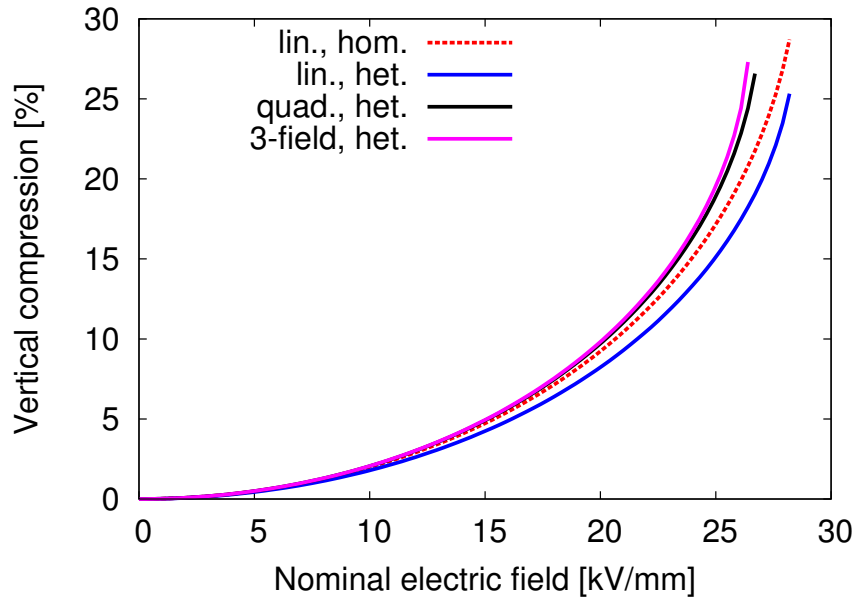

FIGURE 7.5: Influence of the element discretisation on the compression curves of heterogeneous RVEs.

7.1.3   RVE with Spherical Inclusion of Variable Radius

In the previous examples, the radius of the spherical inclusion has been kept constant since the focus of the analysis was to study the influence of the element technology. In a next step in this study, the diameter of the inclusion is varied. For this purpose linear displacement and Q1P0 elements are considered in the discretisation of the RVE. The free energy formulations for the displacement elements are the neo-Hooke and the Yeoh model described in section 2.3.1.1 and 2.3.1.3. The three field energy formulation which is considered for the Q1P0 element is not modified. The material parameters and boundary conditions remain the same as in the two previous examples. The electric loading steps $\Delta\varphi$ also remain unmodified. The diameter of the inclusion is varied from $d = 0$ to $20\,\mu m$ which is the maximum diameter where the inclusion sphere is tangent to the boundary of the RVE.

The results of the analysis are depicted in Fig. 7.6. The horizontal axis corresponds to the diameter of the inclusion with 100 % beeing the maximal diameter. The vertical axis represents the vertical compression of the RVE as the ratio between the displacement of the top electrode and the initial height of the cube. Each curve represents the influence of the inclusion diameter for a given nominal electric field E_0. For a better understanding, only 4 curves are depicted. The curves correspond to fields of 9, 18, 24 and 27 kV/mm.

Figure 7.6.(a) and 7.6.(b) show the results for the neo-Hooke case. According to this analysis and for $\nu = 0.49$, an increase of the inclusion diameter leads initially to a slight decrease of the vertical compression which is followed by an increase. If the Poisson's ratio is increased towards incompressibility ($\nu = 0.4999$) the decrease of the vertical compression is more pronounced.

The Yeoh model which is depicted in Figs. 7.6.(c) and 7.6.(d) shows the same effects concerning the influence of the Poisson's ratio on the vertical compression for an increasing inclusion diameter.

Both material models show the effects of the volumetric locking which is more accentuated as the value of ν approaches 0.5. According to these results, the incorporation of a stiff material with a high relative permittivity ϵ_r cannot be recommended since it leads to a decrease of the the compression for larger inclusion diameters. For a correct analysis of the influence of the inclusion diameter, mixed elements need to be taken into account.

According to the last analysis, in which the RVE geometry is discretised with Q1P0 elements, the prediction is that an inclusion will lead to an increase of the compression of the RVE. The curves are shown in Figs. 7.6.(e) and 7.6.(f).

In all examples it can be observed that the maximal diameter is reduced as the applied electric field increases. This is due to the instability which is taking place in the region between the spherical inclusion and the electrodes on the RVE. The details of this phenomenon, which is rendered in the numerical analysis by the loss of convergence in the Newton iteration, are described in the last paragraph of section 7.1.1.

(a) Neo-Hooke. Linear displacement. $\nu = 0.49$

(b) Neo-Hooke. Linear displacement. $\nu = 0.4999$

(c) Yeoh. Linear displacement. $\nu = 0.49$

(d) Yeoh. Linear displacement. $\nu = 0.4999$

(e) Three field formulation. Q1P0. $\nu = 0.49$

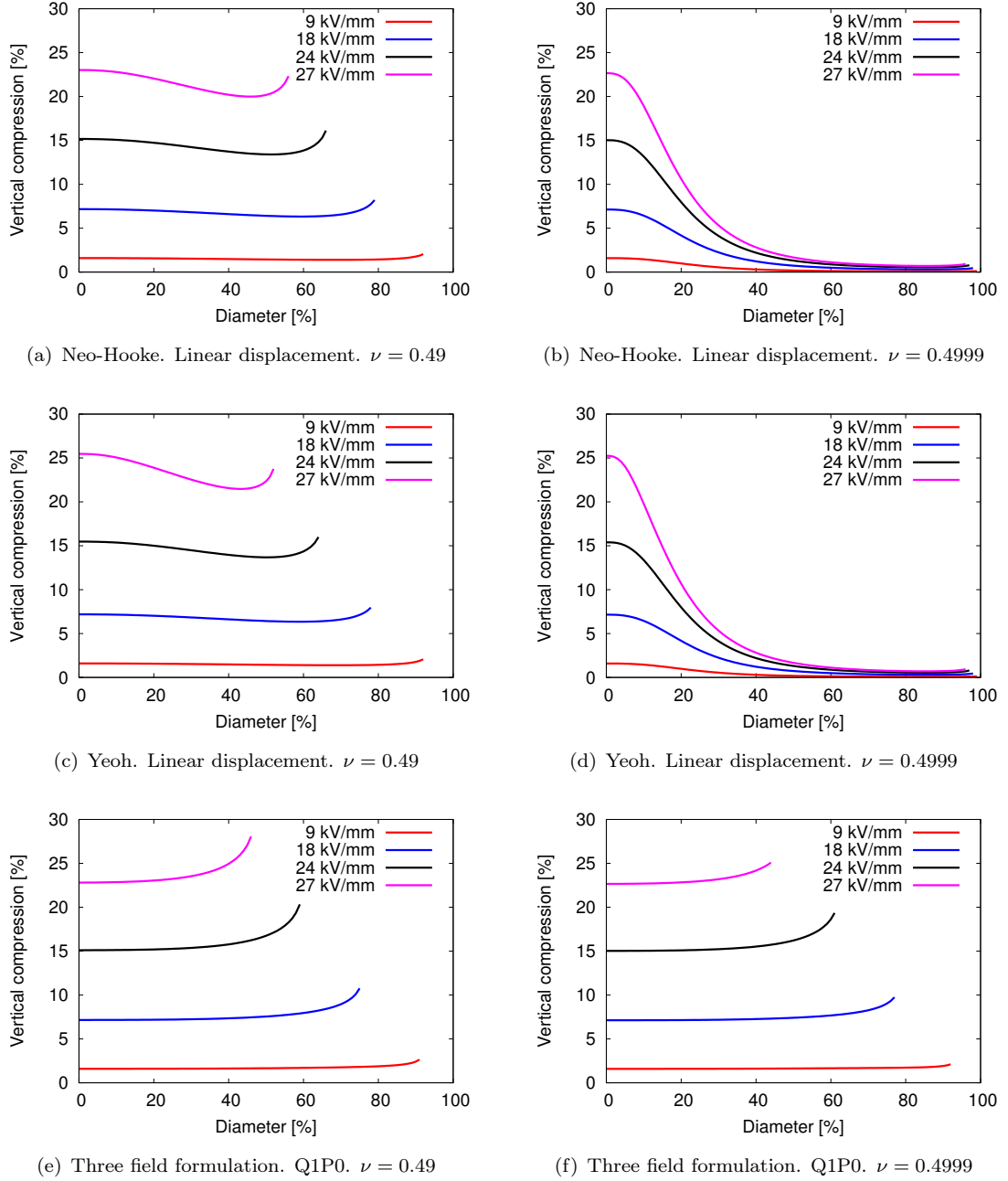(f) Three field formulation. Q1P0. $\nu = 0.4999$

FIGURE 7.6: Influence of inclusion diameter on vertical compression of heterogeneous RVEs for different material models, element discretisations and Poisson's ratios.

7.2   Dynamic Analysis

This section is concerned with the analysis of the RVE under the effects of inertia. Therefore, the numerical implementation used in the quasi-static analysis has been extended by the means of section 4.3. The analysis is performed considering time independent and time dependent electric loadings.

7.2.1   RVE with Spherical Inclusion and Time Independent Electric Loading

In this simulation, the microstructural RVE of the static analysis is considered, see Fig. 7.1. The geometry is discretized in the same manner as before, see Fig. 7.2. The shape of the RVE is a cube with an edge length $a = 20\,\mu m$. For the spherical inclusion, three diameters are considered, namely $d = 5, 10$ and $15\,\mu m$, which correspond to 25, 50 and 75 % of the maximum diameter. The simulations are performed applying the three field formulation. The material parameters are the ones from section 7.1.1 which have been used for the static analysis as well. The densities which are necessary for the dynamic simulation are $\rho = 960\,\mathrm{kg/m^3}$ for the elastomer matrix and $\rho = 6020\,\mathrm{kg/m^3}$ for the spherical inclusion. They correspond to the VHB 4910 tape and barium titanate respectively. The loading of the RVE structure is performed by applying a constant potential difference on the top and bottom faces of the cube thus creating a constant nominal electric field. The considered nominal electric fields are $E_0 = 10, 15, 20$ and $25\,\mathrm{kV/mm}$.

The vertical compression as a function of time is depicted in Fig. 7.7 for constant nominal electric fields. Each curve represents a different inclusion diameter. The homogeneous case is also depicted in each subplot. As in the static case, where the Q1P0 element was studied, the consideration of a material inclusion leads to an increase of compression. In the dynamic case this is observed as the increase of the oscillation amplitudes at larger inclusion diameters. Furthermore, the natural oscillation frequency of the RVE is also increased as the diameter of the inclusion becomes larger. At the higher electric fields the larger diameter values could not be considered, see Figs. 7.7.(c) and 7.7.(d). As in the static analysis, this limitation originates from the stability of the RVE which has been discussed before. In the dynamic simulation the Newton iterations did not converge after a certain amount of time steps.

A second analysis of the dynamic behaviour of the RVE can be performed comparing the dynamic case with the quasi-static simulations. For this purpose, the parameters of the

(a) $E_0 = 10[\text{kV/mm}]$

(b) $E_0 = 15[\text{kV/mm}]$

(c) $E_0 = 20[\text{kV/mm}]$
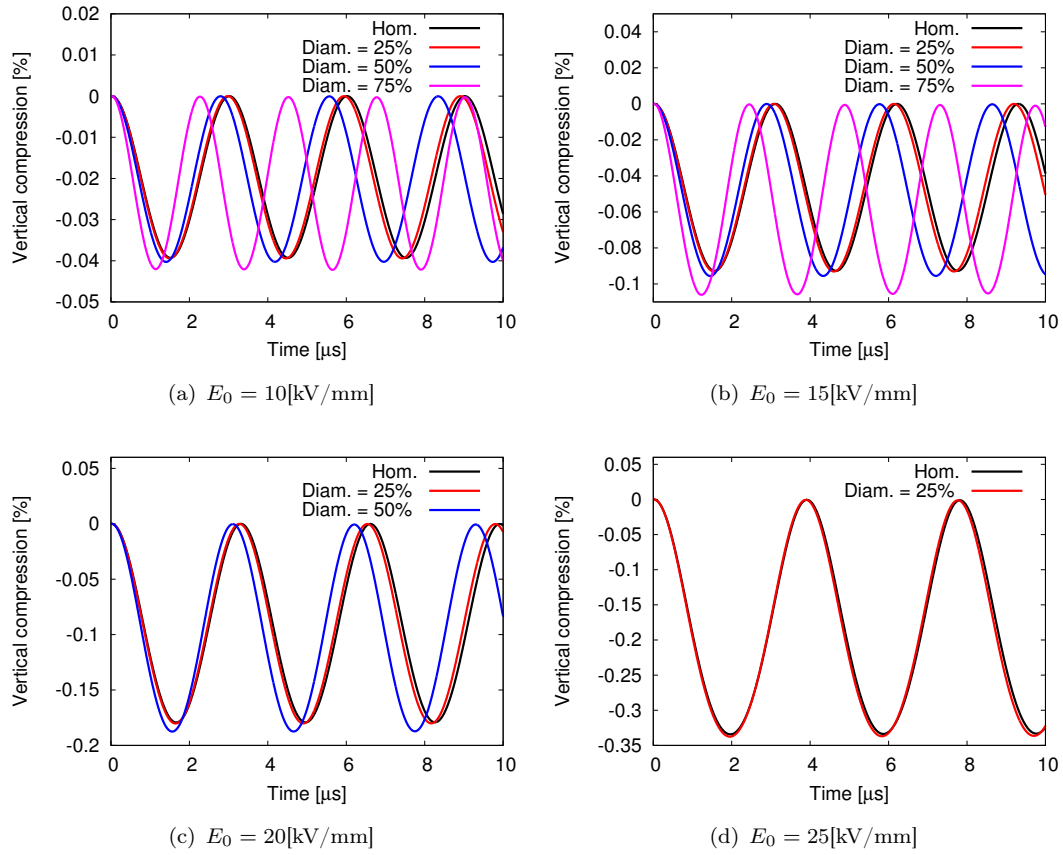
(d) $E_0 = 25[\text{kV/mm}]$

FIGURE 7.7: Influence of the inclusion diameter of the RVE on the oscillation behaviour for different nominal electric fields. Time independent electric loading.

previous analysis are taken into account. The only modification w.r.t. the previous analysis is the number of electric loading cases. For each inclusion diameter the nominal electric field which is applied on the RVE is varied from $E_0 = 0\,\text{kV/mm}$ to $E_0 = 300\,\text{kV/mm}$ in 100 steps. Thus 100 dynamic simulations are performed for each diameter.

In this setting the RVE oscillates with a constant amplitude as observed in Fig. 7.7. The comparison between the amplitude and the compression of the RVE in the quasi-static case is depicted in Fig. 7.8. For all the considered inclusion cases it can be observed, that the compression of the dynamic case is of double the value of the static case. This means that the time dependent compression of an oscillating DEA can be regarded as the superposition of a constant compression corresponding to the static case and an oscillating compression with an amplitude equal to the constant compression. Furthermore, the stretches which are achieved during the oscillations go beyond the critical stretches known from the static stability analysis of chapter 5. In the homogeneous case, shown in Fig. 7.8.(a), the maximum stretch is approximately 0.5 even though the stability analysis predicts a maximum stretch of 0.37. This observation has also been made in [99]. All the plots represented in Fig. 7.8 indicate that the maximum nominal electric field which can

be applied for the dynamic case is limited by the end of the dynamic curves. It is not possible to find a dynamic solution after a further increment of the applied electric field beyond this point. This is rendered by the loss of convergence in the Newton iteration (instability). It should be mentioned, that a dynamic stability analysis could also be performed, but this is beyond the scope of the present work.
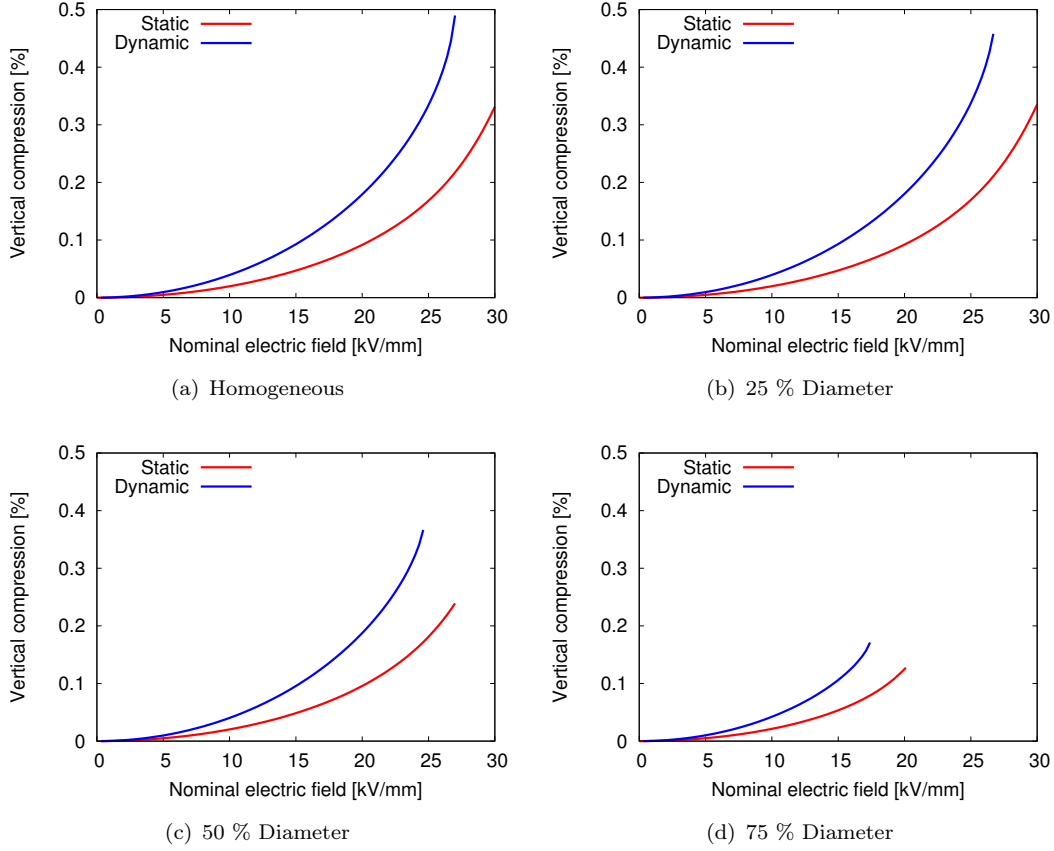

(a) Homogeneous

(b) 25 % Diameter

(c) 50 % Diameter

(d) 75 % Diameter

FIGURE 7.8: Comparison of the compression of the RVE for the static and dynamic case at different inclusion diameters.

7.2.2   RVE with Spherical Inclusion and Time Dependent Electric Loading

To complete the study of the RVE in the same manner as performed with the homogeneous DE, see 6.2.1.2, a time dependent loading is applied as the electric boundary condition on the RVE. The geometry of the RVE and its discretisation remain the same as in the previous benchmarks of this chapter. The material parameters of the DE matrix are $\mu = 20.7\,\text{kPa}$, $\nu = 0.4999$, $\epsilon_r = 4.7$, $\rho = 960$ kg/m^3 and $d = 5 \cdot 10^8$ kg/sm^3. The spherical ceramic inclusion is defined by the parameters $\mu = 25.77\,\text{GPa}$, $\nu = 0.3$, $\epsilon_r = 1700$, $\rho = 6020$ kg/m^3 and $d = 5 \cdot 10^8$ kg/sm^3. Because of the very high oscillation amplitudes which occur at blowup frequency ranges, damping is necessary to obtain

stable numerical solutions. The displacement boundary conditions remain the same as described in 7.1.1. The RVE geometry is fixed at the center of the sphere. The electric potential is set to $\varphi = 0$ at the bottom nodes of the RVE mesh while it is time dependent on the top nodes in a sinusoidal manner. This means that the RVE is subjected to an nominal electric field as in section 6.2.1.2. To observe the influence of different electric fields two loading cases are considered. To this effect, the amplitudes of the electric potential on the top electrode are set to $\varphi_a = 200\,\mathrm{V}$ and $\varphi_a = 235\,\mathrm{V}$. Thus, the amplitudes of the nominal electric fields are $E_a = 10\,\mathrm{kV/mm}$ and $E_a = 11.75\,\mathrm{kV/mm}$. The frequency range is varied from $f = 10$ to $200\,\mathrm{kHz}$ with a resolution of $\Delta f = 1\,\mathrm{kHz}$. The time discretisation is done in steps of $\Delta t = 10^{-8}\,\mathrm{s}$ with a total number of 20000, which is sufficient to obtain a damped solutions.

The response of the RVE for the given excitation frequency range can be seen in Fig. 7.9. The normalised amplitude is defined as the amplitude of the vertical stretch w.r.t. the undeformed height of the RVE. The inclusion diameter is set to values which correspond to 40 % and 50 % of the maximum diameter for comparison. The response curve of a homogeneous RVE is also taken into account for reference. The first observation corresponds to the influence of the inclusion diameter. It is observed, that an increase of the diameter leads to higher deformations or amplitudes. Furthermore, an increase in E_0 produces an increase of the amplitudes which is inferred by comparing Fig. 7.9.(a) to Fig. 7.9.(b). The last observation is with regard to the peak in the frequency sweep. In the range from 80 to 90 kHz the amplitudes reach their highest levels. Depending on the inclusion diameter the peak frequency varies. For larger inclusions, higher peaks are obtained. This originates from the modification of the average value of the material parameters of the RVE. Since the volume ratio of the inclusion changes with different diameters, so do the average material properties as well.

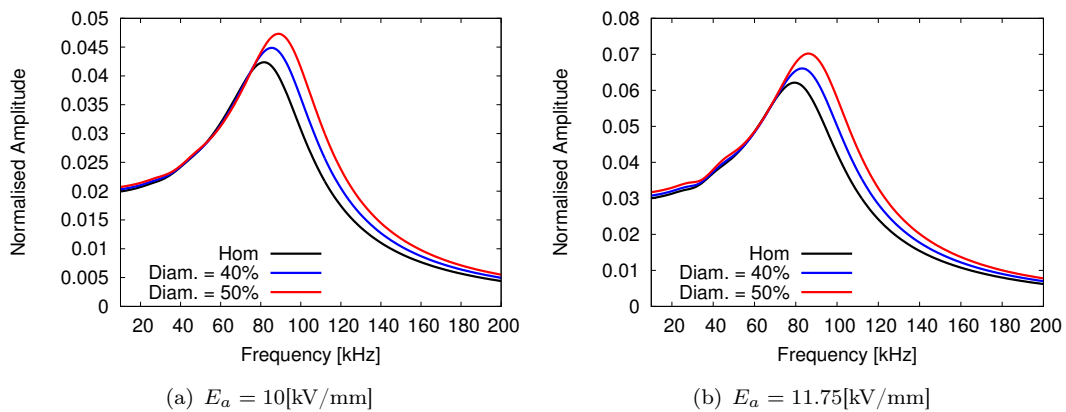(a) $E_a = 10[\mathrm{kV/mm}]$ (b) $E_a = 11.75[\mathrm{kV/mm}]$

FIGURE 7.9: Frequency dependence of the oscillation amplitude of the RVE at different inclusion diameters and nominal electric field amplitudes with damping parameter $d = 5 \cdot 10^8$ [kg/sm^3].

Chapter 8

Conclusion and Outlook

In the work at hand a numerical investigation of DEs has been performed. Because of their large deformation range and quasi-incompressibility, the fundamentals of non-linear mechanics and the three field formulation were introduced in first place. For the comprehension of electric aspects of DEs the theory of electrostatics has been outlined afterwards. Starting from the Coulomb forces of electric fields on electric charges the theory was developed to the electrostatic forces which act on polarisable matter resulting in the electrostatic volume force and the Maxwell stress tensor. In the description of the numerical implementation the electromechanical coupling for compressible DEs has been treated at first. Subsequently the implementation has been modified to treat the quasi-incompressibility of the material and also inertia effects. The electromechanical stability has been outlined as a further aspect. During the incremental compression with an increasing electric field the equilibrium of the actuator can become unstable at a strain which depends on the chosen constitutive material model. This phenomenon was studied in [98] and the numerical results of the implementation in this work were compared with this study. Several benchmarks have been performed to investigate the quasi-incompressibility and the dynamics of DEAs. The volumetric locking effect has been demonstrated and simulation results of DEA dynamics have been compared with analytical studies. Furthermore, a tube pump made of DE material has been simulated for the static and dynamic case. A microstructure consisting of a piezoceramic spherical inclusion in a DE matrix has been proposed and analysed to reduce the magnitude of the electric field which deforms the dielectric. The influence of the inclusion radius and the material incompressibility has been evaluated for the static and dynamic case.

The implementation of the electromechanical coupling has been realised in a monolithic manner with a consistent tangent matrix. This matrix has turned out symmetric even though the derivations for the obtention of the tangent matrix has started from the

mechanical momentum balance and Gauss's law. Thus the electromechanical balance can be derived from a variational principle, see [106]. The incompressibility constraint, the mass inertia and the damping term have been implemented in the pure mechanical parts of the tangent matrix and the internal residual vector. The numerical results of the implementation have been compared to analytical results with good agreement for simulations of static and dynamic case. The stability analysis has agreed with the numerical results by the non convergence of the Newton iterations in the solution process when reaching the unstable equilibrium region. The volumetric locking effect has been observed for the cases of homogeneous and heterogeneous DEAs. In the second case the neglection of the incompressibility predicted a reduction of the compression of the DE for an increasing inclusion diameter. If the incompressibility is considered in the simulation of the microstructure, e.g. a RVE with a spherical inclusion, the prediction is opposed to the previous one, which means that an increasing inclusion diameter leads to a larger compression of the DEA. This indicates the microstructural optimisation of DEs with ceramic materials of high relative permittivity and the consideration of the incompressibility constraint. It should be pointed out that the radius of the inclusion is limited by the electromechanical stability of the elastomer. If the radius is too large, the high electric field in the region between the inclusion and the electrodes will lead to an unstable equilibrium. With regard to the dynamic studies, a blow up effect could be observed in which the oscillation amplitudes become very large at specific excitation frequencies. The effect can be considered as a nonlinear resonance effect.

The study of the DE microstructure in this work has been limited to the variation of the radius of inclusion. Further research could be realised by considering alternative inclusion geometries and orientations. The arrangement of multiple inclusions could also be studied. Also special attention could be given to the interface between the inclusion and the matrix which has been considered as ideal in this work. Since debonding could occur, appropriate interface elements would be necessary to model the phenomenon. As mentioned previously, numerical solutions were not obtained in the unstable compression regions. With a modified solution process, e.g. the arc length method, solutions could be obtained in these regions and the switching between stable regions for material models with more than one stable region could be computed. More investigation could also be realised by simulating different kinds of DEAs to support the development of the actuators. In previous research works like e.g. [36] and [37], the viscosity of the elastomer was included in the modelling. Further phenomenological aspects of elastomers would also be interesting for a better approximation of the numerical simulations to reality. The electrodes of the actuators have been neglected so far and the surrounding space could also be considered, as it was the case in [35].

Appendix A

Derivatives and Symmetry in electromechanical Coupling

This appendix is intended to present the derivatives which are typical in the electrome-chanical coupled field problem. The focus lies on the derivatives of the Maxwell stress tensor and the electric displacement vector which are generally not given in standard literature. Furthermore, the symmetry of the tangent matrix is demonstrated.

The derivations are performed in index notation. In the derivation process the product rule is frequently applied in which the following two derivates are needed:

$$\frac{\partial C_{AB}^{-1}}{\partial C_{CD}} = -\mathbb{I}_{\boldsymbol{C}^{-1}ABCD} = -\frac{1}{2}(C_{AC}^{-1}C_{BD}^{-1} + C_{AD}^{-1}C_{BC}^{-1}), \tag{A.1}$$

$$\frac{\partial J}{\partial C_{AB}} = \frac{1}{2}JC_{AB}^{-1}. \tag{A.2}$$

A.1   Maxwell Stress w.r.t. Right Cauchy-Green Strain

$$\frac{\partial S_{0IJ}^{E}}{\partial C_{PQ}} = \frac{\partial}{\partial C_{PQ}}(C_{IK}^{-1}E_{0K}D_{0J} - \frac{1}{2}\epsilon_0 JE_{0K}C_{KM}^{-1}E_{0M}C_{IJ}^{-1}) \tag{A.3}$$

$$D_{0J} = \epsilon_0(J + \chi)C_{JM}^{-1}E_{0M} \tag{A.4}$$

$$\frac{\partial S_{0IJ}^{E}}{\partial C_{PQ}} = \frac{\partial}{\partial C_{PQ}}(\epsilon_0(J + \chi)C_{IK}^{-1}E_{0K}C_{JM}^{-1}E_{0M} - \frac{1}{2}\epsilon_0 JE_{0K}C_{KM}^{-1}E_{0M}C_{IJ}^{-1}) \tag{A.5}$$

$$\frac{\partial S_{0IJ}^{E}}{\partial C_{PQ}} = \epsilon_0 E_{0K}E_{0M}(\frac{\partial}{\partial C_{PQ}}((J + \chi)C_{IK}^{-1}C_{JM}^{-1}) - \frac{1}{2}\frac{\partial}{\partial C_{PQ}}(JC_{KM}^{-1}C_{IJ}^{-1})) \tag{A.6}$$

$$\frac{\partial S_{0IJ}^E}{\partial C_{PQ}} = \epsilon_0 E_{0K} E_{0M} \left(\frac{\partial (J+\chi)}{\partial C_{PQ}} C_{IK}^{-1} C_{JM}^{-1} + (J+\chi) \frac{\partial C_{IK}^{-1}}{\partial C_{PQ}} C_{JM}^{-1} \right.$$

$$+ (J+\chi) C_{IK}^{-1} \frac{\partial C_{JM}^{-1}}{\partial C_{PQ}} - \frac{1}{2} \left(\frac{\partial J}{\partial C_{PQ}} C_{KM}^{-1} C_{IJ}^{-1} \right.$$

$$\left. \left. + J \frac{\partial C_{KM}^{-1}}{\partial C_{PQ}} C_{IJ}^{-1} + J C_{KM}^{-1} \frac{\partial C_{IJ}^{-1}}{\partial C_{PQ}} \right) \right) \tag{A.7}$$

$$\frac{\partial S_{0IJ}^E}{\partial C_{PQ}} = \epsilon_0 E_{0K} E_{0M} \left(\frac{1}{2} J C_{PQ}^{-1} C_{IK}^{-1} C_{JM}^{-1} \right.$$

$$+ (J+\chi) \left(-\frac{1}{2} (C_{IP}^{-1} C_{KQ}^{-1} + C_{IQ}^{-1} C_{KP}^{-1}) \right) C_{JM}^{-1}$$

$$+ (J+\chi) C_{IK}^{-1} \left(-\frac{1}{2} (C_{JP}^{-1} C_{MQ}^{-1} + C_{JQ}^{-1} C_{MP}^{-1}) \right)$$

$$- \frac{1}{2} \left(\frac{1}{2} J C_{PQ}^{-1} C_{KM}^{-1} C_{IJ}^{-1} \right.$$

$$+ J \left(-\frac{1}{2} (C_{KP}^{-1} C_{MQ}^{-1} + C_{KQ}^{-1} C_{MP}^{-1}) \right) C_{IJ}^{-1}$$

$$\left. \left. + J C_{KM}^{-1} \left(-\frac{1}{2} (C_{IP}^{-1} C_{JQ}^{-1} + C_{IQ}^{-1} C_{JP}^{-1}) \right) \right) \right) \tag{A.8}$$

A.2 Maxwell Stress w.r.t. Electric Field

$$\frac{\partial S_{0IJ}^E}{\partial E_{0P}} = \frac{\partial}{\partial E_{0P}} \left(C_{IK}^{-1} E_{0K} D_{0J} - \frac{1}{2} \epsilon_0 J E_{0K} C_{KM}^{-1} E_{0M} C_{IJ}^{-1} \right) \tag{A.9}$$

$$D_{0J} = \epsilon_0 (J+\chi) C_{JM}^{-1} E_{0M} \tag{A.10}$$

$$\frac{\partial S_{0IJ}^E}{\partial E_{0P}} = \frac{\partial}{\partial E_{0P}} \left(\epsilon_0 (J+\chi) C_{IK}^{-1} E_{0K} C_{JM}^{-1} E_{0M} - \frac{1}{2} \epsilon_0 J E_{0K} C_{KM}^{-1} E_{0M} C_{IJ}^{-1} \right) \tag{A.11}$$

$$\frac{\partial S_{0IJ}^E}{\partial E_{0P}} = \epsilon_0 (J+\chi) C_{IK}^{-1} C_{JM}^{-1} (\delta_{KP} E_{0M} + E_{0K} \delta_{MP})$$

$$- \frac{1}{2} \epsilon_0 J C_{KM}^{-1} C_{IJ}^{-1} (\delta_{KP} E_{0M} + E_{0K} \delta_{MP}) \tag{A.12}$$

$$\frac{\partial S_{0IJ}^E}{\partial E_{0P}} = \epsilon_0 (J+\chi) (C_{IP}^{-1} C_{JM}^{-1} E_{0M} + C_{IK}^{-1} C_{JP}^{-1} E_{0K})$$

$$- \frac{1}{2} \epsilon_0 J C_{IJ}^{-1} (C_{PM}^{-1} E_{0M} + E_{0K} C_{KP}^{-1}) \tag{A.13}$$

$$\frac{\partial S_{0IJ}^E}{\partial E_{0P}} = C_{IP}^{-1} D_{0J} + C_{JP}^{-1} D_{0I} - \frac{J}{J+\chi} C_{IJ}^{-1} D_{0P} \tag{A.14}$$

A.3   Electric Displacement w.r.t. Right Cauchy-Green Strain

$$\frac{\partial D_{0I}}{\partial C_{PQ}} = \frac{\partial}{\partial C_{PQ}}\epsilon_0(J + \chi)C_{IJ}^{-1}E_{0J} \tag{A.15}$$

$$\frac{\partial D_{0I}}{\partial C_{PQ}} = \epsilon_0\frac{\partial(J + \chi)}{\partial C_{PQ}}C_{IJ}^{-1}E_{0J} + \epsilon_0(J + \chi)\frac{\partial C_{IJ}^{-1}}{\partial C_{PQ}}E_{0J} \tag{A.16}$$

$$\frac{\partial D_{0I}}{\partial C_{PQ}} = \frac{1}{2}\epsilon_0 J C_{PQ}^{-1}C_{IJ}^{-1}E_{0J} - \frac{1}{2}\epsilon_0(J + \chi)(C_{IP}^{-1}C_{JQ}^{-1} + C_{IQ}^{-1}C_{JP}^{-1})E_{0J} \tag{A.17}$$

$$\frac{\partial D_{0I}}{\partial C_{PQ}} = \frac{J}{2(J + \chi)}C_{PQ}^{-1}D_{0I} - \frac{1}{2}D_{0Q}C_{IP}^{-1} - \frac{1}{2}D_{0P}C_{IQ}^{-1} \tag{A.18}$$

A.4   Electric Displacement w.r.t. Electric Field

$$\frac{\partial D_{0I}}{\partial E_{0P}} = \frac{\partial}{\partial E_{0P}}(\epsilon_0(J + \chi)C_{IJ}^{-1}E_{0J}) \tag{A.19}$$

$$\frac{\partial D_{0I}}{\partial E_{0P}} = \epsilon_0(J + \chi)C_{IJ}^{-1}\delta_{JP} \tag{A.20}$$

$$\frac{\partial D_{0I}}{\partial E_{0P}} = \epsilon_0(J + \chi)C_{IP}^{-1} \tag{A.21}$$

A.5   Symmetry Condition for the Electromechanical Coupled Tangent Matrix

The symmetry condition given in (4.53) can be written in index notation according to

$$\frac{\partial S_{0IJ}^E}{\partial E_{0P}} = -2\frac{\partial D_{0P}}{\partial C_{IJ}}. \tag{A.22}$$

Special attention has to be given to the fact that tensors of third order are compared which are implemented as matrices by using the Voigt notation. This means that a transposition in the Voigt notation results in an exchange of the indices IJ with P in the index notation. The right hand side of (A.22) can be rewritten by the means of (A.18) with

$$-2\frac{\partial D_{0P}}{\partial C_{IJ}} = D_{0J}C_{IP}^{-1} + D_{0I}C_{JP}^{-1} - \frac{J}{(J + \chi)}C_{IJ}^{-1}D_{0P}. \tag{A.23}$$

The indices of the tensor C_{IJ}^{-1} can be interchanged since it is symmetric. Comparing (A.23) with (A.14) shows that condition (A.22) is true.

Bibliography

[1] S. Shian, R.M. Diebold, and D.R. Clarke. Tunable lenses using transparent dielectric elastomer actuators. *Opt. Express*, 21:8669–8676, 2013.

[2] Y. Bar-Cohen. Electroactive polymers for refreshable braille displays. *SPIE Newsroom*, 2009. doi: 10.1117/2.1200909.1738.

[3] G. Kovacs, P. Lochmatter, and M. Wissler. An arm wrestling robot driven by dielectric elastomer actuators. *Smart Mater. Struct.*, 16:306–317, 2007.

[4] Y. Bar-Cohen. *Electroactive Polymer (EAP) Actuators as Artificial Muscles: Reality, Potential, and Challenges*. Spie Press, Bellingham, 2004.

[5] R.D. Kornbluh, R. Pelrine, H. Prahlad, and R. Heydt. Electroactive polymers: an emerging technology for mems. *Proc. SPIE*, 5344:13–27, 2004.

[6] R.E. Pelrine, R.D. Kornbluh, and J.P. Joseph. Electrostriction of polymer dielectrics with compliant electrodes as a means of actuation. *Sensor Actuat. A-Phys*, 64:77–85, 1998.

[7] Y. Bar-Cohen. Electro-active polymers: current capabilities and challenges. In *EAPAD Conference*, pages 4695–4702.

[8] R. Kornbluh, J. Pelrine, R. Eckerle, and J. Joseph. Electrostrictive polymer artifical muscle actuators. In *Proceedings of 1998 IEEE International Conference on Robotics and Automation*, volume 3, pages 2147–2154, 1998.

[9] Y. Bar-Cohen, S. Sherrit, and S. Lih. Characterization of the electromechanical properties of eap materials. In *Proceedings of EAPAD, SPIEťs 8th Annual International Symposium on Smart Structures and Materials, SPIE*, volume 4329, pages 286–293, 2002.

[10] F. Carpi, D. De Rossi, R. Kornbluh, R. Pelrine, and P. Sommer-Larsen. *Dielectric Elastomers as Electromechanical Transducers*. Elsevier, Amsterdam, 2008.

[11] R. Pelrine, R. Konrbluh, J. Joseph, R. Heydt, Q. Pei, and S. Chiba. High-field deformation of elastometric dielectrics for actuators. *Mater. Sci. Eng. C*, 11:89–100, 2000.

[12] R. Pelrine, R. Konrbluh, Q. Pei, and J. Joseph. High-speed electrically actuated elastomers with strain greater than 100%. *Science*, 287:836–839, 2000.

[13] R. Pelrine, R. Konrbluh, and G. Kofod. High-strain actuator materials based on dielectric elastomers. *Adv. Mater.*, 12:1223–1225, 2000.

[14] R. Samatham, K.J. Kim, D. Dogruer, H.R. Choi, M. Konyo, J.D. Madden, Y. Nakabo, J-D Nam, J. Su, S. Tadokoro, W. Yim, and M. Yamakita. *Active polymers: an overview. In Electroactive Polymers for Robotic applications. Chap. 1.* Springer, London, 2007.

[15] R.A. Toupin. The elastic dielectric. *J. Rational Mech. Anal.*, 5:849–915, 1956.

[16] R.A. Toupin. Elastic materials with couple-stresses. *Arch. Ration. Mech. An.*, 1: 385–414, 1962.

[17] A.C. Eringen. On the foundations of electroelastostatics. *Int. J. Eng. Sci.*, 1: 127–153, 1963.

[18] A.C. Eringen and G.A. Maugin. *Electrodynamics of continua, Foundations and Solid Media, vol. 1.* Springer-Verlag, New York, 1989.

[19] G.A. Maugin. *Continuum Mechanics of Electromagnetic Solids.* North-Holland, Amsterdam, 1988.

[20] Y.H. Pao. Electromagnetic forces in deformable continua. *Mechanics Today*, 4: 209–305, 1978.

[21] M. Dolfin, M. Francaviglia, and L. Restuccia. Thermodynamics of deformable dielectrics with a non-euclidean structure as internal variable. *Technische Mechanik*, 24(2):137–145, 2004.

[22] D.J. Steigmann. On the formulation of balance laws for electromagentic continua. *Math. Mech. Solids*, 14:390–402, 2009.

[23] C. Miehe, D. Rosato, and B. Kiefer. Variational principles in dissipative electro-magneto-mechanics: A framework for the macro-modeling of functional materials. *Int. J. Numer. Meth. Engng.*, 86:1225–1276, 2011.

[24] A. Dorfmann and R.W. Ogden. Magnetoelastic modelling of elastomers. *Eur. J. Mech. A-Solid*, 22:497–507, 2003.

[25] A. Dorfmann and R.W. Ogden. Nonlinear electroelasticity. *Acta Mech.*, 174:167–183, 2005.

[26] A. Dorfmann and R.W. Ogden. Nonlinear electroelastic deformations. *J. Elasticity*, 82:99–127, 2006.

[27] A. Dorfmann and R.W. Ogden. Nonlinear electroelastostatics: Incremental equations and stability. *Int. J. Eng. Sci.*, 48:1–14, 2010.

[28] R.M. McMeeking and C.M. Landis. Electrostatic forces and stored energy for deformable dielectric materials. *J. Appl. Mech.*, 72:581–590, 2005.

[29] R.M. McMeeking, C.M. Landis, and S.M.A. Jimenez. Aprinciple of virtualwork for combined electrostatic and mechanical loading of materials. *Int. J. Nonlin. Mech.*, 42:831–838, 2007.

[30] L.D. Landau and E.M. Lifshitz. *Electrodynamics of Continuous Media*. Pergamon Press Ltd., London, 1960.

[31] Z. Suo, X. Zhao, and W.H. Greene. A nonlinear field theory of deformable dielectrics. *J. Mech. Phys. Solids*, 56:467–486, 2008.

[32] Z. Suo. Theory of dielectric elastomers. *Acta Mech. Solida Sin.*, 23:549–578, 2010.

[33] G. Zhan, A. Tuncer, and Cuiti no A.M. Modeling and simulation of the coupled mechanicalÐelectrical response of soft solids. *Int. J. Plasticity*, 27:1459–1470, 2011.

[34] D.K. Vu, P. Steinmann, and G. Possart. Numerical modelling of non-linear electroelasticity. *Int. J. Numer. Meth. Engng.*, 70:685–704, 2007.

[35] D.K. Vu and P. Steinmann. A 2-d coupled bem-fem simulation of electroelastostatics at large strain. *Comput. Methods Appl. Mech. Engrg.*, 199:1124–1133, 2010.

[36] A. Ask, A. Menzel, and M. Ristinmaa. On the modelling of electro-viscoelastic response of electrostrictive polyurethane elastomers. *IOP Conf. Series: Materials Science and Engineering*, 10:012101, 2010.

[37] A. Ask, A. Menzel, and M. Ristinmaa. Electrostriction in electro-viscoelastic polymers. *Mech. Mater.*, 50:9–21, 2012.

[38] A. Ask, R. Denzer, A. Menzel, and M. Ristinmaa. Inverse-motion-based form finding for quasi-incompressible finite electroelasticity. *Int. J. Numer. Meth. Engng.*, 94:554–572, 2013.

[39] M. Klassen, B.X. Xu, and R. Müller. The influence of incompressibility on the microstructure of dielectric elastomers. *Proc. Appl. Math. Mech.*, 13:221–222, 2013.

[40] S. Klinkel, S. Zwecker, and R. Müller. A solid shell finite element formulation for dielectric elastomers. *J. Appl. Mech.*, 80:021026, 2013.

[41] J. Huang, T. Li, C.C. Foo, J. Zhu, and D.R. Clarke. Giant, voltage-actuated deformation of a dielectric elastomer under dead load. *Appl. Phys. Lett.*, 100: 041911, 2012.

[42] T.Q. Lu and Z.G. Suo. Large conversion of energy in dielectric elastomers by electromechanical phase transition. *Acta Mech. Sinica*, 28:1106–1114, 2012.

[43] G. Kofod and P. Sommer-Larsen. Silicone dielectric elastomer actuators: finite elasticity model of actuation. *Sensor Actuat. A-Phys.*, 122:273–283, 2005.

[44] M. Wissler and E. Mazza. Modeling of a pre-strained circular actuator made of dielectric elastomers. *Sensor Actuat. A-Phys.*, 120:184–192, 2005.

[45] S. Rudykh, K. Bhattacharya, and G. deBotton. Snap-through actuation of thik-wall electroactive balloons. *Int. J. Nonlin. Mech.*, 47:206–209, 2012.

[46] G. Kofod, P. Sommer-Larsen, R. Kornbluh, and R. Pelrine. Actuation response of polyacrylate dielectric elastomers. *J. Intell. Mater. Syst. Struct.*, 14:787–793, 2003.

[47] P. Lochmatter, G. Kovacs, and P. Ermanni. Design and characterization of shell-like actuators based on sof dielectric electroactive polymers. *Smart Mater. Struct.*, 16:1415–1422, 2007.

[48] E.M. Mockensturm and N. Gouldbourne. Dynamic response of dielectric elastomers. *Int. J. Non-Linear Mech.*, 41:388–395, 2006.

[49] W. Kaal and S. Herold. Electroactive polymer actuators in dynamic applications. *IEEE/ASME Trans. Mechatronics*, 16:24–32, 2011.

[50] G. Kofod, W. Wirges, M. Paajanen, and S. Bauer. Energy minimization for self-organized structure formation and actuation. *Appl. Phys. Lett.*, 90:081916, 2007.

[51] M.T. Wissler. *Modeling Dielectric Elastomer Actuators*. PhD thesis, Swiss Federal Institute of Technology in Zurich, 2007.

[52] L. Tian. *Effective Behaviour of Dielectric Elastomer Composites*. PhD thesis, California Institute of Technology, 2007.

[53] Z. Gao. *Modeling and Simulation of the Coupled Mechanical-Electrical Response of Dielectric Elastomers*. PhD thesis, State University of New Jersey, 2007.

[54] N.C.S. Gouldbourne. *Electroelastic Modeling of Dielectric Elastomer Membrane Actuators.* PhD thesis, The Pennsylvania State University, 2005.

[55] G. Kofod. *Dielectric elastomer actuators.* PhD thesis, The Technical University of Denmark, 2001.

[56] J.C. Simo, R.L. Taylo, and K.S. Pister. Variational and projection methods for the volume constraint in finite deformation elasto-plasticity. *Comput. Methods Appl. Mech. Engrg.*, 51:177–208, 1985.

[57] J.C. Simo. On a fully three-dimensional finite-strain viscoelastic damage model: Formulation and computational aspects. *Comput. Methods Appl. Mech. Engrg.*, 60:153–173, 1987.

[58] J.C. Simo and R.L. Taylor. Quasi-incompressible finite elasticity in principal stretches. continuum basis and numerical algorithms. *Comput. Methods Appl. Mech. Engrg.*, 85(3):273–310, 1991.

[59] H.C. Hu. On some variational principles in the theory of elasticity and the theory of plasticity. *Sci. Sinica*, 4:33–54, 1955.

[60] K. Washizu. *On the Variational Principles of Elasticity and Plasticity.* M.I.T. Aeroelastic and Structures Research Laboratory, Cambridge, 1955.

[61] T. Belytschko, W.K. Liu, and B. Moran. *Nonlinear Finite Elements for Continua and Structures.* John Wiley and Sons, Ltd., Chichester, 2000.

[62] G. Holzapfel. *Nonlinear Solid Mechanics.* John Wiley and Sons, Ltd., Chichester, 2000.

[63] P. Wriggers. *Nichtlineare Finite-Element-Methode.* Springer Verlag, Berlin, 2001.

[64] J. Bonet and R.D. Wood. *Nonlinear Continuum Mechanics of Finite Element Analysis.* Cambridge University Press, Cambridge, 2008.

[65] R.W. Ogden. *Nonlinear Elastic Deformations.* Dover, New York, 1997.

[66] K.J. Bathe, E. Ramm, and E.L. Wilson. Finite element formulations for large deformation dynamic analysis. *Int. J. Numer. Meth. Eng.*, 9:353–386, 1975.

[67] A.G. Gent. *Engineering with Rubber.* Hanser Verlag, Munich, 2001.

[68] P.G. Ciarlet. *Mathematical Elasticity I: Three-dimensional elasticity.* Elsevier, 1993.

[69] C. Renaud, J.M. Cros, Z.Q. Feng, and B. Yang. The yeoh model applied to the modeling of large deformation contact/impact problems. *Int. J. Impact Eng.*, 36: 659, 2009.

[70] D.J. Griffiths. *Introduction to Electrodynamics.* Prentice Hall, New Jersey, 1999.

[71] J.D. Jackson. *Classical Electrodynamics.* John Wiley and Sons, Inc., 1999.

[72] E.M. Purcell. *Berkeley Physik Kurs - Band 2: Elektrizität und Magnetismus.* Vieweg, Braunschweig, 1976.

[73] E. Hering, R. Martin, and M. Stohrer. *Physik für Ingenieure.* Springer-Verlag, Berlin, 2007.

[74] A. Kovetz. *Electromagnetic Theory.* Oxford University Press, Oxford, 2000.

[75] J.C. Maxwell. *A Treatise on Electricity and Magnetism. Vols. 1 and 2.* Dover Publications Inc., New York, 1954.

[76] C. Rinaldi and H. Brenner. Body versus surface forces in continuum mechanics: Is the maxwell stress tensor a physically objective cauchy stress? *Phys. Rev. E*, 65: 036615, 2002.

[77] R.A. Anderson. Mechanical stress in a dielectric solid from a uniform electric field. *Phys. Rev. B*, 33:1302–1307, 1986.

[78] J. Melcher. *Continuum Electromechanics.* MIT Press, Cambridge, MA, 1981.

[79] R. Mueller, B.X. Xu, D Gross, M. Lyschik, D. Schrade, and S. Klinkel. Deformable dielectrics - optimization of heterogeneities. *International Journal of Engineering Science*, 48:647–657, 2010.

[80] U. Brink and E. Stein. On some mixed finite element methods for incompressible and nearly incompressible finite elasticity. *Comput. Mech.*, 19:105–119, 1996.

[81] F. Auricchio, L. Beirao da Veiga, C. Lovadina, and A. Reali. A stability study of some mixed finite elements for large deformation elasticity problems. *Comput. Methods Appl. Mech. Engrg.*, 194:1075–1092, 2005.

[82] F. Auricchio, L. Beirao da Veiga, C. Lovadina, and A. Reali. The importance of the exact satisfaction of the incompressibility constraint in nonlinear elasticity: mixed fems versus nurbs-based approximations. *Comput. Methods Appl. Mech. Engrg.*, 199:314–323, 2010.

[83] R.C. Batra. Finite plane strain deformations of rubberlike materials. *Int. J. Numer. Meth. Engng.*, 15:145–160, 1980.

[84] J.M.A. Cesar de Sa and R.M. Natal Jorge. New enhanced strain elements for incompressible problems. *Int. J. Numer. Meth. Engng.*, 44:229–248, 1999.

[85] F. Koschnick. *Geometrische Locking-Effekte bei Finiten Elementen und ein allgemeines Konzept zu ihrer Vermeidung.* PhD thesis, Technische Universität München, 2004.

[86] B.P. Lamichhane. A mixed finite element method for nonlinear and nearly incompressible elasticity based on biorthogonal systems. *Int. J. Numer. Meth. Engng.*, 00:1–6, 2000.

[87] F. Brezzi and M. Fortin. *Mixed and Hybrid Finite Element Methods.* Springer, Berlin, 1991.

[88] P.A.L. van den Bogert, R. de Borst, G.T. Luiten, and J. Zeilmaker. Robust finite elements for 3d-analysis of rubber-like materials. *Engng. Comput.*, 8:3–17, 1991.

[89] D. Chapelle and K.J. Bathe. The inf-sup test. *Comp. Struct.*, 47:537–545, 1993.

[90] F. Diewald. Implementierung eines q2/p1 elementes für eine gemischte 3-feld variationsformulierung. Studienarbeit, Technische Universität Kaiserslautern, 2015.

[91] M. Sabel. Fem-analyse des dynamischen verhaltens von dielektrischen elastomer aktuatoren. Projektarbeit, Technische Universität Kaiserslautern, 2012.

[92] Y. Liu, L. Liu, S. Sun, and J. Leng. Electromechanical stability of a mooney-rivlin-type dielectric elastomer with nonlinear variable permittivity. *Polym. Int.*, 59:371–377, 2010.

[93] A.N. Norris. Comment on method to analyze electromechanical stability of dielectric elastomers. *Appl. Phys. Lett.*, 92:026101, 2008.

[94] X. Zhao and Z. Suo. Method to analyze electromechanical stability of dielectric elastomers. *Appl. Phys. Lett.*, 91:061921, 2007.

[95] J. Zhou, W. Hong, X. Zhao, Z. Zhang, and Z. Suo. Propagation of instability in dielectric elastomers. *Int. J. Solids Struct.*, 45:3739–3750, 2008.

[96] K. Bertoldi and M. Gei. Instability in multilayered soft dielectrics. *J. Mech. Phys. Solids*, 59:18–42, 2011.

[97] J-S Plante and S. Dubowsky. Large-scale failure modes of dielectric elastomer actuators. *Int. J. Solids Struct.*, 43:7727–7751, 2006.

[98] B.X. Xu, R. Müller, M. Klassen, and D. Gross. On electromechanical stability analysis of dielectric elastomer actuators. *Appl. Phys. Lett.*, 97:162908, .

[99] B.X. Xu, R. Müler, A. Theis, M. Klassen, and D. Gross. Dynamic analysis of dielectric elastomer actuators. *Appl. Phys. Lett.*, 100:112903, .

[100] M. Klassen, B.X. Xu, S. Klinkel, and R. Müller. Material modeling and microstructural optimization of dielectric elastomer actuators. *Technische Mechanik*, 32:38–52, 2012.

[101] R. Müller, M. Klassen, and B.X. Xu. Numerical modeling aspects of dielectric elastomer actuators. *Proc. Appl. Math. Mech.*, 12:409–410, 2012.

[102] L. Tian, L. Tevet-Deree, G. deBotton, and K. Bhattacharya. Dielectric elastomer composites. *J. Mech. Phys. Solids*, 60:181–198, 2012.

[103] J. Robertson and D.A. Hall. Nonlinear dielectric properties of particulate barium titanate-polymer composites. *J. Phys. D: Appl. Phys.*, 41:115407, 2008.

[104] G. deBotton, L. Tevet-Deree, and E.A. Socolsky. Electroactive heterogeneous polymers: Analysis and applications to laminated composites. *Mech. Adv. Mater. Struct.*, 14:13–22, 2007.

[105] Q.M. Zhang, H. Li, F. Cheng Z.Y. Poh, M. Xia, H. Xu, and C. Huang. An all-organic composite actuator material with a high dielectric constant. *Nature*, 419: 284–287, 2002.

[106] O.C. Zienkiewicz and R.L. Taylor. *The Finite Element Method - Volume 1.* Butterworth-Heinemann, Oxford, 2000.

Curriculum Vitae

Name: Markus Klassen

Geburtsort: Asunción, Paraguay

10.2002 - 09.2009   Studium des Maschinenbaus mit angewandter Informatik
in der Vertiefungsrichtung Berechnung und Simulation
an der Technischen Universität Kaiserslautern

Diplomarbeit:
Analyse und Anwendung der rationalen B-Spline
Finite Element Methode in 2D

Abschluss: Diplom Ingenieur

10.2009 - 06.2016   Wissenschaftlicher Mitarbeiter
am Lehrstuhl für Technische Mechanik,
Fachbereich Maschinenbau und Verfahrenstechnik
der Technischen Universität Kaiserslautern